

# **Raman Scattering in Carbon Nanotubes**

**Pricciard Roy Shiri**

A dissertation submitted to the Faculty of Science, University of the Witwatersrand, Johannesburg, in fulfilment to the requirements of the degree of Master of Science.

Johannesburg 2007

*Dedicated to my parents Kudakwashe and Beauty Shiri, and my  
siblings Thirling, Prelacy and Thelma for their love, patience,  
emotional and spiritual support. I love you all.*



## DECLARATION

I declare that this dissertation is my own unaided work. It is being submitted for the degree of Master of Science at the University of the Witwatersrand, Johannesburg. It has not been submitted before for any degree or examination in any other University.

Signed

---

Date

---



## ACKNOWLEDGMENTS

My deepest gratitude goes to my supervisor Prof Darrell Comins for his guidance and support and for all the knowledge I have gained from him. Thank you very much. I am also very grateful to my co-supervisor Dr Marjorie Mujaji for her support and caring advice during the course of my studies. I am also deeply grateful to Rudolph Erasmus for teaching me how to use the Raman equipment as well as for insightful discussions on several aspects of my work.

I would like to thank and acknowledge Mr Shane Durbach from the Chemistry department at the University of Johannesburg, Doorfontein Campus for allowing me to use his equipment and teaching me to synthesize carbon nanotubes. Prof Neil Coville from Chemistry department at WITS is also thanked for allowing me to use his laboratory to purify my samples. I am thankful to Prof Mike Witcomb from the WITS electron microscopy unit for assisting with TEM work. I would also like to thank all the staff in the Physics workshop and Glassblowers for helping to make some of the equipment.

I am also deeply grateful to the DST/NRF Centre of Excellence in Strong Materials for the financial support without which my stay at WITS might not have been so smooth. Thank you very much. I would also like to thank my friends and fellow postgraduate students for making my stay at WITS a memorable one.

Last but not least I thank God, who through His Grace and Mercy, makes all things possible.

## ABSTRACT

Analysis of peak shifts of Raman vibrational modes in single-walled carbon nanotubes (SWCNTs) gives important information about the vibrational properties of SWCNTs, which in turn gives a deeper understanding of the physical, electronic and thermal properties of SWCNTs.

In this work, the temperature dependence of the frequencies and linewidths of the vibrational modes of semi-conducting and metallic nanotubes were studied using Raman spectroscopy. The SWCNTs used here were synthesized using the electric-arc discharge method. Two laser lines, the 514.5 nm and 488.0 nm were used to exploit the resonances of the semi-conducting tubes and the 647.1 nm was used to excite metallic SWCNTs.

The radial breathing mode (RBM) peak positions of semi-conducting and metallic tubes were observed to decrease at different rates with increasing temperatures. The line shapes of the RBMs also change significantly with changes in temperatures. The  $G^+$  and  $G^-$  peaks of the tangential modes (G-band) of semi-conducting and metallic nanotubes also decrease at different rates with increasing temperatures. A comparison of the rates of change of mode frequency of the  $G^+$  and  $G^-$  modes in metallic and semi-conducting nanotubes gives more insight into the role played by electron-phonon coupling and plasmon-phonon coupling in each case. It gives a deeper insight into the contentious issue of mode assignment of the  $G^+$  and  $G^-$  modes of metallic SWCNTs.

# Contents

<b>1</b>	<b>Introduction</b>	<b>1</b>
<b>2</b>	<b>Structure and Synthesis of Single Walled Carbon Nanotubes</b>	<b>3</b>
2.1	Introduction . . . . .	3
2.1.1	Chiral Vector . . . . .	3
2.1.2	Chiral Angle, $\theta_c$ . . . . .	5
2.1.3	Translational Vector . . . . .	5
2.2	Electronic Structure of Carbon Nanotubes . . . . .	7
2.2.1	Bonding and Hybridization in Carbon . . . . .	7
2.2.2	Tight Binding Approach in 2D Graphite . . . . .	8
2.2.3	Bonding in Carbon Nanotubes . . . . .	11
2.2.4	Electronic Structure of Carbon Nanotubes . . . . .	12
2.3	Synthesis of Carbon Nanotubes . . . . .	14
2.3.1	Introduction . . . . .	14
2.3.2	Electric Arc Discharge Method . . . . .	15
2.3.3	Laser Ablation Method . . . . .	16
2.3.4	Chemical Vapour Deposition Method . . . . .	18
<b>3</b>	<b>Raman Scattering</b>	<b>20</b>
3.1	Introduction . . . . .	20
3.2	Raman Scattering Process . . . . .	21
3.2.1	Classical Approach . . . . .	21
3.2.2	Quantum Mechanical Approach . . . . .	23



---

3.3	Resonant Raman Scattering . . . . .	25
3.4	Intensity of Raman Scattering . . . . .	25
3.5	Raman Scattering in Carbon Nanotubes . . . . .	26
3.6	Raman Vibrational Modes in SWCNTs . . . . .	27
3.6.1	Radial Breathing Mode (RBM) . . . . .	28
3.6.2	Tangential Mode (G-Band) . . . . .	29
3.6.3	Disorder Induced Mode (D-band) . . . . .	37
<b>4</b>	<b>Raman Experimental Arrangement</b>	<b>39</b>
4.1	Introduction . . . . .	39
4.2	Experimental Apparatus . . . . .	39
4.2.1	The Laser . . . . .	39
4.2.2	The Raman Spectrograph . . . . .	42
4.3	Heating Stage . . . . .	45
4.3.1	High Temperature Experimental Procedure . . . . .	45
4.4	The Cryostat . . . . .	48
<b>5</b>	<b>Electric Arc Discharge Synthesis of SWCNTs</b>	<b>50</b>
5.1	Introduction . . . . .	50
5.2	Experimental Procedures . . . . .	51
5.2.1	The Discharge Chamber . . . . .	51
5.2.2	Synthesis of Carbon Nanotubes . . . . .	52
5.2.3	Transmission Electron Microscopy . . . . .	52
5.2.4	Raman Spectroscopy . . . . .	53
5.3	Purification of SWCNTs . . . . .	58
5.3.1	Purification by Acid Mixture . . . . .	58
5.3.2	Purification of SWCNTs by Heating . . . . .	59
5.4	Discussion . . . . .	60
<b>6</b>	<b>Raman Studies of SWCNTs as a Function of Temperature</b>	<b>61</b>
6.1	Introduction . . . . .	61

---

6.2	Sample Preparation . . . . .	62
6.3	High Temperature Results: G-Bands . . . . .	63
6.3.1	Semi-conducting SWCNTs (514.5 nm) . . . . .	63
6.3.2	Semi-conducting SWCNTs (488.0 nm) . . . . .	66
6.3.3	Metallic SWCNTs (647.1 nm) . . . . .	68
6.3.4	G-Band Linewidth in SWCNTs . . . . .	72
6.4	Radial Breathing Modes . . . . .	78
6.4.1	Calculation of SWCNT Diameters . . . . .	78
6.4.2	514.5 nm Excitation . . . . .	82
6.4.3	488.0 nm Excitation . . . . .	84
6.4.4	647.1 nm Excitation . . . . .	87
6.5	Low Temperature Raman Scattering Studies . . . . .	90
6.5.1	Semi-conducting SWCNTs: 514.5 nm . . . . .	90
6.5.2	Metallic SWCNTs: 647.1 nm . . . . .	93
6.6	G-band Splitting as a Function of Temperature . . . . .	95
6.7	Raman Scattering Measurements as a Function of Laser Power. . . . .	97
6.8	Discussion . . . . .	102
6.8.1	G-band . . . . .	102
6.8.2	Radial Breathing Modes . . . . .	105
<b>7</b>	<b>Conclusions</b>	<b>108</b>

# List of Figures

2.1	Unrolled 2D lattice of a single walled carbon nanotube. A seamless nanotube is constructed if sites O and A, and B and B' are connected. <b>OA</b> is the chiral vector $\mathbf{C}_h$ and <b>OB</b> defines the translational vector <b>T</b> (after Dresselhaus <i>et al.</i> 2005). . . . .	4
2.2	(a) A graphene sheet when a SWCNT is unrolled showing possible ways of rolling the graphene sheet and the chirality of SWCNTs obtained. (b) armchair, (c) zigzag and (d) chiral nanotube (from <a href="http://students.chem.tue.nl">http://students.chem.tue.nl</a> ). . . . .	6
2.3	(a) The unit cell of two dimensional graphite represented by the dotted rhombus and (b) The shaded hexagon shows the Brillouin zone of 2D graphite (after Dresselhaus <i>et al.</i> 2005). . . . .	8
2.4	Energy dispersion relation of 2D graphite throughout the whole Brillouin zone. The insert shows the energy dispersion along the high symmetry points $\Gamma$ , M and K ( after Saito <i>et al.</i> 1998). . . . .	12
2.5	(a) The Brillouin zone of a carbon nanotube represented by the line segment WW'.(b) An expanded view of the graphite 2D Brillouin zone showing the allowed $\mathbf{k}$ vectors for one dimensional nanotubes. One of the lines intersects a K point making the tube metallic ((a) after Saito <i>et al.</i> 1998 and (b) after Saito and Kataura 2001). . . . .	13

2.6	Calculated electronic band structure of nanotubes (5,0), (3,3), and (4,2) in the energy range between -4 and 4 eV with respect to the Fermi energy within the orthogonal-tight binding model (full lines) and the $\pi$ -band tight binding model (dotted lines)(after Popov and Henrard 2004). . . . .	15
2.7	Schematic diagram of the laser ablation arrangement for carbon nanotube synthesis (after Dai 2001). . . . .	17
2.8	Growth mechanisms for SWCNTs proposed by Kataura et al. 2000. .	17
2.9	Two general growth modes of nanotubes in CVD. <i>Left</i> : base growth mode. <i>Right</i> : tip growth mode ( <i>after Dai 2001</i> ). . . . .	18
3.1	A typical Raman spectrum of a polycrystalline material (coumarin) showing the Rayleigh line, and both the Stokes and anti-Stokes sides of the Raman spectrum (from Keresztury, 2002). . . . .	21
3.2	Energy level diagrams showing (a) Rayleigh scattering, (b) Stokes Raman scattering, and (c) anti-Stokes Raman scattering. . . . .	24
3.3	DOS for three different carbon nanotubes, (a) metallic nanotube, (b) and (c), semi-conducting tubes of different chiralty. The DOS near the Fermi level has a non-zero value for metallic tubes and a zero value for semi-conducting tubes. (d) shows the electronic transition energies $E_{ii}$ for all $(n, m)$ SWCNTs in the diameter range 0.4-3.0 nm (after Jorio <i>et al.</i> 2003). . . . .	26
3.4	Raman vibrational modes in semi-conducting SWCNTs showing the radial vibrations of C-atoms giving rise to the radial breathing mode (RBM), the G band, with C-atom vibrations along nanotube axis (LO mode) and tangential to the circumference of the nanotube (TO mode) and the disorder induced D-band. . . . .	28
3.5a	The G-band of semi-conducting SWCNTs. Both the $G^-$ and $G^+$ have Lorentzian lineshapes. . . . .	34

---

3.5b	The G-band of metallic SWCNTs. The $G^+$ band has a Lorentzian lineshape, while the $G^-$ band is much broader and can be fitted with a BWF lineshape. . . . .	34
3.6	Variation of the G-band Stokes and anti-Stokes intensities as a function of the incident photon flux. (After Teredesai <i>et al.</i> 2001) . . . . .	37
4.1	A transition scheme for an $Ar^+$ laser. The first collision ionises the neutral argon and the next pumps it to an excited state (from the Operational Manual for the Spectra Physics 2020/2025 Ion Laser.) . . . . .	41
4.2	Schematic diagram of a gas laser (after Beesley (1976)) . . . . .	42
4.3	Schematic diagram of the Raman Spectrograph showing the beam path (from the Instruction Manual for the Jobin-Yvon T64000 Raman spectrograph). . . . .	44
4.4	Schematic diagram of the Linkam heating stage (after Hayes 2002). . . . .	46
4.5	Schematic diagram of the cryostat system (after Hayes, 2002). . . . .	49
5.1	Schematic diagram of the electric arc discharge apparatus. . . . .	51
5.2	Transmission electron microscopy images of the as-produced soot using a 26 at.% $LaNi_5$ catalyst at a helium pressure of 60 kPa clearly showing bundles of SWCNTs. . . . .	53
5.3	Raman spectra showing the RBM, the D-band and the G-band of the as-produced soot containing SWCNTs produced with catalyst A consisting of 25 at.% $LaNi_5$ at helium pressures of 30kPa (top) and 60kPa (bottom). . . . .	54
5.4	Raman spectra showing the RBM, the D-band and the G-band of the as-produced soot containing SWCNTs produced with catalyst B consisting of 26 at.% $LaNi_5$ at helium pressures of 30kPa (top) and 60kPa (bottom). . . . .	55

---

5.5	Raman spectra showing the RBM, the D-band and the G-band of the as-produced soot containing SWCNTs produced with catalyst C consisting of 2.7 at.% Fe, 2.9 at.% Co, 4 at.% FeS and 2.6 at.% Ni at a helium pressures of 30kPa (top) and catalyst D consisting of 5 at.% YNi at a helium pressure of 60kPa (bottom). . . . .	56
5.6	Room temperature Raman spectra taken on the same spot of a sample of SWCNTs using the 514.5 nm laser excitation before and after heating.	60
6.1	G bands for semi-conducting SWCNTs excited with the 514.5 nm laser line with decreasing temperatures for the second cooling cycle.	63
6.2a	Temperature dependence of the $G^+$ mode frequency in SWCNTs during two heating and cooling runs using the 514.5 nm laser line. . . . .	64
6.2b	Temperature dependence of the $G^-$ mode frequency in SWCNTs during two heating and cooling runs using the 514.5 nm laser line. . . . .	64
6.3	Temperature dependence of the $G^+$ and $G^-$ mode frequencies of SWCNTs excited by the 514.5 nm laser line corresponding to the second cooling run. The $G^-$ band has a slope of $-2.94 \text{ cm}^{-1}/100\text{K}$ and the $G^+$ band has a slope of $-2.75 \text{ cm}^{-1}/100\text{K}$ . . . . .	65
6.4	G bands for semi-conducting SWCNTs measured with decreasing temperatures during the second cooling run, using the 488 nm excitation line. The curves have been displaced for the purposes of clarity. . . . .	66
6.5a	Temperature dependence of the $G^+$ mode frequencies in SWCNTs during two heating and cooling runs using the 488.0 nm excitation line.	67
6.5b	Temperature dependence of the $G^-$ mode frequencies in SWCNTs during two heating and cooling cycles using the 488.0 nm excitation. . . . .	67
6.6	Temperature dependence of the $G^+$ and $G^-$ mode frequencies of SWCNTs excited by the 488.0 nm laser line corresponding to the second cooling run, with the slopes being $-2.45 \text{ cm}^{-1}/100\text{K}$ for the $G^-$ band and $-1.99 \text{ cm}^{-1}/100\text{K}$ for the $G^+$ band. . . . .	68

---

6.7	G bands for metallic SWCNTs measured with decreasing temperatures during the first cooling run using 647.1 nm excitation. The curves have been displaced for the purposes of clarity. . . . .	69
6.8a	Temperature dependence of the $G^+$ mode frequencies in SWCNTs during heating and cooling runs using the 647.1 nm laser line. . . . .	70
6.8b	Temperature dependence of the $G^-$ mode frequencies in SWCNTs during heating and cooling runs using the 647.1 nm laser line. . . . .	70
6.9	Temperature dependence of the $G^+$ and $G^-$ mode frequencies of SWCNTs excited by the 647.1 nm laser line corresponding to the first cooling run, with the slopes being $-1.67 \text{ cm}^{-1}/100\text{K}$ for the $G^-$ band and $-2.68 \text{ cm}^{-1}/100\text{K}$ for the $G^+$ band. . . . .	71
6.10a	Temperature dependence of the line width of the $G^-$ band for SWCNTs excited with the 488.0 nm laser line using a laser power density of $44 \text{ W}/\text{cm}^2$ on the sample. The slope of the graph is $0.76 \text{ cm}^{-1}/100\text{K}$ . . . . .	73
6.10b	Temperature dependence of the line width of the $G^+$ band for SWCNTs excited with the 488.0 nm laser line using a laser power density of $44 \text{ W}/\text{cm}^2$ on the sample. The slope of the graph is $1.66 \text{ cm}^{-1}/100\text{K}$ . . . . .	74
6.11a	Temperature dependence of the line width of the $G^-$ band for SWCNTs excited with the 514.5 nm laser line using a laser power density of $60 \text{ W}/\text{cm}^2$ on the sample. The slope of the graph is $0.88 \text{ cm}^{-1}/100\text{K}$ . . . . .	74
6.11b	Temperature dependence of the line width of the $G^+$ band for SWCNTs excited with the 514.5 nm laser line using a laser power density of $60 \text{ W}/\text{cm}^2$ on the sample. The slope of the graph is $1.51 \text{ cm}^{-1}/100\text{K}$ . . . . .	75
6.12a	Temperature dependence of the line width of the $G^-$ band (BWF line) for SWCNTs excited by the 647.1 nm laser line using a laser power density of $20 \text{ W}/\text{cm}^2$ on the sample. The slope of the graph is $-5.33 \text{ cm}^{-1}/100\text{K}$ . . . . .	75
6.12b	Temperature dependence of the line width of the $G^+$ band for SWCNTs excited with the 647.1 nm laser line using a laser power density of $20 \text{ W}/\text{cm}^2$ on the sample. The slope of the graph is $3.63 \text{ cm}^{-1}/100\text{K}$ . . . . .	76

---

6.13	Deconvoluted radial breathing mode for semi-conducting tubes excited with the 514.5 nm laser line. . . . .	79
6.14	Deconvoluted radial breathing mode for semi-conducting tubes excited with the 488.0 nm laser line. . . . .	80
6.15	Deconvoluted radial breathing mode for metallic nanotubes excited using the 647.1 nm laser line. . . . .	81
6.16	Deconvoluted RBM spectra of SWCNTs at different temperatures for the 514.5 nm excitation line, showing the change in line shape of the RBM with increasing temperatures. . . . .	83
6.17	Temperature dependence of the radial breathing mode for the $\omega_{181}$ peak obtained using the 514.5 nm laser line, with slope being $-1.95 \text{ cm}^{-1}/100\text{K}$ . . . . .	84
6.18	Deconvoluted radial breathing mode spectra for SWCNTs at different temperatures excited using the 488.0 nm excitation line. . . . .	86
6.19	Temperature dependence of the radial breathing mode for the $\omega_{179}$ and $\omega_{158}$ peaks for semi-conducting SWCNTs excited by the 488.0 nm laser line. . . . .	86
6.20	Deconvoluted radial breathing mode spectra of SWCNTs at different temperatures excited using the 647.1 nm excitation line. . . . .	88
6.21	Temperature dependence of the radial breathing mode for the $\omega_{190}$ peak for metallic SWCNTs excited by the 647.1 nm laser line . . . . .	89
6.22a	Temperature dependence of the G band for the low temperature region for semi-conducting SWCNTs excited using the 514.5 nm excitation. The curves have been displaced for the purposes of clarity. . . . .	90
6.22b	Temperature dependence of the $G^+$ and $G^-$ band frequencies for SWCNTs excited with the 514.5 nm laser line for the low temperature region, with slopes being $-2.11 \text{ cm}^{-1}/100\text{K}$ for the $G^-$ band and $-2.44 \text{ cm}^{-1}/100\text{K}$ for the $G^+$ band. . . . .	91



---

6.23	Temperature dependence of the RBM for the low temperature region for SWCNTs excited using the 514.5 nm excitation. The curves have been displaced for reasons of clarity. . . . .	92
6.24	Temperature dependence of the $G^+$ and $G^-$ band frequencies for the low temperature and high temperature regions for SWCNTs excited with the 514.5 nm laser line. . . . .	92
6.25a	Temperature dependence of the G band for the low temperature region for metallic SWCNTs excited using the 647.1 nm excitation. The curves have been displaced for the purposes of clarity. . . . .	93
6.25b	Temperature dependence of the $G^+$ and $G^-$ band frequencies for metallic SWCNTs excited with the 647.1 nm laser line for the low temperature region, with slopes being $-1.98 \text{ cm}^{-1}/100\text{K}$ for the $G^-$ band and $-2.18 \text{ cm}^{-1}/100\text{K}$ for the $G^+$ band. . . . .	94
6.26	Temperature dependence of the $G^+$ and $G^-$ band frequencies for the low temperature and high temperature regions for metallic SWCNTs excited with the 647.1 nm laser line. . . . .	94
6.27	Temperature dependence of the $G^+-G^-$ splitting for metallic and semi-conducting SWCNTs. (Colour line) Circles: Metallic SWCNTs excited at 647.1 nm. Squares: Semi-conducting SWCNTs excited at 514.5 nm. Inverted triangles: Semi-conducting SWCNTs excited at 488.0 nm. . . . .	96
6.28a	Laser power density dependence of the Stokes $G^-$ and $G^+$ modes for semi-conducting SWCNTs excited with the 514.5 nm line of the $\text{Ar}^+$ laser. . . . .	98
6.28b	Laser power density dependence of the anti-Stokes $G^-$ and $G^+$ modes for SWCNTs excited with the 514.5 nm excitation line of the $\text{Ar}^+$ laser. . . . .	98
6.29	Laser power density dependence of the intensity of the Stokes and anti-Stokes $G^+$ modes for SWCNTs excited with the 514.5 nm excitation line of the $\text{Ar}^+$ laser. . . . .	99

- 6.30 Radial breathing modes at 373K and at 773K showing the different lineshapes at different temperatures for the 514.5 nm excitation. . . . 107

# List of Tables

5.1	Determination of SWCNT's purity using intensity ratios. . . . .	57
6.1	Slopes of the graphs of frequency versus temperature for the $G^+$ and $G^-$ bands of metallic and semi-conducting SWCNTs. . . . .	72
6.2	Calculated diameters and corresponding chiralities for semi-conducting tubes excited by the 514.5 nm laser line. . . . .	79
6.3	Calculated diameters and corresponding chiralities for semi-conducting tubes excited by the 488.0 nm laser line. . . . .	80
6.4	Calculated diameters and corresponding chiralities for metallic tubes excited by the 647.1 nm laser line. . . . .	81
6.5	Slopes of the graphs of frequency versus temperature for the RBM modes excited with various laser wavelengths. . . . .	89
6.6	Slopes of the graphs of frequency versus temperature for the $G^+$ and $G^-$ bands of metallic and semi-conducting SWCNTs. . . . .	95
6.7	Calculated sample temperatures using the AS/S intensity ratio method and the peak frequency shift method. . . . .	101

# Chapter 1

## Introduction

Carbon nanotubes are an allotrope of carbon. Since they were first reported by Iijima (1991), there has been much research into these materials because of their novel properties which make them potentially useful in applications such as electronics, nanotechnology, optics and in material science.

Carbon nanotubes have a Young's modulus that is greater than that of diamond, they are very good thermal conductors, they are good superconductors at temperatures below 0.55K and depending on their chirality, they can have a conductivity that is comparable to that of copper (Kempa 2002).

Single-walled carbon nanotubes (SWCNTs) can be imagined to be the tubes that are formed when a graphene layer is rolled up in different ways. There are a number of methods available for synthesis of carbon nanotubes. These include the electric arc discharge method, laser ablation and chemical vapor deposition. In this project the arc discharge method was used to synthesize SWCNTs of high purity and with a narrow diameter dispersion.

There are a number of methods available for studying and characterizing SWCNTs. These include Transmission Electron Microscopy (TEM), Atomic Force Microscopy (AFM) and Raman Spectroscopy. The latter has been a widely used technique for studying and characterizing SWCNTs, being a non-destructive technique that can be used directly from the production stage. The Raman spectra of carbon

---

nanotubes have features that give information about the vibrational, structural and electronic properties of carbon nanotubes (Souza Filho *et al.* 2003). An understanding of the behaviour of these Raman active features under different conditions is important for a deeper understanding of the physics of SWCNTs.

In the present work the temperature dependence of Raman vibrational modes was studied. Previous work of this kind includes that of Huong *et al.* (1995) and Li *et al.* (2000) who studied the behaviour of Raman modes of SWCNTs due to laser induced temperature effects in the range 300K-700K. Laser power densities on the samples for this temperature range varied from  $10^2$ - $10^4$  W/cm<sup>2</sup>. They calculated sample temperature using the ratio of the Stokes to anti-Stokes intensities of the Raman peaks.

Raravikar *et al.* (2002) studied the temperature dependence of the radial breathing mode in SWCNTs in the temperature range 299- 773K using a Linkam cell. They used a power density of  $3 \times 10^5$  W/cm<sup>2</sup>.

In the present work the radial breathing mode and the tangential modes in SWCNTs were studied as a function of temperature in the range 77K-1073K in order to provide further information on their temperature dependence over a wider temperature range. A Linkam hot stage was used for high temperature Raman measurements and an Oxford Instruments micro-cryostat system was used for low temperature studies. Laser power densities were kept as low as possible to minimize any laser heating effects. In the present work it is shown that taking the sample through one or more annealing cycles under argon gas stabilizes the sample, giving an improvement in the nature of results.

The results are shown to provide information relevant to the controversial issue of the Raman active mode assignments of the G<sup>+</sup> and G<sup>-</sup> bands in metallic nanotubes as well as the mode of phonon coupling. The results are consistent with the model of electron-phonon coupling for metallic nanotubes.

# Chapter 2

## Structure and Synthesis of Single Walled Carbon Nanotubes

### 2.1 Introduction

Single walled carbon nanotubes are cylindrical structures based on the hexagonal lattice of  $sp^2$  carbon atoms that form crystalline graphite. An isolated SWCNT can be visualised as the seamless cylinder obtained when a graphene sheet is rolled up (Dresselhaus *et al.* 2005). There are many ways to roll up a graphene sheet into a cylinder, resulting in different diameters and microscopic structure of the tubes. Typical diameters of carbon nanotubes are in the range 0.7-10 nm. The length to diameter ratio of a carbon nanotube can be as large as  $10^4$ - $10^5$ ; hence nanotubes can be considered as 1D nanostructures.

#### 2.1.1 Chiral Vector

The chiral vector  $\mathbf{C}_h$  determines the structure of a SWCNT (Saito *et al.* 1998). It corresponds to the unrolled section of the nanotube perpendicular to the nanotube axis, as shown in Fig 2.1. This vector determines the diameter, as well as the electronic properties of the SWCNTs. It can be represented in real space by the

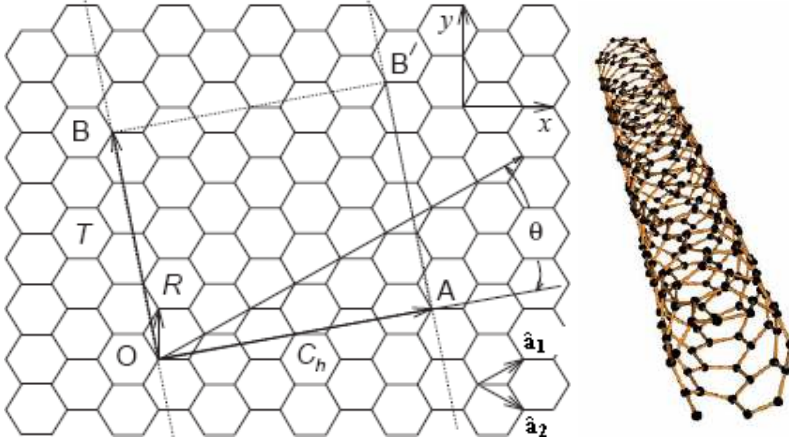


**Figure 2.1:** Unrolled 2D lattice of a single walled carbon nanotube. A seamless nanotube is constructed if sites  $O$  and  $A$ , and  $B$  and  $B'$  are connected.  $\mathbf{OA}$  is the chiral vector  $\mathbf{C}_h$  and  $\mathbf{OB}$  defines the translational vector  $\mathbf{T}$  (after Dresselhaus *et al.* 2005).

equation

$$\mathbf{C}_h = n\hat{\mathbf{a}}_1 + m\hat{\mathbf{a}}_2 \equiv (n, m) \quad (2.1)$$

where  $\hat{\mathbf{a}}_1$  and  $\hat{\mathbf{a}}_2$  are unit vectors of the hexagonal lattice (Fig 2.1) and are expressed as

$$\hat{\mathbf{a}}_1 = \left( \frac{\sqrt{3}}{2}a, \frac{a}{2} \right), \quad \hat{\mathbf{a}}_2 = \left( \frac{\sqrt{3}}{2}a, -\frac{a}{2} \right) \quad (2.2)$$

in which  $a$  is the lattice constant of 2D graphite. The integers  $n$  and  $m$  determine the diameter and electronic properties of the nanotubes. If  $n - m = 3p$ , where  $p$  is an integer, the nanotube is metallic, otherwise it is semi-conducting.

The diameter of the nanotube is obtained from the length of the chiral vector, and can be expressed as

$$d_t = \frac{\sqrt{3}}{\pi} (n^2 + m^2 + mn)^{\frac{1}{2}} a_{C-C} \quad (2.3)$$

where  $a_{C-C}$  is the nearest neighbour carbon-carbon distance.

### 2.1.2 Chiral Angle, $\theta_c$

The chiral angle is defined as the angle of the hexagon helix around the tube axis. It lies between  $0^\circ$  and  $30^\circ$ . From Fig 2.1 can be seen that

$$\mathbf{C}_h \cdot \hat{\mathbf{a}}_1 = |\mathbf{C}_h| |\hat{\mathbf{a}}_1| \cos \theta_c \quad (2.4)$$

and therefore

$$\cos \theta_c = \frac{2n + m}{2\sqrt{n^2 + m^2 + nm}}. \quad (2.5)$$

Carbon nanotubes are classified as being either chiral or achiral. An achiral tube is one whose mirror image has an identical structure to the original one. There are two types of achiral nanotubes, armchair and zigzag. For armchair nanotubes, the chiral indices are equal,  $n = m$  and the chiral angle  $\theta_c = 30^\circ$ . Zigzag tubes exhibit a zigzag pattern along the circumference, and they are of type  $(n, 0)$ , and the chiral angle  $\theta_c = 0^\circ$  (Figure 2.2).

Chiral nanotubes have a spiral symmetry whose mirror image cannot be superposed on to the original one. The chiral angle lies between  $0^\circ$  and  $30^\circ$  (Figure 2.2).

### 2.1.3 Translational Vector

The translational vector is defined as the unit vector of the 1D carbon nanotube (Saito *et al.* 1998). It runs parallel to the nanotube axis and is normal to the chiral vector. The translational vector and the chiral vector define the unit cell of the carbon nanotube (Figure 2.1). The translational vector is expressed in terms of the basis vectors and as

$$\mathbf{T} = t_1 \hat{\mathbf{a}}_1 + t_2 \hat{\mathbf{a}}_2 \quad (2.6)$$

where  $t_1$  and  $t_2$  are integers whose values can be calculated from the equation

$$\mathbf{C}_h \cdot \mathbf{T} = 0. \quad (2.7)$$



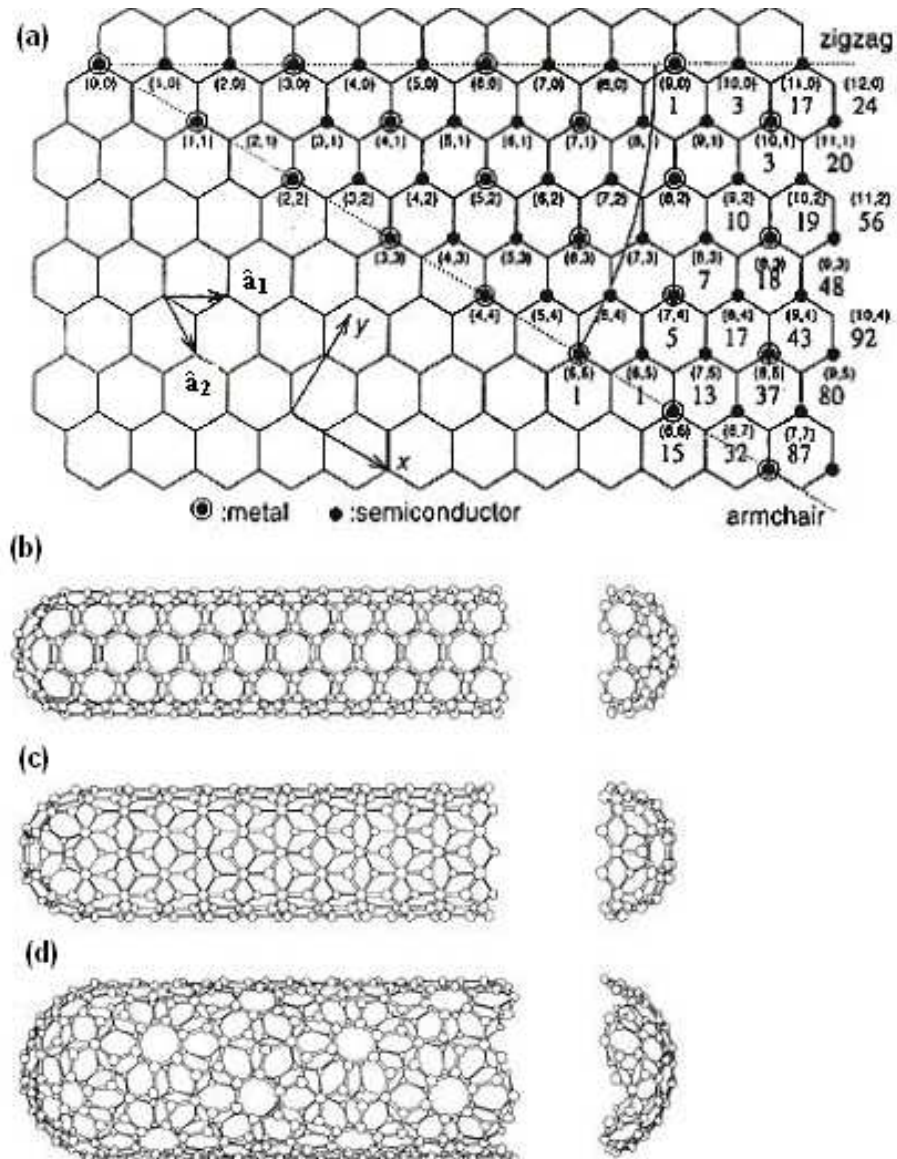


**Figure 2.2:** (a) A graphene sheet when a SWCNT is unrolled showing possible ways of rolling the graphene sheet and the chirality of SWCNTs obtained. (b) armchair, (c) zigzag and (d) chiral nanotube (from <http://students.chem.tue.nl>).

The number of carbon atoms in a nanotube unit cell is obtained by dividing the area of the nanotube unit cell by the area of the unit cell of 2D graphite. The number of hexagons  $N$  in a nanotube unit cell is obtained from

$$N = \frac{|\mathbf{C}_h \times \mathbf{T}|}{|\hat{\mathbf{a}}_1 \times \hat{\mathbf{a}}_2|} \quad (2.8)$$

Since each hexagon contains two carbon atoms, there are  $2N$  carbon atoms per unit cell of the nanotube.

## 2.2 Electronic Structure of Carbon Nanotubes

The electronic properties of carbon nanotubes are derived directly from those of 2D graphite. In order to get a clear understanding of these properties a discussion of bonding in carbon, and a tight binding description of 2D graphite will be given first.

### 2.2.1 Bonding and Hybridization in Carbon

Carbon is the sixth element of the periodic table and the six electrons in carbon occupy the  $1s^2$ ,  $2s^2$  and  $2p^2$  atomic orbitals. The  $2p$  orbital can be split into three possible sub-orbitals,  $2p_x$ ,  $2p_y$  and  $2p_z$  (Reynolds, 1998).

The electronic wave vectors of the four valence electrons can mix with each other, resulting in a change of the occupation of the  $2s$  and three  $2p$  atomic orbitals so as to enhance the binding energy of the carbon atom with its neighboring atoms. When one  $2s$  electron mixes with  $n$  electrons from the three  $2p$  atomic orbitals, then  $sp^n$  hybridization takes place, where  $n = 1, 2, 3$ .

Molecular orbitals are formed from the combination of two or more atomic orbitals. A  $\sigma$  molecular orbital is formed by the lateral overlap of two  $sp$  hybrid orbitals, and a  $\pi$  orbital formed by the side to side overlap of the  $sp$  hybrid orbitals.

In graphite each carbon atom is bonded to three other carbon atoms forming a layer of flat hexagons. The distance between two neighbouring carbon atoms within

the layer is 0.142 nm. Graphite is made up of several of these layers arranged on top of each other about 0.335 nm apart. These layers are bonded together by weak van der Waal's forces.

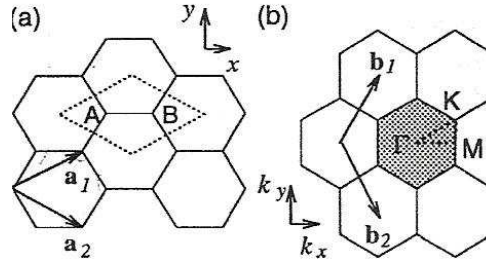


**Figure 2.3:** (a) The unit cell of two dimensional graphite represented by the dotted rhombus and (b) The shaded hexagon shows the Brillouin zone of 2D graphite (after Dresselhaus *et al.* 2005).

Figure 2.3 shows the unit cell and the Brillouin zone of 2D graphite.  $\mathbf{a}_1$  and  $\mathbf{a}_2$  are the lattice vectors in real space and  $\mathbf{b}_1$  and  $\mathbf{b}_2$  are the reciprocal lattice vectors. The points  $\Gamma$ ,  $K$  and  $M$  are the high symmetry points of the Brillouin zone of 2D graphite. Energy dispersion relations for graphite are calculated for the dotted triangle  $\Gamma MK$  shown in the diagram. In 2D graphite the  $2p_z$  orbital is involved in the perpendicular  $\pi$  covalent bonding. The  $\pi$  energy bands are responsible for the electronic properties of 2D graphite.

### 2.2.2 Tight Binding Approach in 2D Graphite

There are basically two approaches to calculate the energy bands of a material. The free electron model assumes that electrons in a material move as free particles. They feel the periodic potential produced by atoms and they interact with other electrons. In the tight binding (TB) model, electrons are considered as part of atoms forming the solid and there are interactions between valence electrons from different atoms (Reich *et al.* 2004).

Reich *et al.* (2004) calculated the electronic band structure of the graphene  $\pi$

orbitals using the TB model, by solving the Schrödinger's equation

$$H\psi(\mathbf{k}) = E(\mathbf{k})\psi(\mathbf{k}) \quad (2.9)$$

where  $H$  is the Hamiltonian,  $E(\mathbf{k})$  are the eigenvalues and  $\psi(\mathbf{k})$  are the eigenfunctions.

The eigenfunctions can be written as a linear combination of Bloch functions  $\phi_l(\mathbf{k})$ , namely

$$\psi(\mathbf{k}) = \sum_l C_l \phi_l(\mathbf{k}). \quad (2.10)$$

The Bloch functions  $\phi_l(k)$  can be written as a linear combination of the atomic wave functions. Graphene has two carbon atoms in its unit cell labelled A and B (Fig 2.2 (a)). The Bloch function for the graphene sub lattice at A or B can be written as

$$\phi_\alpha = \frac{1}{\sqrt{N}} \sum_{\mathbf{R}_\alpha} e^{i\mathbf{k}\cdot\mathbf{R}_\alpha} \varphi(\mathbf{r} - \mathbf{R}_\alpha), (\alpha = A, B) \quad (2.11)$$

where  $\varphi(\mathbf{r})$  denotes the atomic wave function at of the atom at position  $\mathbf{r}$ ,  $N$  is the number of unit cells in the solid and  $\mathbf{R}_\alpha$  is a lattice vector.

To solve the Schrödinger equation of equation(2.9) we substitute  $\psi$  by the linear combination of the Bloch functions in equation(2.10), and multiplying both sides with  $\phi_A$  and  $\phi_B$  we obtain

$$C_A [H_{AA}(\mathbf{k}) - E(\mathbf{k})S_{AA}(\mathbf{k})] + C_B [H_{AB}(\mathbf{k}) - E(\mathbf{k})S_{AB}(\mathbf{k})] = 0 \quad (2.12)$$

$$C_A [H_{BA}(\mathbf{k}) - E(\mathbf{k})S_{BA}(\mathbf{k})] + C_B [H_{BB}(\mathbf{k}) - E(\mathbf{k})S_{BB}(\mathbf{k})] = 0 \quad (2.13)$$

where  $H_{IJ}$  are the matrix elements of the Hamiltonian and  $S_{IJ}$  are the overlaps between the Bloch functions.

Since the two carbons at A and B in the graphene unit cell are identical, the Hamiltonian matrix element  $H_{AA}$ , given by the interaction of an atom at site A with itself and all other A atoms in the crystal, is exactly the same as  $H_{BB}$ . Similarly  $H_{BA}$  is the complex conjugate of  $H_{AB}$ .

The system of linear equations in equation(2.12) has a non trivial solution if the determinant  $\det[H - ES] = 0$ . Therefore the general form of the secular equation for the  $\pi$  orbitals of graphene is

$$\begin{vmatrix} H_{AA}(\mathbf{k}) - E(\mathbf{k})S_{AA}(\mathbf{k}) & H_{AB}(\mathbf{k}) - E(\mathbf{k})S_{AB}(\mathbf{k}) \\ H_{AB}^*(\mathbf{k}) - E(\mathbf{k})S_{AB}^*(\mathbf{k}) & H_{AA}(\mathbf{k}) - E(\mathbf{k})S_{AA}(\mathbf{k}) \end{vmatrix} = 0$$

where

$$\begin{aligned} H_{AA}(k) &= \langle \phi_A | H | \phi_{A'} \rangle \\ &= \frac{1}{N} \sum_{\mathbf{R}_A} \sum_{\mathbf{R}_{A'}} \langle e^{i\mathbf{k}\cdot\mathbf{R}_A} \varphi(\mathbf{r} - \mathbf{R}_A) | H | e^{i\mathbf{k}\cdot\mathbf{R}_{A'}} \varphi(\mathbf{r} - \mathbf{R}_{A'}) \rangle. \end{aligned} \quad (2.14)$$

The first sum is over all N carbon atoms of type A in the graphene sheet. We want to include only the interaction with the first-nearest neighbours of each atom. All three nearest neighbours, however, belong to the B sub lattice, hence for a given  $\mathbf{R}_A$ , the second sum has only a single term,  $\mathbf{R}_{A'} = \mathbf{R}_A$ .

$$\begin{aligned} H_{AA}(k) &= \frac{1}{N} \sum_{\mathbf{R}_A} e^{i\mathbf{k}\cdot(\mathbf{R}_A - \mathbf{R}_A)} \langle \varphi_A(\mathbf{r} - \mathbf{R}_A) | H | \varphi_A(\mathbf{r} - \mathbf{R}_A) \rangle \\ &= \frac{1}{N} N \cdot \langle \varphi_A(\mathbf{r} - \mathbf{R}_A) | H | \varphi_A(\mathbf{r} - \mathbf{R}_A) \rangle \\ &= \epsilon_{2p}. \end{aligned} \quad (2.15)$$

Similarly

$$\begin{aligned} H_{AB} &= \langle \psi_A | H | \psi_B \rangle \\ &= t(e^{i\mathbf{k}\cdot\mathbf{R}_{11}} + e^{i\mathbf{k}\cdot\mathbf{R}_{12}} + e^{i\mathbf{k}\cdot\mathbf{R}_{13}}) \\ &= tf(k) \end{aligned} \quad (2.16)$$

where  $t = \langle \psi_A(\mathbf{r} - \mathbf{R}_A) | H | \psi_B(\mathbf{r} - \mathbf{R}_B) \rangle$  and  $\mathbf{R}_{1i}$  ( $i=1,2,3$ ) is the position of the three nearest neighbours.

$$S_{AA} = S_{BB} = 1 \text{ and}$$

$$S_{AB} = s(e^{i\mathbf{k}\cdot\mathbf{R}_{11}} + e^{i\mathbf{k}\cdot\mathbf{R}_{12}} + e^{i\mathbf{k}\cdot\mathbf{R}_{13}}) \quad (2.17)$$

where  $s = \langle \psi_A | \psi_B \rangle$ .

Therefore  $H$  and  $S$  can be explicitly expressed as

$$\begin{bmatrix} \epsilon_{2p} & tf(k) \\ tf(k)^* & \epsilon_{2p} \end{bmatrix}, \quad \begin{bmatrix} 1 & sf(k) \\ sf(k)^* & 1 \end{bmatrix}$$

respectively.

Solving the secular equation  $\det|H - ES| = 0$ , the eigenvalues  $E(\mathbf{k})$  are obtained as

$$E_{g2D}(k) = \frac{\epsilon_{2p} \pm t\omega(\mathbf{k})}{1 \pm s\omega(\mathbf{k})} \quad (2.18)$$

where  $\omega(\mathbf{k}) = \sqrt{|f(\mathbf{k})|^2}$ .

The + signs in the numerator and denominator give the bonding  $\pi$  energy band and the - signs give the anti-bonding  $\pi^*$  band.

Figure 2.4 shows the energy dispersion relations of 2D graphite along the high symmetry axis of the Brillouin zone. The upper graph in the insert shows the  $\pi^*$ -energy anti bonding band and the lower graph shows the  $\pi$ - energy bonding band. The  $\pi$  and  $\pi^*$  energy bands are degenerate at the K points where the Fermi level crosses. As a result 2D graphite is a zero band gap semi-conductor, with an occupied  $\pi$  band and an empty  $\pi^*$  band.

### 2.2.3 Bonding in Carbon Nanotubes

In carbon nanotubes there are  $\sigma$  bonds along the nanotube walls and  $\pi$  bonds perpendicular to the nanotube surface. The  $\pi$  bonds contribute mostly to the electronic properties of SWCNTs (Dresselhaus *et al.* 2005). The  $\pi$  bonds are also responsible for the weak van der Waal's interactions between nanotubes. Because electrons lie close to the Fermi level, they can be excited from the valence ( $\pi$ ) band to the conduction ( $\pi^*$ ) band optically. Around the Fermi level the  $\pi$  bands are linear to a good approximation. Optical transitions occur close to the K points of a Brillouin zone, where the valence and conduction bands are degenerate.

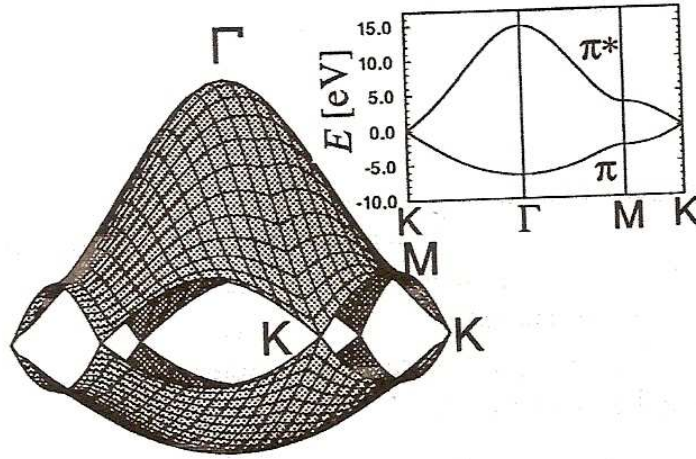


**Figure 2.4:** Energy dispersion relation of 2D graphite throughout the whole Brillouin zone. The insert shows the energy dispersion along the high symmetry points  $\Gamma$ ,  $M$  and  $K$  (after Saito et al. 1998).

### 2.2.4 Electronic Structure of Carbon Nanotubes

The electronic properties of carbon nanotubes are very sensitive to the tubes' geometric structure (Louie 2001). A nanotube can either be metallic or semi-conducting depending on the diameter and chirality of the tube. When forming a carbon nanotube from a graphene sheet, only certain states of the 2D graphite sheet are allowed, due to the periodic boundary conditions introduced in the tube circumferential direction. Therefore, electronic states are restricted to  $\mathbf{k}$  vectors that satisfy the condition

$$\mathbf{K} \cdot \mathbf{C}_h = 2\pi q$$

where  $q$  is an integer. The periodic boundary conditions for a carbon nanotube give  $N$  discrete  $k$  values in the circumferential direction.

If the allowed wave vectors of a nanotube are plotted onto the Brillouin zone of graphene, a series of parallel lines are obtained. The length, number and orientation of these parallel lines depends on the chiral indices  $(n, m)$  of the tube. Figure 2.5(a) shows these allowed lines.  $\mathbf{K}_1$  and  $\mathbf{K}_2$  are the reciprocal lattice vectors in the circumferential direction and along the nanotube axis respectively. These can be

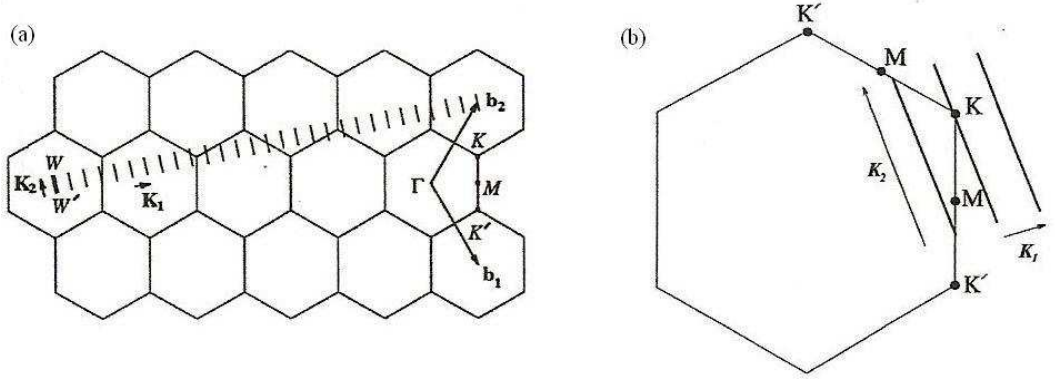


**Figure 2.5:** (a) The Brillouin zone of a carbon nanotube represented by the line segment  $WW'$ . (b) An expanded view of the graphite 2D Brillouin zone showing the allowed  $\mathbf{k}$  vectors for one dimensional nanotubes. One of the lines intersects a  $K$  point making the tube metallic ((a) after Saito *et al.* 1998 and (b) after Saito and Kataura 2001).

obtained from the relation

$$\mathbf{R}_i \cdot \mathbf{K}_j = 2\pi\delta_{ij}$$

where  $\mathbf{R}_i$  and  $\mathbf{K}_j$  are respectively the lattice vectors in real and reciprocal space. It therefore follows that

$$\begin{aligned} \mathbf{C}_h \cdot \mathbf{K}_1 &= 2\pi; & \mathbf{T} \cdot \mathbf{K}_1 &= 0 \\ \mathbf{C}_h \cdot \mathbf{K}_2 &= 0; & \mathbf{T} \cdot \mathbf{K}_2 &= 2\pi. \end{aligned} \quad (2.19)$$

Thus

$$\begin{aligned} \mathbf{K}_1 &= \frac{1}{N}(-t_2\mathbf{b}_1 + t_1\mathbf{b}_2), \\ \mathbf{K}_2 &= \frac{1}{N}(m\mathbf{b}_1 - n\mathbf{b}_2). \end{aligned} \quad (2.20)$$

Figure 2.5(b) shows the Brillouin zone of 2D graphite and the allowed parallel lines (allowed  $\mathbf{k}$  vectors). If a particular line intersects with the  $K$  point of the 2D graphite Brillouin zone (Fig 2.5(b)), where the  $\pi$  and  $\pi^*$  energy bands are degenerate, then the 1D energy bands have a zero energy gap and the nanotube will be metallic. The  $K$  point of a graphene sheet is found at

$$\frac{1}{3}(\mathbf{b}_1 - \mathbf{b}_2).$$



Therefore a nanotube is metallic if

$$\begin{aligned}
 \mathbf{K} \cdot \mathbf{C}_h &= 2\pi q \\
 &= \frac{1}{3}(\mathbf{b}_1 - \mathbf{b}_2)(n\mathbf{a}_1 + m\mathbf{a}_2) \\
 &= \frac{2\pi}{3}(n - m).
 \end{aligned} \tag{2.21}$$

Hence a nanotube is metallic if  $n - m = 3p$ , where  $p$  is an integer, otherwise it is semi-conducting.

The electronic band structure of carbon nanotubes is obtained from the zone folding of the band structure of graphene (Popov 2004). The basic idea of zone folding is that the electronic band structure of a nanotube is given by the graphene electronic energies along the allowed  $k$  lines. The 1D dispersion relations for single-wall nanotubes is given by

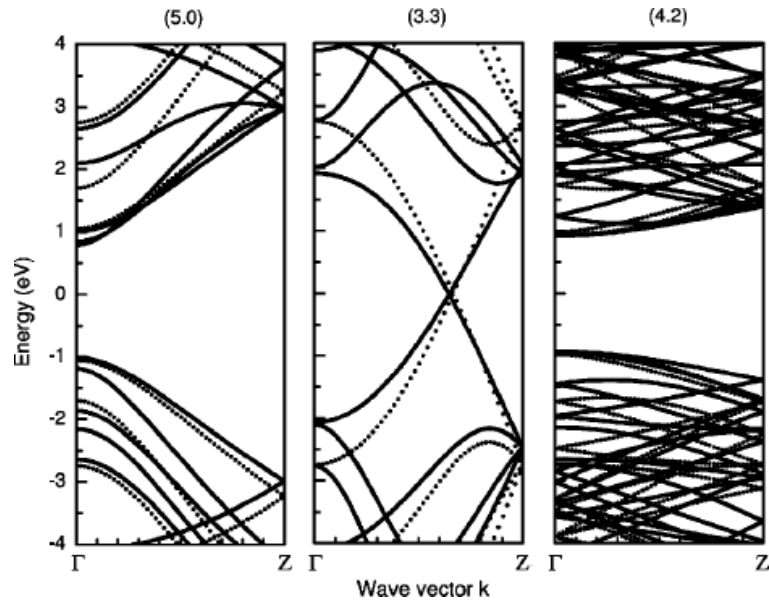
$$E_\mu(k) = E_{g2D}(k \frac{\mathbf{K}_2}{|\mathbf{K}_2|} + \mu\mathbf{K}_1), (\mu = 0, \dots, N - 1, \quad -\frac{\pi}{T} < k < \frac{\pi}{T}). \tag{2.22}$$

Figure 2.6 shows the electronic band structure of three different types of SWCNTs. The valence and conduction band of the (3,3) nanotube cross at the Fermi level. This means that the (3,3) nanotube has a zero band-gap and as a result it shows metallic properties.

## 2.3 Synthesis of Carbon Nanotubes

### 2.3.1 Introduction

There are basically three main techniques of synthesising carbon nanotubes. These are the electric arc-discharge method (EA discharge), laser ablation and chemical vapour deposition (CVD). The EA discharge method was the first technique used to produce carbon nanotubes (Iijima 1991). Its advantage is that it can produce SWCNTs and multi-wall nanotubes (MWCNTs) with few structural defects. However, it produces tubes that are very short and are randomly oriented. Depending on the catalyst used and the growth conditions, EA discharge tubes can have a purity of about 70% (Zhao *et al.* 2003).



**Figure 2.6:** Calculated electronic band structure of nanotubes (5,0), (3,3), and (4,2) in the energy range between -4 and 4 eV with respect to the Fermi energy within the orthogonal-tight binding model (full lines) and the  $\pi$ -band tight binding model (dotted lines)(after Popov and Henrard 2004).

The laser ablation method has a yield of up to 70% and produces both SWCNTs and MWCNTs of larger diameters in large quantities. The disadvantage of this method is that it is expensive because high power lasers are required.

The CVD method has a yield of 20 to 100%, and can be used for production of nanotubes with long length in large quantities, but the tubes are structurally more defective than the EA discharge or laser ablation methods.

### 2.3.2 Electric Arc Discharge Method

This is the most common way of synthesizing carbon nanotubes. In this method nanotubes are produced by the arc vaporisation of a graphite anode into an inert gas plasma.

Two graphite electrodes are placed end to end about 2mm apart in the arc discharge chamber. The anode is loaded with a catalyst, typically of a transition metal. The catalyst is essential for SWCNT growth. Without the catalyst, the by-

products of the EA discharge process are MWCNTs and fullerenes. The discharge chamber is filled with an inert gas, typically argon or helium at low pressure. It is also possible to use a mixture of gases. Zhao *et al.* (2003) used a hydrogen-argon gas mixture and 1 at% Fe catalyst and obtained SWNTs of very high purity.

The two graphite electrodes are subjected to a high current discharge which produces an arc that then vaporises the anode. The produced carbon nanotubes collect on the cathode tip and on the walls of the chamber. The quality of the produced nanotubes depends on the uniformity of the plasma arc, the metal concentration in the catalyst used, the inert gas pressure and the type of gas used (Tarasov *et al.* 2003) and the geometry of the arc discharge system (Journet and Bernier 1998). A detailed study of the EA discharge synthesis of SWCNTs will be given in Chapter 5.

### 2.3.3 Laser Ablation Method

This method involves the laser vaporisation of a carbon target containing small percentages of Ni and Co as catalysts. The target is placed in a tube furnace and temperatures in the furnace can be as high as 1200°C. During the growth process, a flow of inert gas is maintained through the growth chamber to carry the grown nanotubes to be collected at the cold end of the chamber. Figure 2.7 shows a schematic diagram of the laser ablation system for nanotube growth.

The detailed growth process of carbon nanotubes is not well understood. One of the proposed mechanisms of growth, which applies to both laser ablation and EA discharge is called the scooter model (Guo *et al.* 1995; Thess *et al.* 1996; Scott *et al.* 2001). In this model, the atoms of the catalyst attach themselves to a fullerene or a graphene sheet. The catalyst atom prevents the closing of the fullerene as carbon dimers and trimers ( $C_2$  and  $C_3$ ) attach, leading to the formation of tubes.

A single catalyst atom or a group of atoms circulate around the open end of the nanotube adsorbing small carbon molecules and converting them into a tube. Termination of the growth of the tube occurs when too many catalyst atoms aggregate

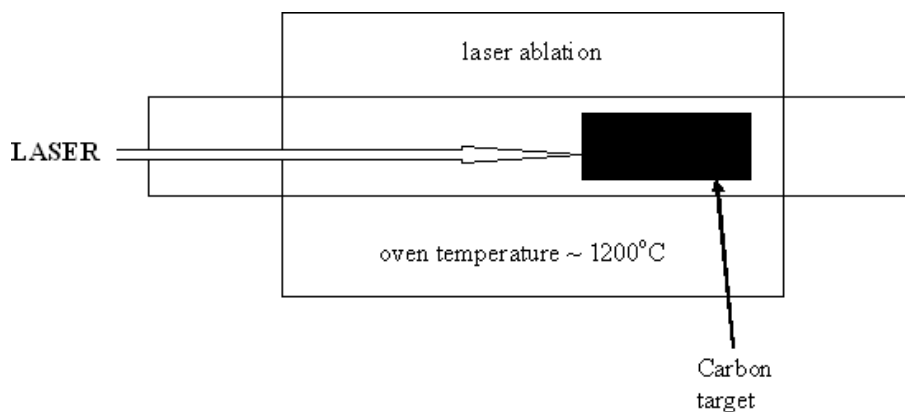


**Figure 2.7:** Schematic diagram of the laser ablation arrangement for carbon nanotube synthesis (after Dai 2001).

on the end of the nanotube or with the attachment of  $C_5$  carbon pentagons to the open ends of the tube (Charlier and Iijima 2001).

In another model, Kataura *et al.* 2000 have suggested that SWCNTs grow from metal particles saturated with carbon, figure 2.8. In this model, at high temperatures of about  $3000^{\circ}\text{C}$ , small carbon clusters having fullerene like structures nucleate (Step 1). As the system cools down, metal atoms from the catalyst condense forming particles or droplets which become saturated with carbon. These particles or droplets get covered with the fullerene like carbon fragments with the open ends sticking to the metal particles to eliminate the unstable dangling bonds (Step 2). These fullerene like fragments act as precursors for SWCNTs growth, with the carbon being supplied from the precipitation from the metal-carbon mixture or the surrounding disordered carbon.

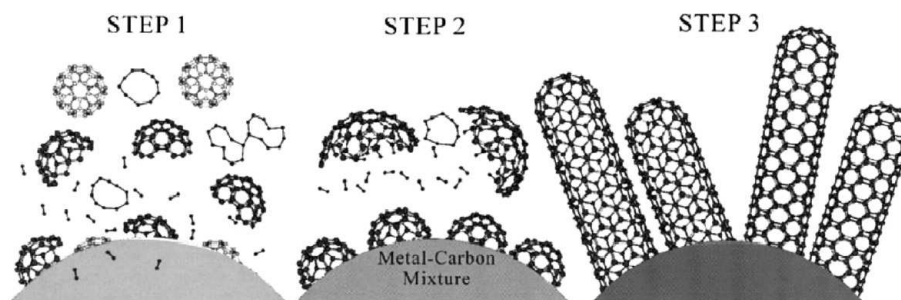


**Figure 2.8:** Growth mechanisms for SWCNTs proposed by Kataura *et al.* 2000.

### 2.3.4 Chemical Vapour Deposition Method

Chemical vapour deposition (CVD) is one of the methods commonly used to synthesize carbon nanotubes (Cheng *et al.* 1998; Nikolaev *et al.* 1999). In this method a catalyst material is heated to temperatures of up to  $1200^{\circ}\text{C}$ . The catalysts that are normally used are transition metal nanoparticles grown on a support material. A hydrocarbon gas, typically methane or ethylene is passed through the tube reactor. This gas is the source of carbon for the CVD process. Due to the high molecular stability of hydrocarbon gases, they only decompose at catalyst sites. This results in low amounts of amorphous carbon being produced.

The growth mechanism of SWCNTs during CVD involves the dissociation of hydrocarbon molecules at the catalyst site (Dai 2001). This is followed by the dissolution and saturation of carbon atoms in the metallic nanoparticle. Precipitation of carbon atoms from the saturated material leads to the formation of carbon nanotubes. The carbon nanotubes can grow on metal particles supported on a substrate, called base growth, or on a floating metal particle, called tip growth.

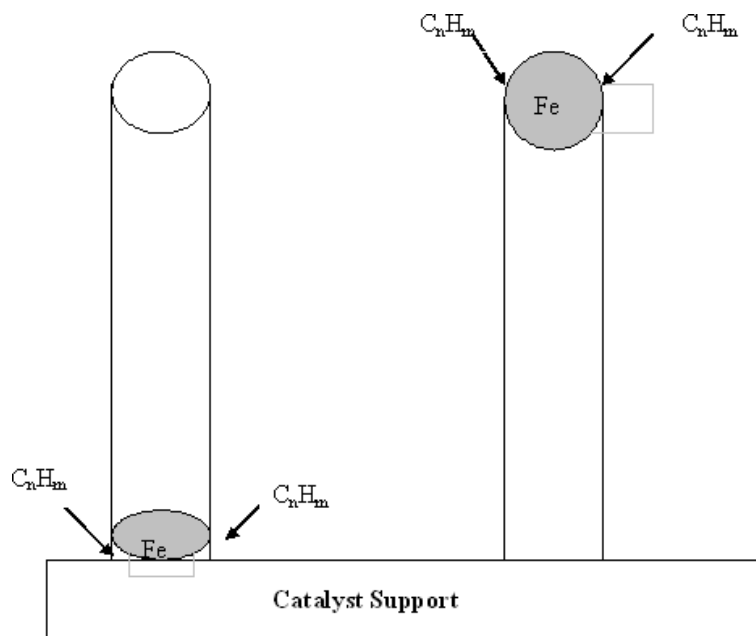


**Figure 2.9:** Two general growth modes of nanotubes in CVD. Left: base growth mode. Right: tip growth mode (after Dai 2001).

The CVD method can be used on a large scale, and can work at lower temperatures compared to EA discharge and laser ablation. Ultralong isolated nanotubes that are about 4 cm long have been synthesized using this method (Zheng *et al.* 2004). This was a big breakthrough because of the need for long isolated tubes for applications such as fibres and other technological applications.

However, the disadvantage of CVD is that it produces nanotubes with more defects compared to EA discharge and laser ablation.

# Chapter 3

## Raman Scattering

### 3.1 Introduction

When monochromatic light impinges on a sample, some of it is transmitted, some absorbed and some of it is scattered by the material. Most of the scattered light has essentially the same frequency as the incident light. This light is said to be Rayleigh scattered. However, some of the photons will be scattered with different energies from the incident photons. This inelastic scattering of the light is called Raman scattering (Hayes 1975). It occurs with a change in vibrational, rotational or electronic energy of the sample. The Raman spectrum of a sample shows discrete frequencies both higher and lower than the exciting radiation frequency. These frequencies are called Raman bands and those bands lower in frequency than the exciting radiation are called Stokes lines while those with higher frequencies are called anti-Stokes lines.

The frequency shift of the scattered photons from the incident photons is characteristic of excitations within the sample. This is a property which makes Raman spectroscopy a powerful, non destructive technique for identifying and characterizing materials.

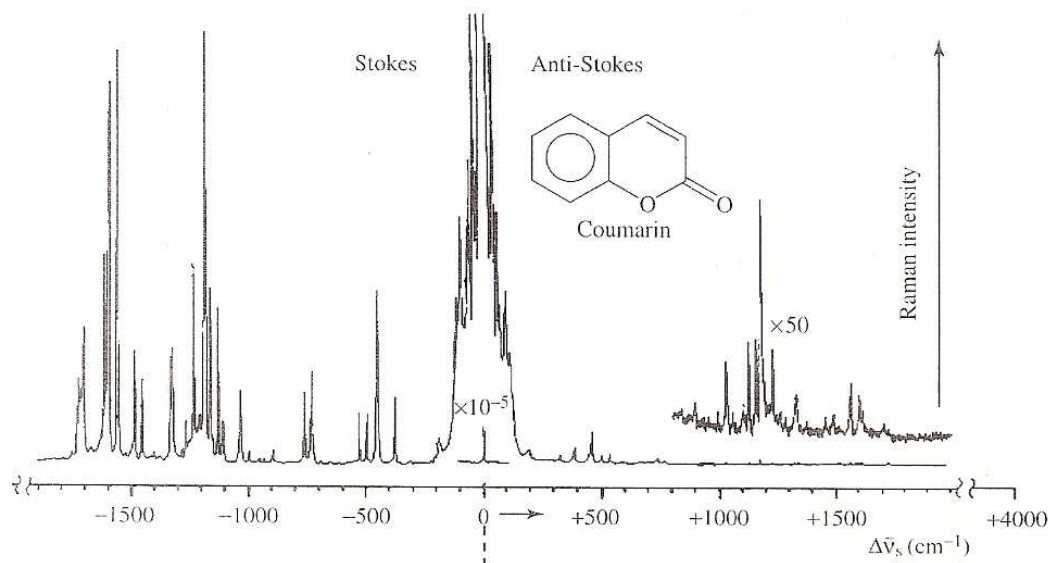


**Figure 3.1:** A typical Raman spectrum of a polycrystalline material (coumarin) showing the Rayleigh line, and both the Stokes and anti-Stokes sides of the Raman spectrum (from Keresztury, 2002).

## 3.2 Raman Scattering Process

Raman scattering can be described in two ways, using the classical approach or the quantum mechanical approach.

### 3.2.1 Classical Approach

This approach assumes that the Raman effect arises from the interaction of the incident photon and the electric dipole of the molecule. The electric field of the incident light causes a perturbation of the molecule's dipole moment. The elastically (Rayleigh) scattered light is therefore generated by the oscillating electric dipoles induced by the electric field of the incident radiation. The inelastically scattered light is a result of the modulation of the polarizability of the scattering molecules by the internal excitations (Keresztury 2002). This discussion will focus on Raman scattering by the vibrational modes of molecules.

The relationship between the induced dipole moment vector  $\mu$  and the electric



field vector  $\mathbf{E}$  is given by the power series

$$\mu = \alpha\mathbf{E} + \frac{1}{2}\beta\mathbf{E}\mathbf{E} + \frac{1}{6}\gamma\mathbf{E}\mathbf{E}\mathbf{E} + \dots \quad (3.1)$$

where  $\alpha$  is the polarizability,  $\beta$  the hyperpolarizability and  $\gamma$  the second hyperpolarizability.

The non-linear terms in the above equation are usually very small compared to the first term, as a result they play little role in linear Raman scattering. The expression for the induced dipole moment vector can therefore be simplified to

$$\mu = \alpha\mathbf{E} \quad (3.2)$$

The above equation can be expressed as scalar equations in the form

$$\mu_x = \alpha_{xx}E_x + \alpha_{xy}E_y + \alpha_{xz}E_z$$

$$\mu_y = \alpha_{yx}E_x + \alpha_{yy}E_y + \alpha_{yz}E_z$$

$$\mu_z = \alpha_{zx}E_x + \alpha_{zy}E_y + \alpha_{zz}E_z$$

This can be written in matrix form as

$$\begin{bmatrix} \mu_x \\ \mu_y \\ \mu_z \end{bmatrix} = \begin{bmatrix} \alpha_{xx} & \alpha_{xy} & \alpha_{xz} \\ \alpha_{yx} & \alpha_{yy} & \alpha_{yz} \\ \alpha_{zx} & \alpha_{zy} & \alpha_{zz} \end{bmatrix} \begin{bmatrix} E_x \\ E_y \\ E_z \end{bmatrix}$$

where the nine co-efficients  $\alpha_{ij}$  are the components of the polarizability tensor  $\alpha$ .

Variation of the molecular polarizability on the normal co-ordinates is expressed in terms of the Taylor series

$$\alpha_{ij} = (\alpha_{ij})_0 + \sum \left( \frac{\partial \alpha_{ij}}{\partial Q_k} \right)_0 Q_k + \frac{1}{2} \sum \left( \frac{\partial^2 \alpha_{ij}}{\partial Q_k \partial Q_l} \right) Q_k Q_l + \dots \quad (3.3)$$

where  $(\alpha_{ij})_0$  is the value of the polarizability tensor in the equilibrium position, and  $Q_k$  is the  $k$ th normal co-ordinate associated with vibrations of wavenumber  $\nu_k$ . For small vibrations near the equilibrium position equation (3.3) can be written as

$$\alpha_{\mathbf{k}} = \alpha_0 + \left( \frac{\partial \alpha}{\partial Q_k} \right)_0 Q_k. \quad (3.4)$$

Taking the normal vibrations of the molecule as being harmonic, the time dependence of  $Q_k$  is given by

$$Q_k = Q_{k0} \cos 2\pi\nu_k t \quad (3.5)$$

where  $Q_{k0}$  is the normal coordinate amplitude. The change in the electric field of the incident radiation of frequency  $\nu_0$  with time is given by

$$E = E_0 \cos 2\pi\nu_0 t \quad (3.6)$$

Combining equations (3.2), (3.4), (3.5) and (3.6) the linear induced dipole moment is expressed by

$$\begin{aligned} \mu &= \alpha_0 E + \left( \frac{\partial \alpha}{\partial Q_k} \right)_0 Q_{k0} E_0 \cos 2\pi\nu_0 t \cos 2\pi\nu_k t \\ &= \alpha_0 E + \frac{1}{2} \left( \frac{\partial \alpha}{\partial Q_k} \right)_0 Q_{k0} E_0 [\cos 2\pi(\nu_0 - \nu_k)t + \cos 2\pi(\nu_0 + \nu_k)t] \end{aligned} \quad (3.7)$$

From the above equation it is apparent that the linear induced dipole has three distinct frequency components. The first term  $\alpha_0 E_0 \cos 2\pi\nu_0 t$  describes the Rayleigh scattered light at  $\nu_0$ . The second term  $(\nu_0 - \nu_k)$  represents the Stokes Raman process and the third term  $(\nu_0 + \nu_k)$  represents the anti-Stokes Raman process. The intensity of Raman scattering depends on the derived polarizability tensor  $\alpha_k$ , also called the Raman tensor.

$$\alpha_k = \left( \frac{\partial \alpha}{\partial Q_k} \right)_0. \quad (3.8)$$

It represents the sensitivity of the molecular polarizability to changes of nuclear configuration along the normal co-ordinates of vibrations. For a molecular vibration to be Raman active, at least one component of the polarizability tensor must change during the vibration i.e

$$\left( \frac{\partial \alpha_{ij}}{\partial Q_k} \right)_0 \neq 0. \quad (3.9)$$

### 3.2.2 Quantum Mechanical Approach

In the quantum mechanical approach, Raman scattering is considered as a two photon process (Kuzmany 1998; Thomsen *et al.* 2004). A photon of incident radiation is absorbed, raising the system to a virtual state. This state has a very

short life time ( $10^{-14}s$ ), hence the system makes a downward transition, creating or absorbing a phonon of a given energy and scattering a photon in the process. Rayleigh scattering is when the energy of the scattered and incident photons is the same (Fig 3.2a). If the energy of the scattered photon is less than the energy of the incident photon, this corresponds to Stokes Raman scattering (Fig 3.2b). If the system was initially in an excited state, it can make a transition from the virtual state to a lower energy state than the initial one (Fig 3.2c). Its energy will therefore be higher than that of the incident photon, corresponding to anti-Stokes Raman scattering (Keresztury 2002). For a crystal at room temperature, this effect is very small since the initial excited state has a low occupancy of excited states at room temperature according to Boltzmann statistics.

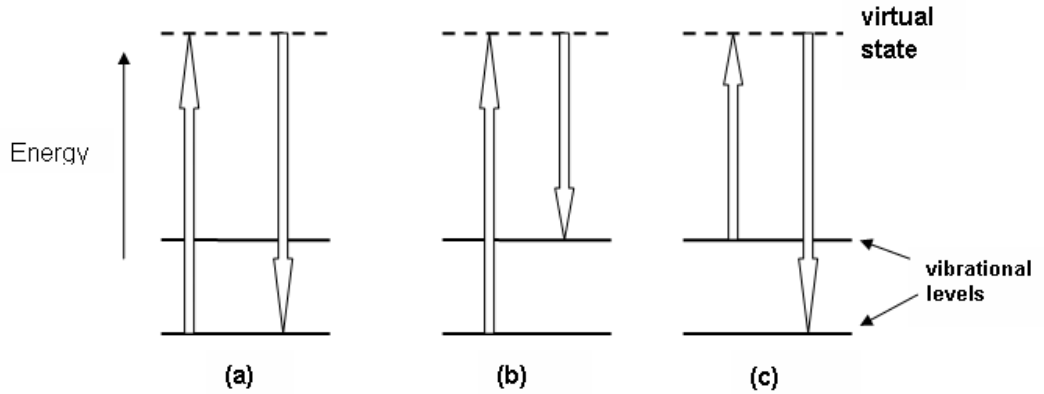


**Figure 3.2:** Energy level diagrams showing (a) Rayleigh scattering, (b) Stokes Raman scattering, and (c) anti-Stokes Raman scattering.

Energy and momentum are conserved in the Raman scattering process. If an incoming photon of frequency  $\omega_i$  causes a phonon of frequency  $\omega_{ph}$  to be created or absorbed in scattering a photon of frequency  $\omega_s$ , then by conservation we have

$$\hbar\omega_i = \hbar\omega_s \pm \hbar\omega_{ph}; \quad \mathbf{q}_i = \mathbf{q}_s \pm \mathbf{q}_{ph}$$

where  $\pm$  represents a Stokes or anti-Stokes process and  $\mathbf{q}_i$ ,  $\mathbf{q}_s$  and  $\mathbf{q}_{ph}$  are the wave vectors of the incident photon, scattered photon and emitted or absorbed phonon, respectively.

### 3.3 Resonant Raman Scattering

Resonance Raman scattering is characterised by the strong enhancement in the intensity of the scattered light. This process occurs when the frequency of the incident light approaches that of an electronic transition or falls inside an electronic absorption band of the sample. This leads to resonances which may significantly enhance the intensities of some Raman lines (Keresztury 2002).

### 3.4 Intensity of Raman Scattering

First order Stokes Raman intensity as a function of phonon energy,  $\hbar\omega$  and laser energy  $E_{laser}$  is given by

$$I(\omega, E_{laser}) = C \left( \frac{E_a}{E_j} \right) [n(q, \mu) + 1] \sum_j \left| \sum_a \frac{M^d(\mathbf{k} - \mathbf{q}, jb) M^{ep}(\mathbf{q}, ba) M^d(\mathbf{k}, aj)}{\Delta E_{aj} (\Delta E_{aj} - \hbar\omega)} \right|^2 \quad (3.10)$$

where  $C$  is a constant,  $n(q, \mu)$  is the number of phonons and

$$\Delta E_{aj} \equiv E_{laser} - (E_a - E_j - i\gamma)$$

and  $j$ ,  $a$  and  $b$  are the initial state, excited state and scattered states respectively, and  $\gamma$  is the broadening factor of the resonant event (Dresselhaus *et al.* 2005).

An electron of wave vector  $\mathbf{k}$  can be excited by the electric dipole interaction represented by  $M^d(\mathbf{k}, aj)$  with the incident photon and makes a transition from  $j$  to  $a$ . It can then be scattered by emitting a phonon of wave vector  $\mathbf{q}$  by an electron-phonon interaction  $M^{ep}(\mathbf{q}, ba)$ . The electron then finally emits a photon by an electric dipole transition, through the interaction represented by  $M^d(\mathbf{k} - \mathbf{q}, jb)$ . Resonance conditions occur either with the incident photon  $E_{laser} = E_{aj}$ , or with the scattered photon  $E_{laser} = E_{aj} + \hbar\omega$ . At resonance, the denominator in the second term in equation (3.10) is a minimum, therefore intensity will be at maximum.

### 3.5 Raman Scattering in Carbon Nanotubes

Raman spectroscopy is a very important tool for characterizing carbon nanotubes. The Raman spectra of carbon nanotubes are unique and distinct due to their one dimensional (1D) nature. The intensity of Raman scattering from carbon nanotubes depends on the density of states (DOS) available for optical transitions (Jorio *et al.* 2003). The DOS structure for a SWCNT can be obtained from the energy dispersion relations of single-walled carbon nanotubes, which are obtained from zone folding of the 2D energy dispersion relations of graphite.

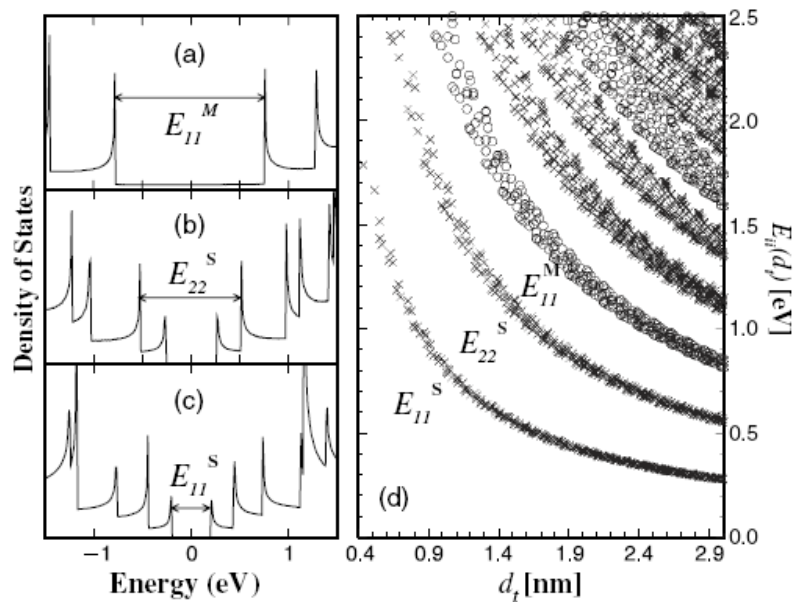


**Figure 3.3:** DOS for three different carbon nanotubes, (a) metallic nanotube, (b) and (c), semi-conducting tubes of different chiralty. The DOS near the Fermi level has a non-zero value for metallic tubes and a zero value for semi-conducting tubes. (d) shows the electronic transition energies  $E_{ii}$  for all  $(n, m)$  SWCNTs in the diameter range 0.4-3.0 nm (after Jorio *et al.* 2003).

The DOS depends largely on the dimensions and energy of the system (Reich *et al.* 2004). This means that different diameter carbon nanotubes have different 1D DOS structures. The DOS are characterized by sharp peaks resulting from van Hove singularities (vHs). vHs are points where the conduction bands and valence bands

are parallel and at these points intensity of absorption is a maximum (Burns 1985). The number of vHs in the DOS spectra depends on the number of  $\pi$  sub-bands,  $2N$ , where  $N$  is the number of carbon atoms in the nanotube unit cell (Saito *et al.*, 1998).

Resonance Raman scattering in carbon nanotubes occurs when the energy of the incident laser ( $E_{laser}$ ) matches the energy separation ( $E_{ii}$ ) between the vHs in the valence and conduction bands. Since  $E_{ii}$  depends on the nanotube structure, it means that nanotubes of different structures and different chiralities will be in resonance with different laser energies. Experimental studies on the dependence of the intensities of Raman vibrational modes of SWCNTs on excitation energy (Pimenta *et al.* 1998; Telg *et al.* 2004; Yin *et al.* 2006) show that peak intensities are strongly dependent on the laser excitation energy. This gives information on what nanotubes are strongly resonant at particular excitation wavelengths. Dresselhaus *et al.* (2006) have also shown that there are significant changes to the shape and position of Raman spectra with changes in excitation energy. The resonant Raman scattering effect is used to characterize the chiralities of SWCNTs and to distinguish between semi-conducting and metallic nanotubes.

### 3.6 Raman Vibrational Modes in SWCNTs

There are three major Raman vibrational features of single-walled carbon nanotubes that were studied in this work. These are the radial breathing mode (RBM), the tangential modes (G-bands) and the disorder induced D-band. Experimental work by several workers on isolated SWCNTs (Jorio *et al.* 2002a); Jorio *et al.* (2002b); Zhang *et al.* (2007)) have shown that one can excite both the RBM and the G-band for an isolated SWCNT. This indicates that in a bundle of SWCNTs, the RBM and the G-bands originate from the same tubes. The data and discussions by Jorio *et al.* (2004) also treats RBM and G-bands as originating from the same nanotube for both isolated SWCNTs and in bundles.

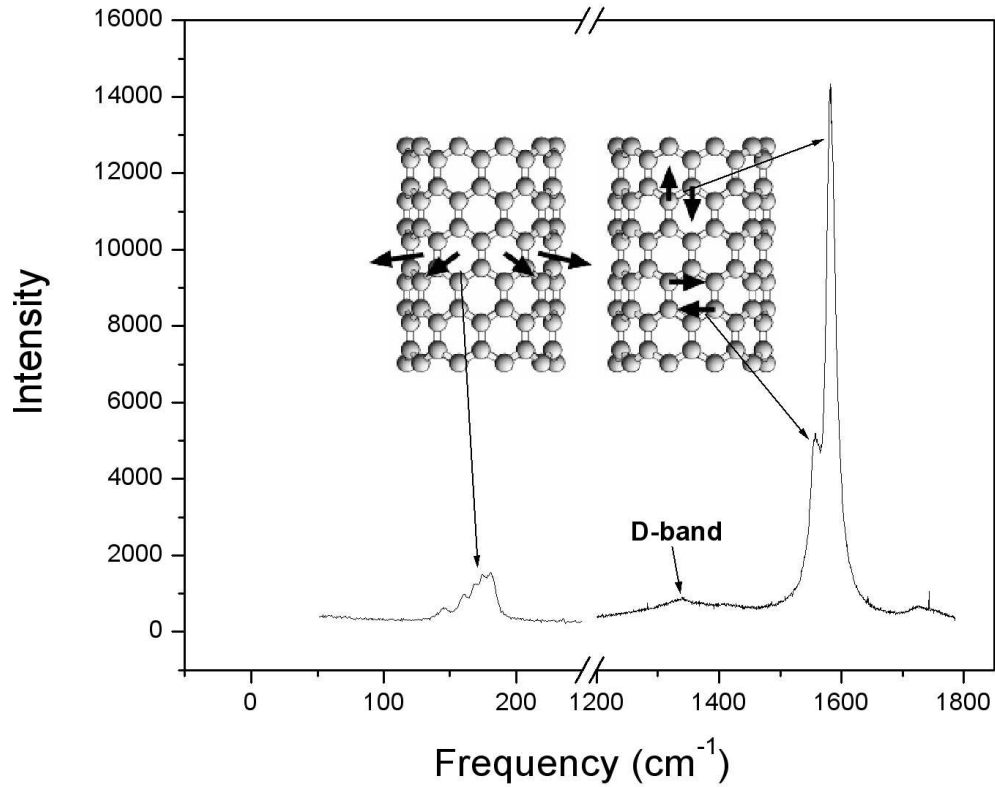


**Figure 3.4:** Raman vibrational modes in semi-conducting SWCNTs showing the radial vibrations of C-atoms giving rise to the radial breathing mode (RBM), the G band, with C-atom vibrations along nanotube axis (LO mode) and tangential to the circumference of the nanotube (TO mode) and the disorder induced D-band.

### 3.6.1 Radial Breathing Mode (RBM)

The RBM results from the coherent vibrations of carbon atoms of each nanotube in the radial direction, as shown by Figure 3.4. It normally appears at frequencies between 120 and 250  $\text{cm}^{-1}$  for nanotubes in the diameter range 1-2 nm. The presence of this feature in a sample of nanotubes indicates the presence of single-walled carbon nanotubes as this feature is unique to such tubes. The RBM can be used for diameter characterization using its frequency  $\omega_{RBM}$ , studying the electronic structure and for chirality assignment.

The RBM frequency  $\omega_{RBM}$  depends linearly on the reciprocal of the nanotube

diameter  $d_t$  and is related to it by the formula

$$\omega_{RBM}(cm^{-1}) = \frac{C(cm^{-1}nm)}{d_t(nm)} + D(cm^{-1}) \quad (3.11)$$

The values of the constants  $C$  and  $D$  are determined experimentally. For isolated SWCNTs  $C = 223.75 \text{ cm}^{-1}\text{nm}$  and  $D = 0$  (Kavhita *et al.* 2003). For bundled SWCNTs  $C = 232 \text{ cm}^{-1}\text{nm}$  and  $D = 6.5 \text{ cm}^{-1}$  (Alvarez *et al.* 2000). The non-zero value of  $D$  in bundled SWCNTs accounts for the upshift in the RBM frequency due to the van der Waal's interactions between tubes in a bundle (Dresselhaus and Eklund 2000).

The frequencies of the RBMs are resonant with electronic transitions in the nanotubes. This means that for a given sample of bundled SWCNTs, RBM peak frequencies and intensities will be different for different excitation energies.

The line width of the RBM peak in isolated SWCNTs varies with nanotube diameter (Dresselhaus *et al.* 2002). As the diameter of a nanotube increases, the line width of the RBM also increases. Line width also depends on the laser excitation energy  $E_{laser}$ . At resonance, where  $E_{laser} = E_{ii}$ , the RBM line width is very sharp, but as  $E_{laser}$  moves away from the resonance energy  $E_{ii}$ , the line width broadens. For a sample of bundled nanotubes, a sharp line width indicates a narrow diameter dispersion at that excitation energy.

RBM line widths also depend on other factors such as temperature dependent effects, tube-tube interactions, deformations and defects, electronic structure and curvature (Jorio *et al.* 2002a).

### 3.6.2 Tangential Mode (G-Band)

The G-band normally occurs between  $1500$  and  $1600 \text{ cm}^{-1}$  in SWCNTs. It is derived from the Raman allowed optical mode  $E_{2g}$  of 2D graphite by the zone folding of the 2D graphene Brillouin zone into the nanotube 1D Brillouin zone. Due to curvature and confinement, the G-band in carbon nanotubes has two distinct peaks, the  $G^-$  peak, which has a lower frequency and the  $G^+$  peak, which has a higher frequency.



In semi-conducting SWCNTs the  $G^-$  peak is due to atomic vibrations along the nanotube circumference (TO mode) and the  $G^+$  peak is due to atomic vibrations parallel to nanotube axis (LO mode) (Fig 3.4). Both the  $G^-$  peak and  $G^+$  peak in semi-conducting SWCNTs can be fitted with Lorentzian lineshapes. In metallic SWCNTs the  $G^+$  peak also has a Lorentzian lineshape. However, the  $G^-$  peak in metallic SWCNTs is significantly broader than the  $G^+$  peak and has an asymmetric Breit-Wigner-Fano (BWF) lineshape. There are two contrasting models on the assignment of the mode vibrations responsible for each peak in metallic SWCNTs and on the origin of the asymmetric BWF lineshape.

The earlier model (Brown *et al.* 2001; Jiang *et al.* 2002; Uchida *et al.* 2004; Bose *et al.* 2005) suggests that the  $G^-$  peak in metallic SWCNTs is due to the TO mode, as in semi-conducting SWCNTs. This deduction is due to the fact that because of curvature, the atomic vibrations in the circumferential direction should be softer than those parallel to tube axis because of weakening of force constants in this direction. The  $G^-$  band frequency also shows a strong diameter dependence, hence its attribution to the TO mode which would be affected by curvature.

These authors attributed the broadening of the  $G^-$  peak in metallic SWCNTs to plasmon-phonon coupling. According to this theory the excitation of the low frequency optical plasmon corresponding to the tangential motion of electrons on the surface of the metallic nanotube and its interaction with the phonon associated with the tangential vibration of carbon atoms is responsible for the broadened  $G^-$  band of metallic SWCNTs. Jiang *et al.* (2002) supported this idea by showing that the BWF line intensity is higher for nanotubes in thick bundles compared to isolated nanotubes or nanotubes in thin bundles. They attributed this effect to a formation of a plasmon band due to the interaction of many metallic tubes within the bundle. They concluded that the coupling of this plasmon band to the Raman phonon gives rise to the BWF line shape for the  $G^-$  peak in metallic SWCNTs .

A study of the temperature dependence of the BWF line for bundled SWCNTs by Uchida *et al.* (2004) for the temperature range 3K-500K showed that the line

width and the intensity decrease with increasing temperature. This behaviour was explained in terms of the thermal expansion of the intertube distance in a bundle resulting in the restriction of the formation of the plasmon band which couples with the TO phonon to give the BWF lineshape. Our results of the temperature dependence of the BWF line width will be reported in Chapter 6.

However, recent models (Ishikama and Ando 2006; Lazzeri *et al.* 2006; Popov and Lambin 2006; Piscanec *et al.* 2007a) provide detailed theoretical models to support their conclusions that the  $G^-$  peak in metallic nanotubes is due to the LO mode, and not the TO mode as in semi-conducting SWCNTs.

Lazzeri *et al.* (2006) provide evidence that the  $G^-$  peak in metallic SWCNTs is due to coupling between phonons and electron-hole pairs, contrary to the earlier held theory of plasmon-phonon coupling (Brown *et al.* 2001; Jiang *et al.* 2002; Uchida *et al.* 2004; Bose *et al.* 2005). Using Density Functional Theory calculations they show that in metallic SWCNTs the LO mode, which is due to atomic vibrations along the nanotube axis is always lower in frequency compared to the TO mode, which is due to atomic vibrations in the circumferential direction. They show that the LO mode frequency in metallic SWCNTs is diameter dependent, in contrast to the earlier theory which suggests that the TO mode frequency of metallic SWCNTs should be diameter dependent.

The lowering of the LO mode frequency was attributed to the presence of Kohn anomalies in the phonon dispersion of metallic SWCNTs. In general, a Kohn anomaly refers to the anomalous behaviour in the phonon dispersion pattern of metals due to the screening of atomic vibrations by electrons (Kohn 1959; Piscanec *et al.* 2004). In metallic SWCNTs, the strong coupling of two electrons with wavevectors  $k_1$  and  $k_2$  having length  $k_F$  at the Fermi surface by a phonon of wavevector  $q = k_1 - k_2$  leads to anomalous softening of the LO phonon branch (Popov and Lambin, 2006).

Since electron-phonon coupling (EPC) is large for the LO phonon and zero for the TO phonon, the presence of a Kohn anomaly only results in the lowering of

the frequencies of phonon modes showing significant EPC. This results in the LO mode frequency being lower than the TO mode frequency. As a result, Lazzeri *et al.* (2006) have assigned the lower frequency  $G^-$  peak in metallic SWCNTs to the LO mode and the higher frequency  $G^+$  peak to the TO mode.

Lazzeri *et al.* (2006) also calculated  $\gamma^{EP}$ , the electron-phonon interaction contribution to the linewidth of the Raman peaks corresponding to the LO and TO modes. They found that for the LO mode in metallic SWCNTs,  $\gamma^{EP}$  has a relatively high value, whilst for the TO mode  $\gamma^{EP}$  is zero. Since for metallic SWCNTs the full width at half maximum (FWHM) of the  $G^-$  band can be up to six times greater than the FWHM for the  $G^+$  band (Jorio *et al.* (2002)), this is consistent with the assignment of Lazzeri *et al.* (2006), namely that the LO mode corresponds to the broad  $G^-$  band while the TO mode is responsible for the narrow  $G^+$  band. The result provides strong evidence in favour of the dominant interaction resulting in the broad  $G^-$  band being electron-phonon in nature rather than plasmon-phonon.

Piscanec *et al.* (2007a) also assign the  $G^-$  Raman peak of metallic SWCNTs to the LO mode. However, for semi-conducting SWNTs, they assign the  $G^-$  peak to the TO mode and the  $G^+$  peak to the LO mode, opposite to that for metallic tubes. They argue that this difference in mode assignment between metallic and semi-conducting tubes is due to the differences in LO frequencies of metallic and semi-conducting tubes, which is a result of the presence of Kohn anomalies in the phonon dispersion of metallic nanotubes.

Other authors have used variants in their theoretical approaches to show that the LO mode frequency in metallic nanotubes is lower than the TO mode frequency, and should therefore be assigned to the  $G^-$  peak. Popov and Lambin (2006) used the symmetry adapted non-orthogonal tight binding model to show that the electron-LO phonon interaction in metallic nanotubes leads to a Kohn anomaly in the phonon dispersion which results in a softening of the LO frequency to below that of the TO mode. Ishikama and Ando (2006) used the effective-mass approximation model to show that there is significant lowering of the LO mode frequency in metallic

SWCNTs and that the TO modes in metallic and semi-conducting nanotubes are different in that the TO mode frequency of semi-conducting tubes shows a diameter dependence whilst that for metallic tubes does not.

It is noted that the shape, frequency and width of the G-band can be used for (i) distinguishing between metallic and semi-conducting tubes (Brown *et al.* 2001) (ii) analysing charge transfer during doping processes (Corio *et al.* 2003) (iii) diameter characterization (Jorio *et al.* 2002b; Lazzeri *et al.* 2006) and (iv) determination of sample temperature during heating processes (Huong *et al.* 1995).

### Distinguishing Between Metallic and Semi-conducting SWCNTs

Despite contrasting theories on the origins and mode assignment for the G<sup>-</sup> band of metallic SWCNTs, it is generally agreed that the broader G<sup>-</sup> shape from the Raman spectra of SWCNTs is a signature of metallic SWCNTs. The G<sup>-</sup> feature in semi-conducting tubes is narrow and can be fitted with a Lorentzian lineshape. The G<sup>-</sup> peak of metallic SWCNTs may be fitted with a Breit-Wigner-Fano line shape. The asymmetric Breit-Wigner-Fano line shape is expressed as

$$I(\omega) = I_0 \frac{[1 + (\omega - \omega_{BWF})/q\Gamma]^2}{1 + [(\omega - \omega_{BWF})/\Gamma]^2} \quad (3.12)$$

where  $\omega_{BWF}$  is the BWF peak frequency at maximum intensity  $I_0$ .  $1/q$  is a measure of the interaction of a phonon with a continuum of states and  $\Gamma$  is the full width at half maximum (FWHM) of the peak.

Figures 3.5 (a) and (b) show the G-band of semi-conducting and metallic SWCNTs clearly showing the different shapes of the G<sup>-</sup> bands in each case.

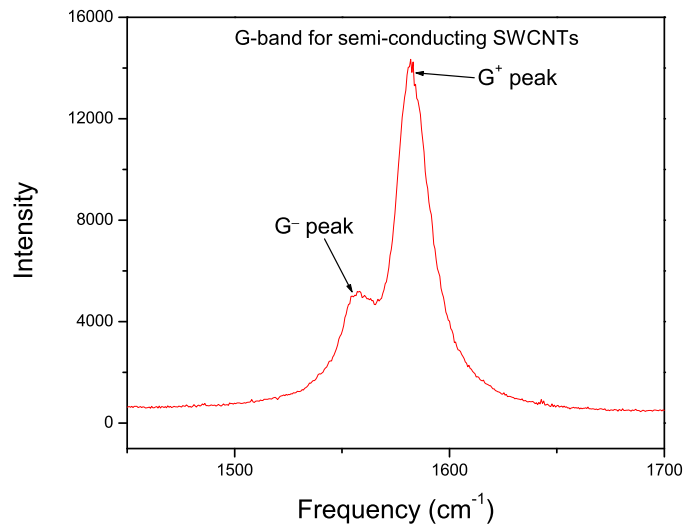


**Figure 3.5a:** The G-band of semi-conducting SWCNTs. Both the  $G^-$  and  $G^+$  have Lorentzian lineshapes.

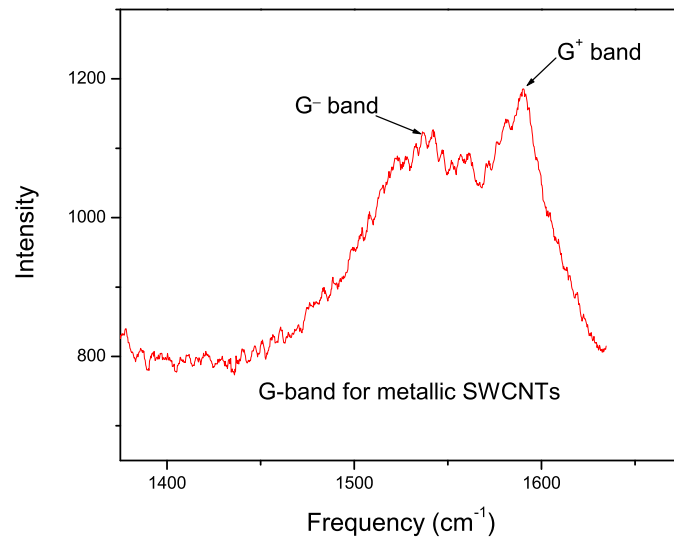


**Figure 3.5b:** The G-band of metallic SWCNTs. The  $G^+$  band has a Lorentzian lineshape, while the  $G^-$  band is much broader and can be fitted with a BWF lineshape.

### Diameter Dependence of the $G^-$ band Frequency

Experiments on SWCNTs by Brown *et al.* (2001) have shown a diameter dependence of the  $\omega_G^-$  peak, while the  $\omega_G^+$  is largely independent of nanotube diameter for both metallic and semi-conducting SWCNTs.  $\omega_G^-$  decreases as nanotube diameter ( $d_t$ ) decreases. Jorio *et al.* (2002b) used the splitting of the  $\omega_G^-$  and  $\omega_G^+$  peaks for diameter characterization using the equation

$$\omega_G^+ - \omega_G^- = \frac{\gamma}{d_t^2} \quad (3.13)$$

where  $\gamma = 47.7 \text{ cm}^{-1} \text{ nm}^2$  for semi-conducting tubes and  $\gamma = 79.5 \text{ cm}^{-1} \text{ nm}^2$  for metallic tubes at room temperature. In these cases they assigned the  $G^-$  mode to the tangential vibrations (TO phonon) and the  $G^+$  mode to the longitudinal vibration (LO phonon) for both metallic and semi-conducting SWCNTs.

However, Lazzeri *et al.* (2006) calculate that the LO mode frequency, which they assign to the  $G^-$  band in metallic SWCNTs is diameter dependent according to their model as discussed above while the TO mode frequency is diameter independent and can be expressed by the equations

$$\omega_{LO}^2 = A^2 - \frac{B}{d}; \quad \omega_{TO}^2 = C \quad (3.14)$$

where A, B and C are constants. It is appreciated that these results do not take into account the reduction in mode frequency with increasing temperatures resulting from anharmonic effects.

### Studying the Thermal Properties of SWCNTs

The G-band and the RBM peak positions and intensity can be used for sample characterization at different temperatures. It has been shown that G-band and RBM peak positions decrease in frequency with increasing sample temperatures (Li *et al.* 2000; Raravikar *et al.* 2002; Zhang *et al.* 2006). This decrease can be attributed to, among other things, lengthening of the C-C bond with temperature, thermal expansion of the tubes in the radial direction and softening of the van der Waal interactions in a bundle.

For a non-resonant scattering process, it is possible to use Raman peak intensities to determine sample temperatures using the Stokes to anti-Stokes intensity ratios (Kuzmany 1998),

$$\frac{I_{as}}{I_s} = \left( \frac{\nu_i + \nu_s}{\nu_i - \nu_s} \right)^4 \exp\left(\frac{-h\nu_s}{k_B T}\right) \quad (3.15)$$

where  $\nu_i$  is the frequency of the incident radiation and  $\nu_s$  is the frequency of the scattered light. The Boltzmann exponential term is the dominant term in the above equation, and this makes the anti-Stokes feature much smaller than the Stokes term.

To obtain an enhancement of the anti-Stokes spectra, Raman measurements can be done by placing the sample on a metallic surface whose roughness is of nanometer dimensions using the surface enhanced Raman scattering (SERS) effect (Smith and Rodger 2002). The enhancement of the Stokes and anti-Stokes peaks in SERS is primarily due to the electric field enhancement associated with localized surface plasmon resonance that occurs at optical frequencies in small metal particles. Significant transfer of the ground state population to the first excited vibrational state by spontaneous surface enhanced Raman scattering can also occur, resulting in an increase in the intensity of the anti-Stokes signal, an effect called vibrational pumping (Kneipp *et al.* 1996). The effects of this vibrational pumping are an anti-Stokes/Stokes ratio which is higher than that expected from a Boltzmann distribution and a quadratic dependence of the anti-Stokes Raman intensity on the excitation intensity. According to the vibrational pumping rate equation model by Kneipp *et al.* 1996, the intensities of the Stokes and anti-Stokes peaks are given by

$$I_S = Nn\sigma \quad (3.16)$$

and

$$I_{AS} = \left[ \exp\left(\frac{-h\nu}{k_B T}\right) + n\sigma\tau \right] Nn\sigma \quad (3.17)$$

where  $n$  is the incident photon flux density,  $\sigma$  is the SERS cross section,  $N$  is the number of carbon nanotubes in the vibrational ground state in the scattering volume and  $\tau$  is the lifetime of the first vibrational excited state.

Figure 3.6 shows the variation of the G-band Stokes and anti-Stokes intensities as a function of the incident photon flux when vibrational pumping occurs. The Stokes intensity is linear with the excitation intensity while the anti-Stokes intensity shows a quadratic dependence on the excitation intensity.

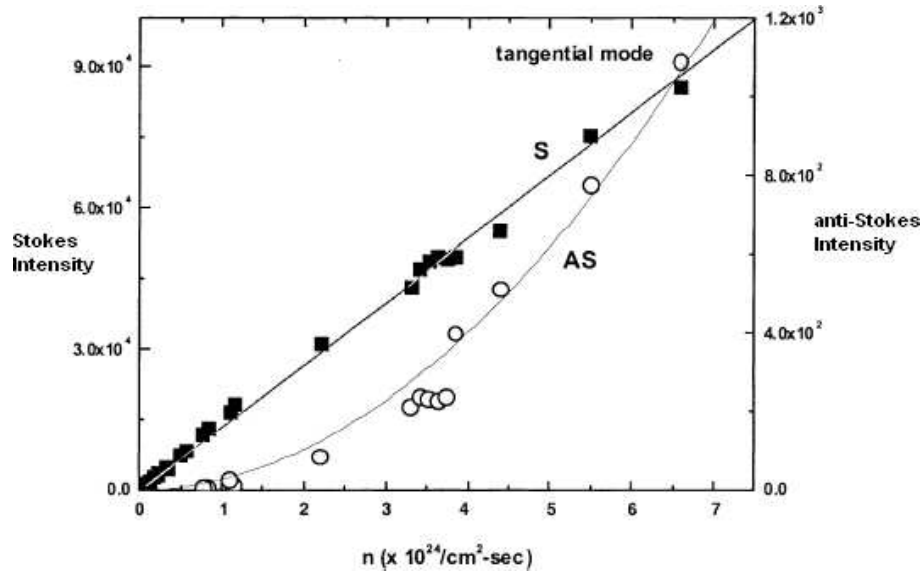


**Figure 3.6:** Variation of the G-band Stokes and anti-Stokes intensities as a function of the incident photon flux. (After Teredesai *et al.* 2001)

### 3.6.3 Disorder Induced Mode (D-band)

This mode carries information about the crystalline quality of the sample. It is a result of disorder such as in-plane hetero-atoms, vacancies, grain boundaries and other effects which lower the crystallinity of the sample. In carbon nanotubes it is also due to the presence of high quantities of amorphous carbon or when the energy of the incident phonon is far from  $E_{ii}$  (Jorio *et al.* 2003).

The line width and intensity of the D-band ( see Figure 3.4) is used to measure the degree of disorder in SWCNTs. A small D-band intensity compared to the G-band intensity indicates a good level of purity and few structural defects of the SWCNTs.

The frequency of the D band,  $\omega_D$  has a linear dependence on the excitation laser



energy  $E_{laser}$  (Matthews *et al.* 1999; Maultzsch *et al.* 2001). This effect is due to a double resonance Raman process, which selects a phonon wave vector for a given excitation energy. Due to the dispersive nature of the phonon band, change in wave vector satisfying the double resonance condition results in a shift in phonon energy.

$\omega_D$  also depends on the diameter of the nanotubes (Pimenta *et al.* 2001). As tube diameter decreases  $\omega_D$  also decreases. Pimenta *et al.* (2001) also showed that for SWNT bundles, the D band intensity is larger for metallic SWCNTs than for semi-conducting SWCNTs.

# Chapter 4

## Raman Experimental Arrangement

### 4.1 Introduction

Although the theory of Raman scattering has been known for a long time, the use of Raman scattering on a large scale to study materials gained momentum only in the nineteen sixties. This is because the Raman effect is very weak, only one in  $10^8$  photons being Raman scattered (Kagel 1991). This meant that very intense incident radiation and very sensitive measuring equipment had to be used. These challenges have been overcome because of the commercial availability of lasers, and the production of very sensitive spectrometers (Adar 2001). These developments have made Raman spectroscopy one of the most important and most reliable methods of studying and characterizing materials.

### 4.2 Experimental Apparatus

#### 4.2.1 The Laser

A laser is a source of intense, coherent monochromatic radiation. Two different types of lasers, the argon ion-laser and the krypton-ion laser were used in this work.

These fall in the group of noble gas lasers, where laser light is produced by the amplification of the radiative electronic transitions of the ionised states of noble gas atoms (Hecht 1999).

The gas is contained in sealed cylinder, called a plasma tube, at a low pressure. An intense electric discharge between two electrodes is used to produce a plasma, consisting of ionised gas particles and electrons. The electrons collide with neutral gas particles, causing them to ionise and become highly excited.

In the case of the  $\text{Ar}^+$  laser used as an example, the first collision with an electron ionises the argon, and the second collision pumps it to an excited state (Figure 4.1). The excited state has a very short lifetime, so the ion decays non radiatively to the  $4p$  energy level. The  $4p$  energy level has a relatively long lifetime, allowing a build up of ions in that level. This creates a condition called population inversion, where there are more ions in the higher energy levels than the ground state. Population inversion is a necessary condition for laser operation.

The  $4p$  ions then decay into the  $4s$  level, either spontaneously or by stimulation by a photon of equivalent energy. The transition is radiative and the emitted photon has a wavelength that can be expressed by the formula

$$\lambda = \frac{hc}{E}$$

where  $h$  is Planck's constant,  $c$  the speed of light and  $E$  the energy separation between the states.

The light energy released through stimulated emission in the plasma tube is stored in the optical cavity of the ion laser. Figure 4.2 shows a schematic diagram of the laser optical cavity. At one end is a high reflector mirror with a reflectivity of 100%, and at the other end is an output mirror with a reflectivity of slightly less than 100%. The emitted photons move back and forth between these mirrors and in the process they stimulate more atoms to produce photons. A small percentage of the photons manage to pass through the output mirror and these make up the output laser beam.

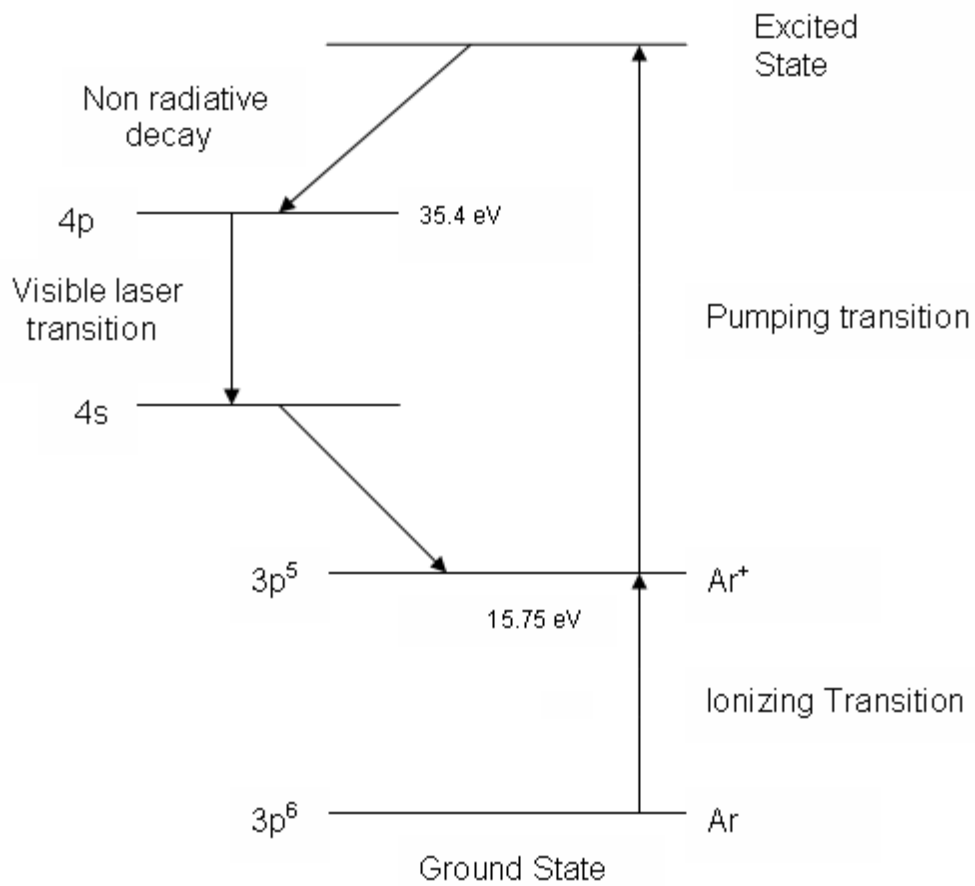


**Figure 4.1:** A transition scheme for an Ar<sup>+</sup> laser. The first collision ionises the neutral argon and the next pumps it to an excited state (from the Operational Manual for the Spectra Physics 2020/2025 Ion Laser.)

Resulting from the population inversion, photons emitted by the stimulated emission process are emitted coherently and greatly exceed those emitted spontaneously that are incoherent. The design of the long optical cavity ensures that the stimulated photons are emitted co-linear with the cavity axis, whereas the spontaneous photons are randomly emitted and hence the relatively few on-axis photons result in a very weak incoherent noise superimposed on the beam.

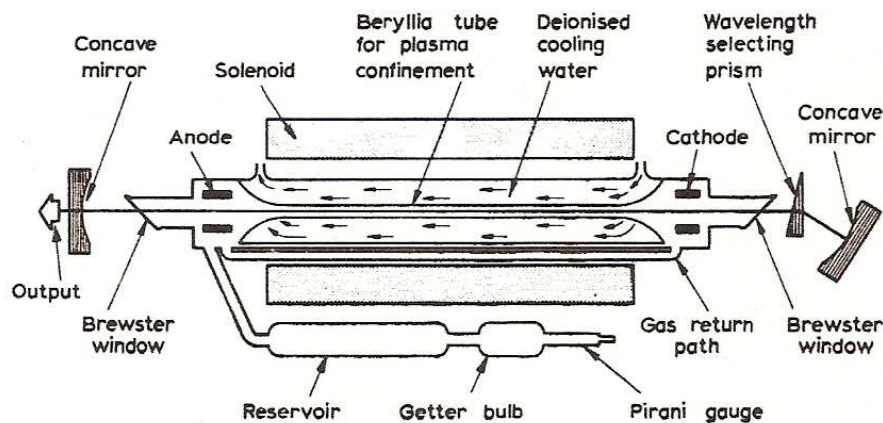


*Figure 4.2:* Schematic diagram of a gas laser (after Beesley (1976))

### 4.2.2 The Raman Spectrograph

Figure 4.3 shows a schematic diagram of the Jobin-Yvon T64000 Raman spectrograph used in our laboratory. Laser light is directed into the spectrometer by optical mirrors. The light can be focused on the sample using an Olympus BX40 microscope attached to the spectrograph. A narrow band pass filter removes the laser plasma lines and allows only the selected wavelength into the microscope.

Scattered light from the sample returns through the microscope into the spectrometer where it is processed in any one of the three configurations of the spectrograph.

In the single spectrograph mode, the light is directed to a holographic notch filter, which strongly suppresses the elastically scattered light but allows the Raman scattered light to pass through. The transmitted light then passes through an

entrance slit and falls on a grating where it is dispersed.

Two types of grating are available with the spectrometer and can be used interchangeably using the software. The choice of grating depends on the resolution and spectral range required. The 600g/mm grating offers a wide spectral range but resolution is reduced, whereas the 1800g/mm grating has a narrow spectral range but improved resolution.

Light dispersed by the grating falls on the charge coupled device (CCD) detector, which detects the scattered light and produces a spectrum. The CCD detector is a rectangular chip comprising of 1024 x 256 pixels, each pixel being a silicon photosensor. When scattered radiation falls on a pixel, photoelectrons are produced in numbers proportional to the intensity of the radiation. For optimum performance, the CCD is cooled to 140K by liquid nitrogen. The advantage of the single spectrograph mode is that it has a higher throughput and offers rapid analysis time. Its disadvantage is that it cannot be used for Raman bands close to the frequency of the laser line.

In triple subtractive mode, the two pre-monochromators work as filters by dispersing the scattered light and recombining part of it, before it is re-dispersed by the spectrograph. The advantage of the triple subtractive mode is that it is more efficient in removing stray light resulting from the laser exciting line therefore allowing for analysis at low wavenumbers. However, the throughput is considerably weaker than that obtained in the single spectrograph mode.

In triple additive mode, all three monochromators act as dispersers, and this results in a narrow range of wavelengths being spread across the detector, and therefore offering very high resolution of a small spectral range. Its disadvantage is that it is not possible to perform analysis close to the laser line.

The output from the detector is analysed on a computer using Labspec Scientific software supplied by Jobin-Yvon. The spectra can be saved in the form of data or text files which can be exported to a spreadsheet for analysis.

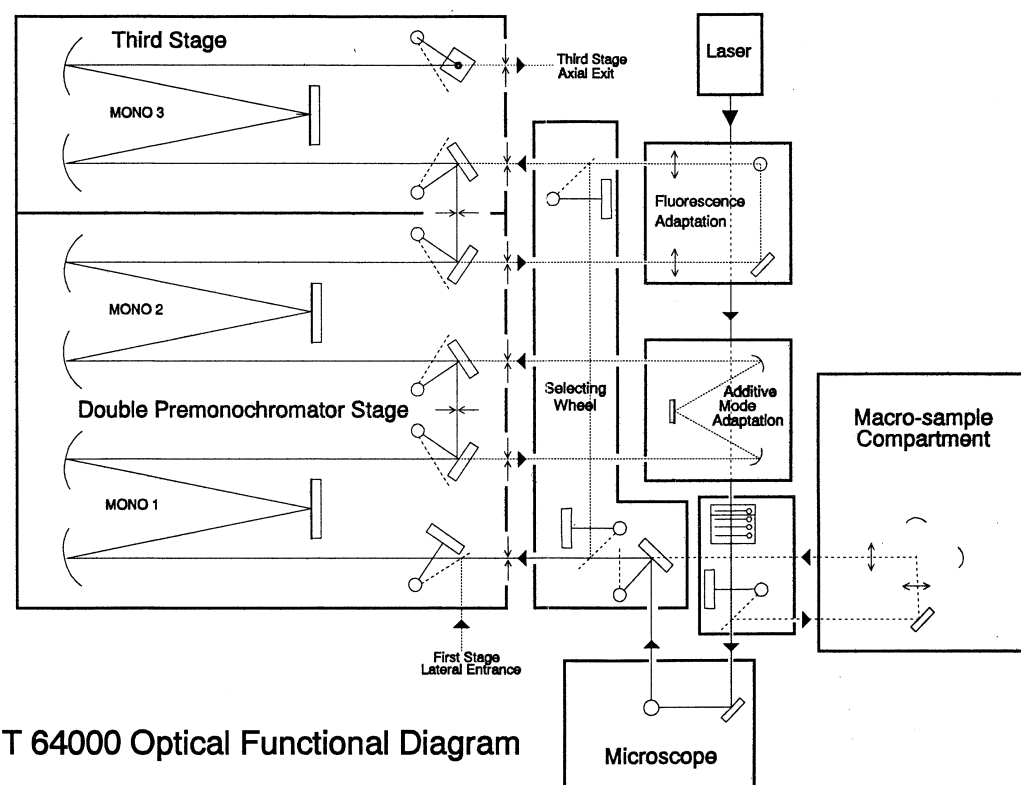


**Figure 4.3:** Schematic diagram of the Raman Spectrograph showing the beam path (from the Instruction Manual for the Jobin-Yvon T64000 Raman spectrograph).

## 4.3 Heating Stage

A Linkam TS1500 heating stage was used for high temperature Raman measurements of SWCNTs and is shown schematically in Figure 4.4. In this work the cell was used for measurements from room temperature to 1100K.

The body, lid and window of the cell are water cooled to protect the user and the lens from the high temperatures inside the stage. The sample is placed on a sapphire disc located in a deep ceramic sample cup. The stage is designed to attach to the Olympus BX40 microscope allowing for in-situ Raman measurements to be made at high temperatures. Heating of the sample takes place from underneath as well as from the sides of the cup.

Temperature is controlled by a TMS1500 programmer via an s-type platinum/rhodium thermocouple. The thermocouple is located directly below the sapphire disc and has an accuracy of  $\pm 1\text{K}$  in an Argon environment. At room temperature the thermocouple reading is  $\pm 1\text{K}$  of the ambient temperature. This means that the error on temperature in the range 298K to 1100K is less than 0.7%. The power supply from the programmer to the heating stage is DC to eliminate electromagnetic interference. There are two gas valves on the sides of the stage body so that the environment within the cell can be controlled.

### 4.3.1 High Temperature Experimental Procedure

The single walled carbon nanotubes in the form of small sample bucky paper (see Section 5.3.1) was placed on a sapphire disc inside the heating chamber of the the heating cell. The cell was mounted on the microscope stage of the Raman spectrometer. The laser beam was focused on the sample using the microscope with a  $20\times$  objective lens. A motorized X-Y stage was used to move the cell and an attached monitor located the beam positions on the sample. The diameter of the de-focused laser beam on the sample was kept at  $4.7 \times 10^{-3}\text{cm}$ . Laser powers were measured at the sample before and after the experiment.



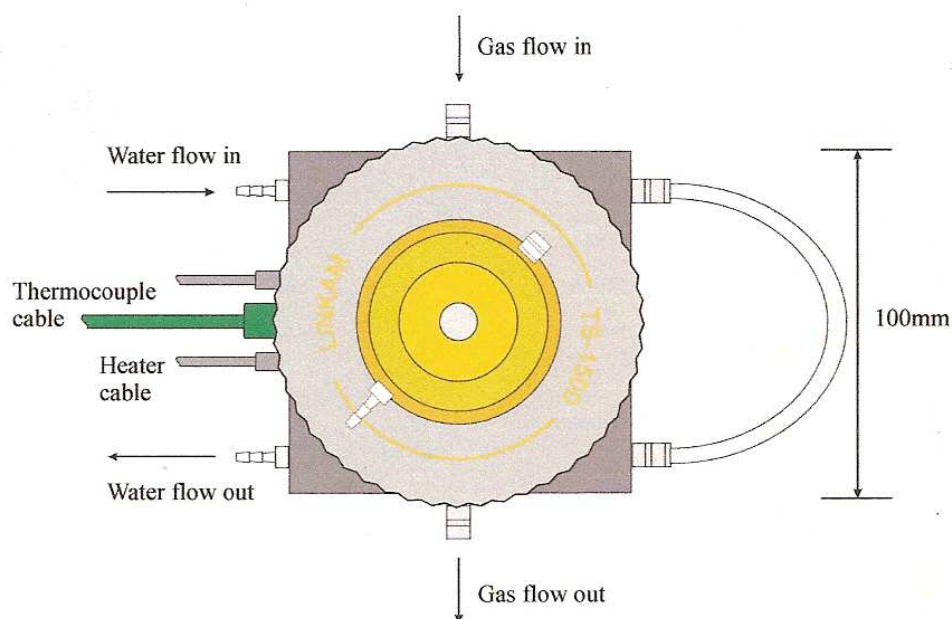


**Figure 4.4:** Schematic diagram of the Linkam heating stage (after Hayes 2002).

At the beginning of each session, alignment of the external optics was carried out. This was done by moving the laser beam steering mirrors in the X-Y direction until the laser beam on the monitor showed perfectly circular concentric rings. Calibration of the spectrometer was also carried out at the beginning of each session, especially after any changes in the setup, such as moving from single spectrograph mode to triple mode or after changing lasers. Laser plasma lines were used for calibration of the spectrograph. These plasma lines have well defined frequencies and have very narrow line widths. For the green line of the  $\text{Ar}^+$  laser, calibration was done using the plasma line which has a peak shift of  $520.30 \text{ cm}^{-1}$  from the Rayleigh scattered line. The mercury discharge lamp was also used employing the mercury peak which has a shift of  $1122 \text{ cm}^{-1}$  from the Rayleigh scattered line. It is noted that mercury lamp was switched on during acquisition of spectra and each spectral position taken with reference to the mercury peak. This reduces calibration errors and those due to spectrometer wavelength drift to negligible values.

The Linkam TS1500 heating cell was controlled by a Linkam TMS93 temperature

controller. The heating rate was kept at 20K per minute from room temperature to 1073K for semi-conducting tubes and to 873K for metallic nanotubes. Argon gas flow in the cell was maintained at a rate of 0.1 litres per minute. Argon provides an inert environment in the cell so as to prevent oxidation of the sample at high temperatures. Water for cooling the cell was pumped from an external reservoir by means of an electric pump and enters the cell where it circulates before it is pumped back to the reservoir. The sample within the cell was heated in intervals of 100K and stabilized at each temperature before recording a spectrum. This was done to achieve thermal equilibrium in the cell. Raman spectra were collected using the Jobin-Yvon Raman spectrograph in single or triple subtractive modes using entrance slit widths of 150  $\mu\text{m}$  and a 1800g/mm grating as discussed in Section 4.2.2. Spectra were collected for two heating and cooling cycles. This procedure helps to improve the stability of the sample by thermally de-activating the contributions to the spectrum of amorphous carbon and some unstable small diameter nanotubes.

The 514.5 nm and 488.0 nm laser lines from the argon-ion laser, corresponding to photon energies of 2.41 eV and 2.54 eV respectively were used to study semi-conducting nanotubes. This allows one to examine nanotubes that have the same electronic properties but different diameters. The 647.1 nm line of the krypton-ion laser, corresponding to a photon energy of 1.92 eV was used to excite the metallic nanotubes. Figure 3.3 shows the density of states and the energy transitions necessary for exciting metallic and semi-conducting SWCNTs.

The output from the CCD detector is displayed on the computer monitor in the form of a spectrum. The output is saved in text format and exported to a spreadsheet using Origin software. Peak fitting was performed using the non-linear peak fitting routine also using Origin software. The RBM, the  $G^+$  and  $G^-$  bands of semi-conducting SWCNTs were fitted with Lorentzian lineshapes. The  $G^+$  band of metallic SWCNTs was also fitted with a Lorentzian lineshape and the  $G^-$  band was fitted with a Breit-Wigner-Fano lineshape. Errors arising from the peak fitting procedure are very small (less than  $1\text{cm}^{-1}$ ) for the  $G^+$  and  $G^-$  band peak frequencies

and higher ( $\approx 1\text{cm}^{-1}$ ) for the line widths of these peaks. The errors due to peak fitting give the highest contributions to errors in frequencies.

## 4.4 The Cryostat

Low temperature Raman measurements on SWCNTs were carried out using a continuous flow Oxford Instruments microstatHE micro-cryostat system which is designed to be mounted on the Raman microscope. Figure 4.5 shows a schematic diagram of the experimental arrangement for the low temperature experiments. Using liquid nitrogen, the working temperature range of the cryostat is from 70K to 450K. During operation the environment inside the cryostat is kept under vacuum conditions using a Pfeiffer-Turbocube high vacuum turbo molecular pumping system.

An Oxford Instruments GF3 diaphragm pump with a gas flow controller was used to draw liquid nitrogen from the dewar along a transfer tube into the sample holder. A thermocouple and a heater are mounted on the sample holder inside the cryostat. The gas flow controller has a flow meter and a pressure gauge to control flow rates and pressure. Cooling of the sample occurs as the nitrogen evaporates on the sample holder inside the cryostat.

Sample temperature and temperature inside the cryostat is controlled by means of an Oxford Instruments ITC4 temperature controller. In this work, Raman spectra were measured from 77K to 400K.

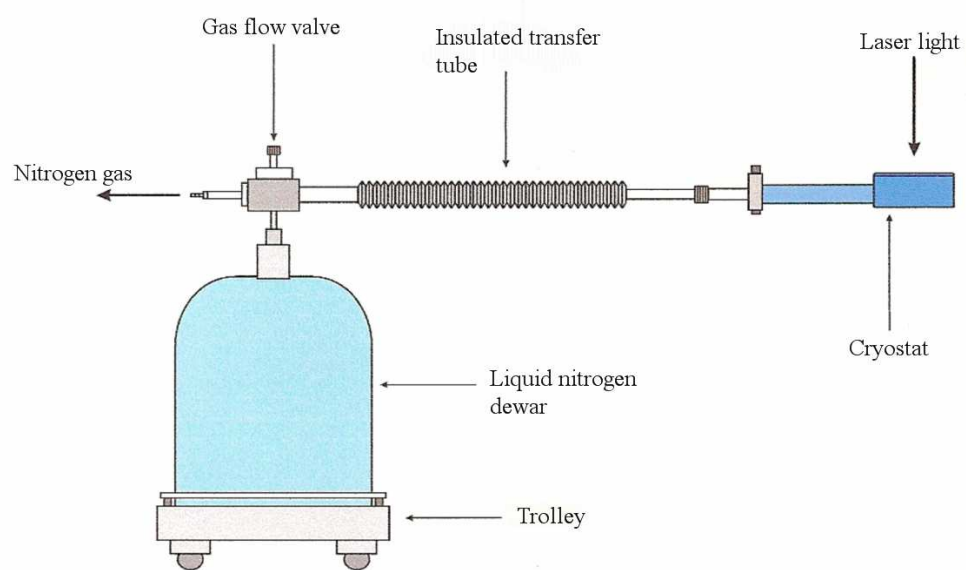


**Figure 4.5:** Schematic diagram of the cryostat system (after Hayes, 2002).

# Chapter 5

## Electric Arc Discharge Synthesis of SWCNTs

### 5.1 Introduction

In this chapter a description of the electric arc-discharge synthesis for SWCNTs using different catalysts is given. A comparison of their Raman spectra is then made to assess the quality of the SWCNTs.

The first carbon nanotubes to be produced were observed in the by-products in the synthesis of fullerenes using the electric arc discharge method (Iijima 1991). Since then this method has been optimized for the production of carbon nanotubes, and to date, it is one of the most widely used methods for nanotube synthesis.

The method involves the arc vaporization of a graphite electrode into a gas plasma at low pressures. The use of catalysts, preferably transition metal catalysts is necessary for the formation of SWCNTs. Without the catalysts the products of the EA discharge process are usually multi-walled carbon nanotubes and fullerenes.

The aim of these experiments was to find the best conditions of pressure, plasma gas, current and catalyst which give the best quality SWCNTs.

## 5.2 Experimental Procedures

### 5.2.1 The Discharge Chamber

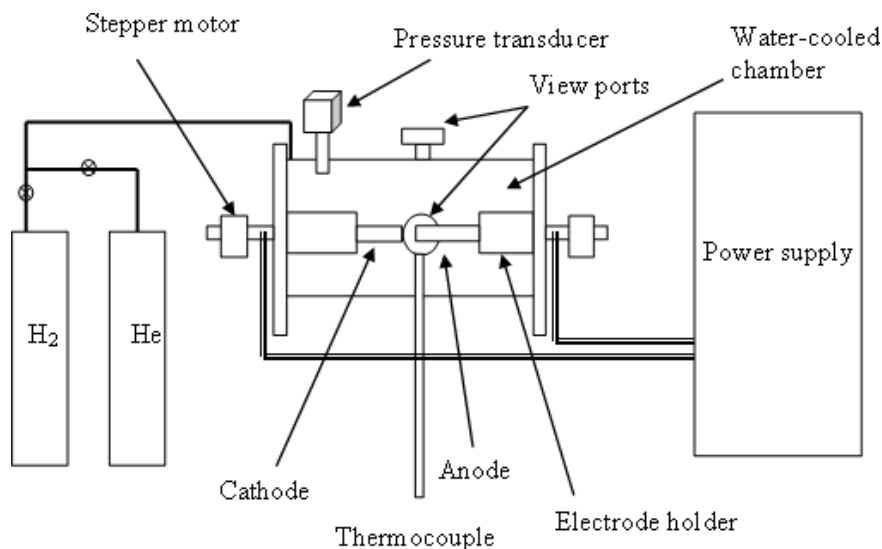


**Figure 5.1:** Schematic diagram of the electric arc discharge apparatus.

Figure 5.1 shows a schematic representation of the electric-arc (EA) discharge chamber used in this work. The chamber is located in the Chemistry Department at the University of Johannesburg, Doornfontein Campus. The electrodes are made of high purity graphite with an electrical conductivity of  $1120 \mu\Omega \text{ cm}^{-1}$  and a density of  $1.75 \text{ g/cm}^3$ . A hole about 5 cm deep is drilled in the anode and the catalyst material is loaded into this hole. The catalyst is made by mixing high purity graphite and a pure transition metal or a compound of transition metals. The pressure, current, potential and temperature parameters of the instrument are monitored and controlled by a Pentium 4 computer using Labview software. A thermocouple is fixed about 5 mm from the electrodes for temperature measurements. The chamber is water cooled to avoid over-heating of the outer jacket of the instrument.

### 5.2.2 Synthesis of Carbon Nanotubes

The arc chamber was first flushed four times with high purity helium gas and pumped down to a pressure of 20 kPa. A DC arc was then started with the current being 60 A, at a potential of 10V for about 3 minutes with helium at a pressure of 30 kPa or 60 kPa. These pressures were found to be the best suitable for a discharge chamber that was used in this case. As the anode is consumed into the gas plasma, the distance and potential between the two electrodes is maintained manually by means of a stepper motor on the chamber. After the arc-discharge process, the chamber is allowed to cool and is pumped back to ambient pressure. The produced soot is deposited on the cathode and walls of the discharge chamber. This procedure was repeated for four catalysts, A containing 25 at.% LaNi<sub>5</sub>, B containing 26 at.% LaNi<sub>5</sub>, C containing 2.7 at.% Fe, 2.9 at.% Co, 4 at.% FeS and 2.6 at.% Ni, and catalyst D containing 5 at.% YNi. Raman scattering measurements were done on the as-produced soot using the 514.5 nm excitation line of the argon ion laser.

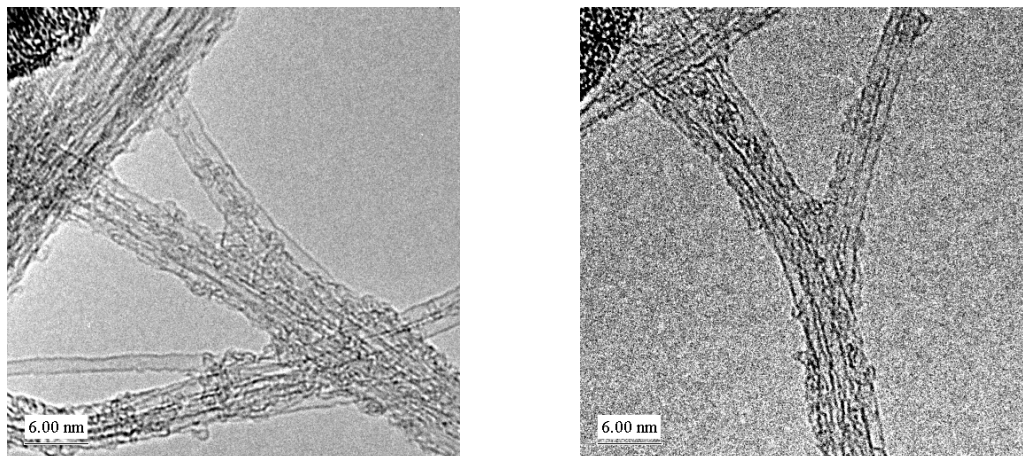
### 5.2.3 Transmission Electron Microscopy

Transmission electron microscopy (TEM) is an imaging technique that gives high resolution images up to the atomic scale. In the study of carbon nanotubes, TEM can be used to study the by-products of various synthesis methods, for example whether the products of a synthesis technique are single-walled carbon nanotubes, multi-walled carbon nanotubes or fullerenes and to calculate the diameters of these tubes or fullerenes. TEM images can also be used to make comparisons of the purity of nanotubes produced using different techniques or under different conditions.

In TEM, a stream of electrons is generated by a suitable source and accelerated towards the sample. The electrons are focussed by electro-magnetic lenses into typically a roughly parallel beam. When the beam strikes the sample, some of the electrons are backscattered, some are forward scattered, and for carbon nanotubes most travel through the sample without any interaction. The latter two types of electrons are utilized to form a magnified image of the sample on either a phosphor

screen or a CCD camera.

In the present case, the as-produced SWCNTs were ultrasonicated in absolute ethanol and then pipetted onto lacey, carbon-coated copper grids for TEM examination. Transmission Electron Microscopy studies were carried out at an accelerating voltage of 197 kV using a Philips CM200 instrument equipped with a LaB<sub>6</sub> source. A Gatan Model 678 Imaging Filter (GIF) was used to record the images.



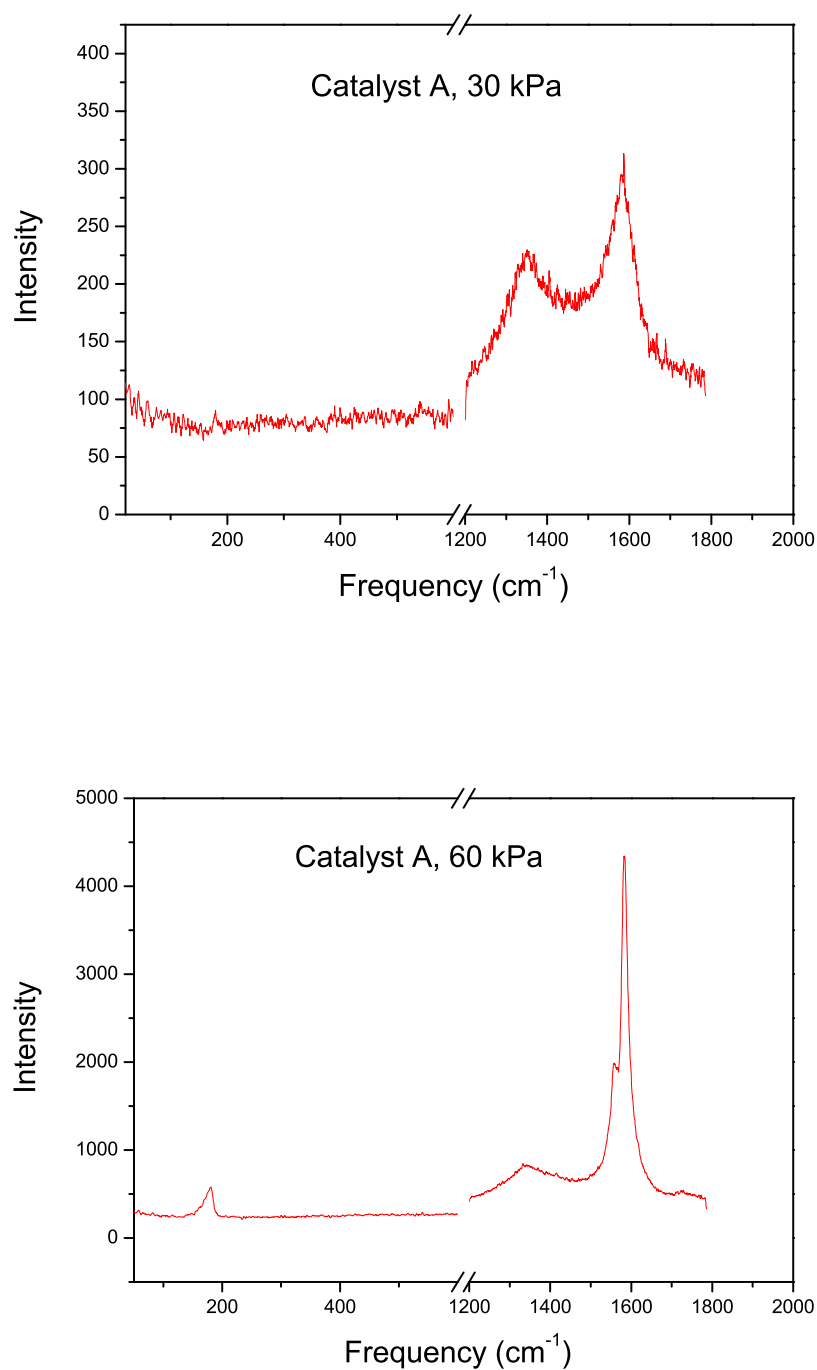
**Figure 5.2:** Transmission electron microscopy images of the as-produced soot using a 26 at.% LaNi<sub>5</sub> catalyst at a helium pressure of 60 kPa clearly showing bundles of SWCNTs.

Figure 5.2 clearly shows TEM images of SWCNT bundles on different regions of the as-produced SWCNT material from the arc-discharge process using a 26 at. % LaNi<sub>5</sub> catalyst and helium as a buffer gas at 60 kPa. The diameters of these tubes measured from the images above range from 0.96 nm - 1.68 nm. The images show that there is a low concentration of amorphous carbon impurities.

#### 5.2.4 Raman Spectroscopy

Raman scattering was carried out using the 514.5 nm excitation laser line, corresponding to a photon energy of 2.41eV. This laser line predominantly excites semi-conducting SWCNTs. The Raman spectra obtained from the soot produced under different conditions and using the four catalysts are shown in figures 5.3-5.5.





**Figure 5.3:** Raman spectra showing the RBM, the D-band and the G-band of the as-produced soot containing SWCNTs produced with catalyst A consisting of 25 at.% LaNi<sub>5</sub> at helium pressures of 30kPa (top) and 60kPa (bottom).

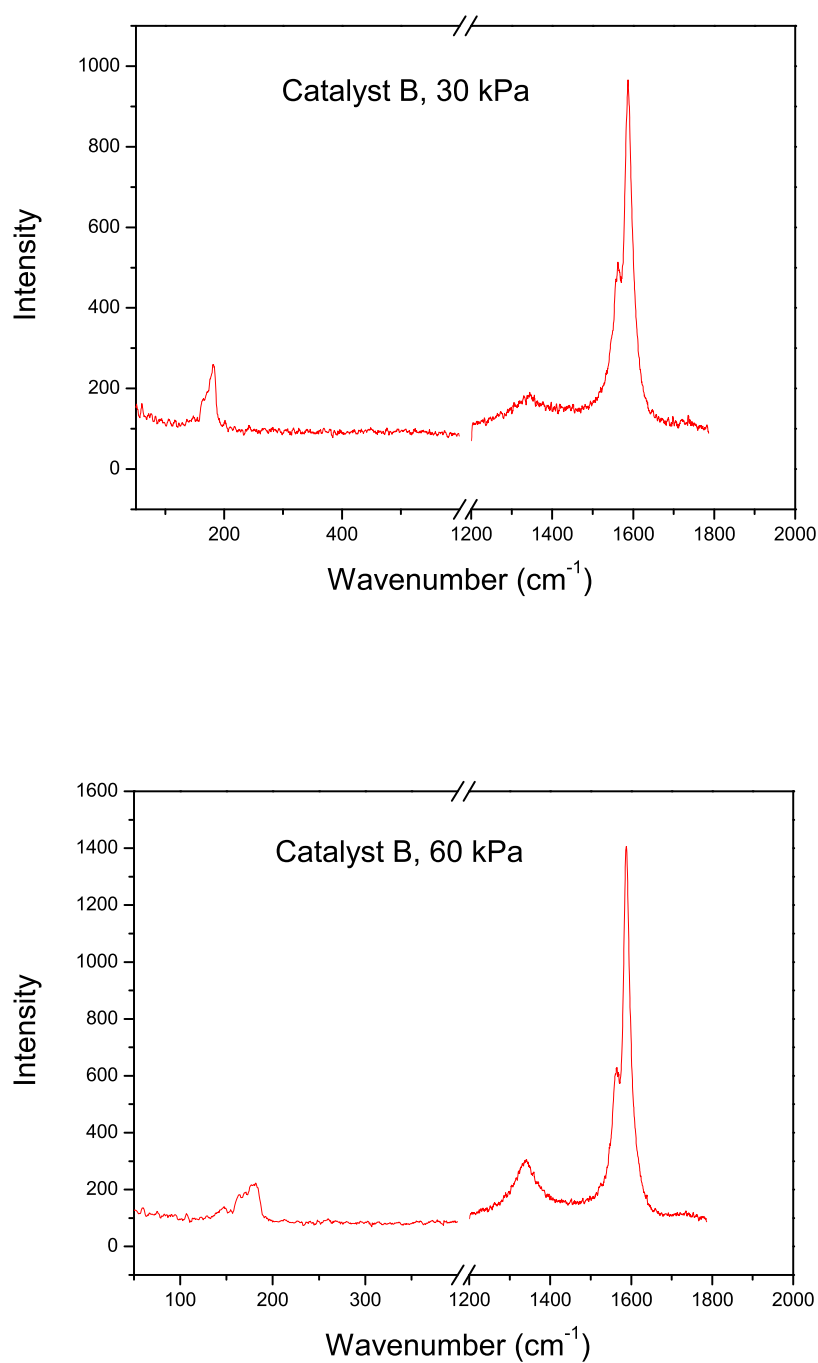


**Figure 5.4:** Raman spectra showing the RBM, the D-band and the G-band of the as-produced soot containing SWCNTs produced with catalyst B consisting of 26 at.% LaNi<sub>5</sub> at helium pressures of 30kPa (top) and 60kPa (bottom).

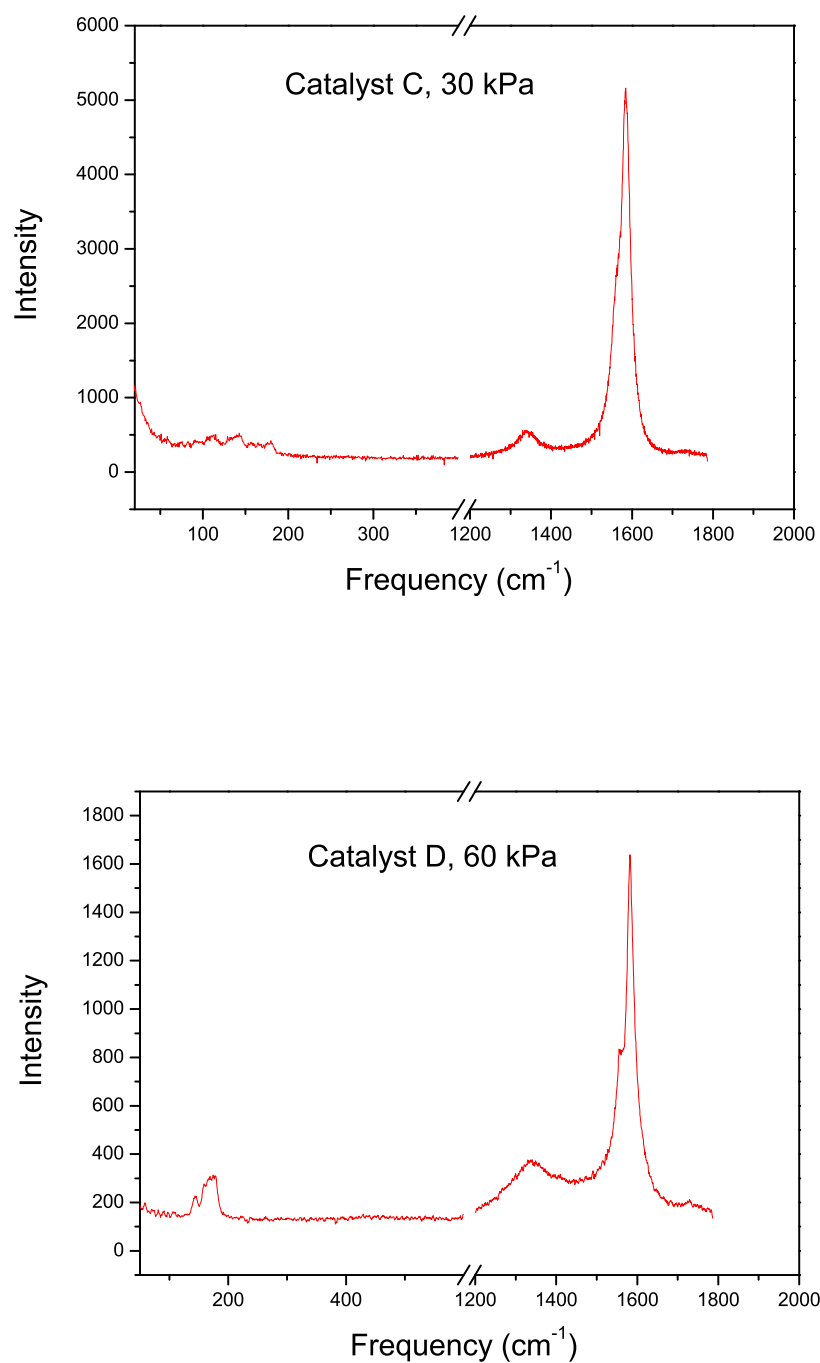


**Figure 5.5:** Raman spectra showing the RBM, the D-band and the G-band of the as-produced soot containing SWCNTs produced with catalyst C consisting of 2.7 at.% Fe, 2.9 at.% Co, 4 at.% FeS and 2.6 at.% Ni at a helium pressures of 30kPa (top) and catalyst D consisting of 5 at.% YNi at a helium pressure of 60kPa (bottom).

From the Raman spectra shown above, the intensity ratios of the G<sup>+</sup> band to the disorder induced D-band were determined. This ratio  $\left(\frac{I_G}{I_D}\right)$  was used to determine the purity and crystalline quality of the nanotubes. The higher the intensity of the D-band the more defects and impurities in that sample; therefore a high value of  $\left(\frac{I_G}{I_D}\right)$  is desirable. Table 5.1 lists the values of  $\left(\frac{I_G}{I_D}\right)$  for each of the catalysts used. The as-produced soot obtained using Catalyst C at a helium pressure of 60 kPa and catalyst D at a helium pressure of 30 kPa does not give good Raman signals, therefore are not listed in Table 5.1.

**Table 5.1:** Determination of SWCNT's purity using intensity ratios.

Catalyst	Helium Pressure (kPa)	$\left(\frac{I_G}{I_D}\right)$
A	30	1.53
A	60	9.90
B	30	11.77
B	60	7.28
C	30	8.52
D	60	5.75

From Table 5.1, the 26 at.% LaNi<sub>5</sub> catalyst at a helium pressure of 30 kPa gives the purest nanotubes corresponding to  $\left(\frac{I_G}{I_D}\right) = 11.77$  followed by the 25 at.% LaNi<sub>5</sub> catalyst at a helium pressure 60 kPa corresponding to  $\left(\frac{I_G}{I_D}\right) = 9.90$ . For the purposes of future experiments it was decided to use nanotubes grown with 25 at.% LaNi<sub>5</sub> under helium at 60kPa. Although they have a lower  $\left(\frac{I_G}{I_D}\right)$  ratio of 9.90 compared to those made with 26 at.% LaNi<sub>5</sub> at a helium pressure of 30 kPa, with an  $\left(\frac{I_G}{I_D}\right)$  ratio of 11.77, they have a narrower linewidth of the radial breathing mode indicating a narrower diameter distribution. This is an advantage when calculating diameters using the RBM frequency.

The determination of diameters of the semi-conducting and metallic SWCNTs, and the chirality assignment will be discussed in Chapter 6.

## 5.3 Purification of SWCNTs

The as-produced soot containing SWCNTs from the arc-discharge chamber contains impurities in the form of amorphous carbon and metal particles from the catalysts. The purity of these SWCNTs can be improved by carrying out purification processes to reduce the amounts of amorphous carbon and metallic catalyst particles.

### 5.3.1 Purification by Acid Mixture

The SWCNT soot produced using 25 at.% LaNi<sub>5</sub> catalyst at a helium pressure of 60kPa was purified using an HNO<sub>3</sub>/HCl acid mixture method (Chattopadhyay *et al.* 2002). 50 mg of the as-produced nanotubes were ultrasonicated for 5 hours in a 1:1 acid mixture of 98% HNO<sub>3</sub> and 35% HCl. The ultrasonication was done in order to break up the nanotube bundles so as to release metal particles trapped in between the bundles. The resulting dispersion was filtered using a high vacuum filtration system over a teflon micro-membrane filter paper. The filtrate was rinsed thoroughly with a mixture of distilled water and sodium hydroxide of pH 12. This helps in the solubilization of carbonaceous materials present in the soot. This was followed by washing with ethanol.

The SWCNT material left on the membrane filter was peeled off and was in the form of flakes, called bucky paper. The bucky paper was then vacuum dried at 373K for 8 hours. The SWCNT bucky paper is easier to handle and work with compared to the powdered form of SWCNTs.

This method is effective in removing the metal impurities that come from the catalyst as well as to reduce the amount of amorphous carbon. The presence of metallic impurities in the SWCNTs reduces the thermal conductivity of the sample (Li *et al.* 2000) because these particles do not dissipate heat effectively. This means that when a nanotube sample with a high concentration of metal particles is heated up, the metal particles then absorb heat, resulting in hot spots on the sample area. This results in an uneven temperature distribution in the sample.

Raman measurements on the as-produced SWCNTs could not be taken for temperatures exceeding 773K due to the increase in thermal background radiation partly resulting from the presence of metallic impurities. After purification Raman spectra could be measured for temperatures up to 1073 for semi-conducting tubes and 873K for metallic SWCNTs, indicating improved quality of the SWCNTs sample.

### 5.3.2 Purification of SWCNTs by Heating

Heating a sample of bundled nanotubes by a laser or by a heating cell purifies them and improves the structural stability of the sample. Figure 5.6 shows the room temperature Raman spectra of the same nanotube sample taken on the same spot using the same laser power density before and after the heating the sample to 1073K as described in section 6.2. The after heating spectrum is more intense indicating improved scattering efficiency and improved sample quality. The  $\left(\frac{I_G}{I_D}\right)$  ratio for the sample before heating is 5.06 and it increases to 14.2 after heating. This shows the importance of taking the sample through several annealing cycles before taking final measurements in temperature dependence experiments.

It is also noted from the successive heating and cooling cycles to be presented in figures 6.2, 6.5 and 6.8 to follow that in the earlier cycles there are irregular variations in the spectral properties. It is considered that these arise from the effects of thermally unstable nanotubes, effects of sample inhomogeneity resulting from the presence of amorphous carbon and other defects which are subsequently minimized with the technique of repeated heating and cooling cycles.

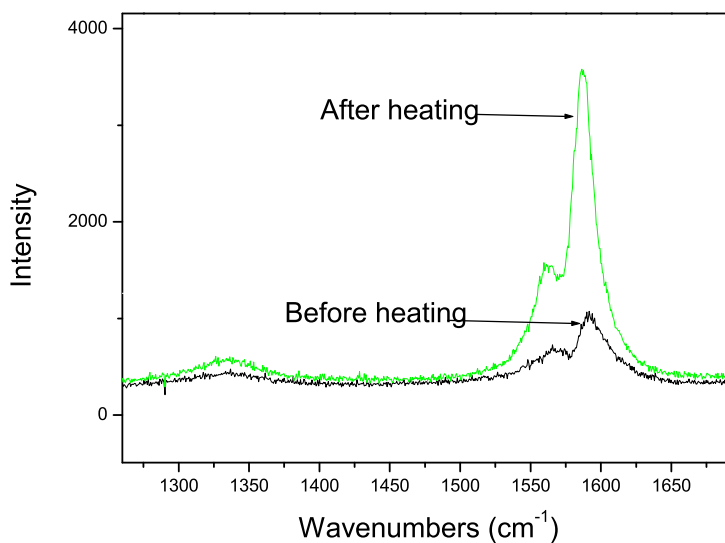


**Figure 5.6:** Room temperature Raman spectra taken on the same spot of a sample of SWCNTs using the 514.5 nm laser excitation before and after heating.

## 5.4 Discussion

SWCNTs of very high quality were successfully synthesized using the electric arc-discharge method. Different catalysts at different helium gas pressures were used during the EA discharge method. A comparison of the purity and crystalline quality of the as-produced soot containing SWCNTs was done by comparing their  $\left(\frac{I_G}{I_D}\right)$  ratios.

It was found that the 26 at.% LaNi<sub>5</sub> catalyst and helium buffer gas at a pressure of 30kPa gives SWCNTs of highest quality, with an  $\left(\frac{I_G}{I_D}\right)$  ratio of 11.77, followed by 25 at.% LaNi<sub>5</sub> and a helium pressure of 60kPa with an  $\left(\frac{I_G}{I_D}\right)$  ratio of 9.90. However, owing to the narrower diameter distribution found in the latter case, these were chosen for experimental investigations.

TEM studies were also carried out and they show the presence of SWCNTs in the as-produced soot, clearly indicating their bundled nature. The diameters of the SWCNTs measured from the TEM images range from 0.96 nm - 1.68 nm.

# Chapter 6

## Raman Studies of SWCNTs as a Function of Temperature

### 6.1 Introduction

This chapter presents the Raman scattering results on SWCNTs carried out as a function of temperature. The temperature dependence of the tangential and radial breathing modes of SWCNTs were studied in both a lower temperature region (77K-350K) and a higher temperature region (300K-1100K). Semi-conducting and metallic tubes were studied by taking advantage of the resonance effect of the 514.5 nm (2.41 eV) and 488.0 nm (2.54eV) argon laser lines for semi-conducting tubes and the 647.1 nm (1.92eV) Kr laser line which excites predominantly metallic nanotubes.

A very important aspect of this experiment was the laser power density (LPD) used on the samples. The LPD was maintained at less than 60 W/cm<sup>2</sup> for all samples studied in terms of the temperature dependence of the tangential and radial breathing modes to minimize laser heating effects. This ensures that any observed spectral changes are overwhelmingly due to the controlled heating from the heating stage. In much of the previous work of this kind, higher laser power densities have been used. Li *et al.* 2000 used a LPD in the range 10<sup>2</sup>-10<sup>4</sup> W/cm<sup>2</sup> in their



work. Teredesai *et al.* 2001 used a laser power density in the range  $10^4$ - $10^6$  W/cm<sup>2</sup>. Raravikar *et al.* 2002 used a LPD of  $3 \times 10^5$  W/cm<sup>2</sup> in their studies. Zhang *et al.* 2006 used a low LPD of 20 W/cm<sup>2</sup> for their work, but only achieved a maximum sample temperature of 673K. The maximum temperature attained in this work was 1073K for semi-conducting SWCNTs and 873K for metallic SWCNTs, these limiting temperatures being determined by the presence of substantial thermal background radiation and spectral broadening. The high and low temperature results are presented separately since the experiments were done in different environments.

A laser power dependence study of the G-band of semi-conducting tubes was also carried out. Here considerably higher laser powers on the sample were used and the effects of using high LPDs on the samples discussed.

## 6.2 Sample Preparation

The SWCNTs used were produced using the arc-discharge method, using 25 at.% LaNi<sub>5</sub> as a catalyst and helium as a buffer gas at a pressure of 60 kPa as described in Chapter 5. The as-produced SWCNT soot contained impurities in the form of amorphous carbon and metal particles from the catalyst. The SWCNT soot was purified using the method outlined in Section 5.3.1.

The bucky paper produced as described in Section 5.3.1 was taken through a series of heating and cooling cycles in order to remove the thermally unstable SWCNTs. This was done until the mode frequency versus temperature graphs show consistent behaviour. Heating the SWCNTs also purifies the SWCNTs as described in section 5.3.2. In this case it was found out that two heating and cooling cycles are sufficient.

## 6.3 High Temperature Results: G-Bands

### 6.3.1 Semi-conducting SWCNTs (514.5 nm)

The high temperature Raman studies were carried out as explained in section 4.2.1. Laser power density on the sample was at about  $60 \text{ W/cm}^2$  and each spectrum was accumulated over a period of 240 seconds.

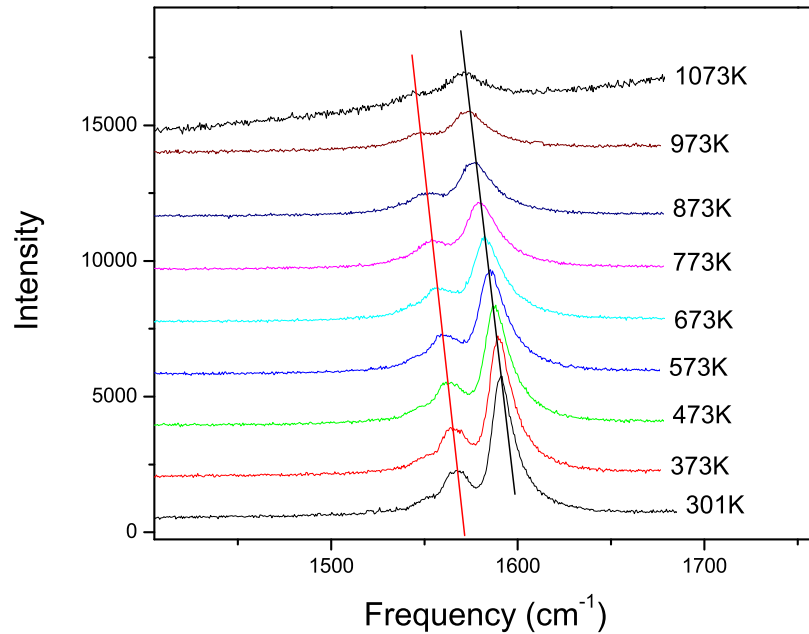


**Figure 6.1:** G bands for semi-conducting SWCNTs excited with the 514.5 nm laser line with decreasing temperatures for the second cooling cycle.

Figure 6.1 shows the Raman spectra for the G bands for semi-conducting SWCNTs excited using the 514.5 nm laser line for the second cooling run. The curves have been displaced for reasons of clarity and therefore the intensities given in the figure are not their absolute intensities. As temperature decreases from 1073K to room temperature the  $G^-$  and  $G^+$  band peak frequencies increase, and the line widths of both modes decrease. A discussion of the line width dependence of the modes with temperature will be given in Section 6.3.4. The intensity of each peak also decreases with increasing temperature.

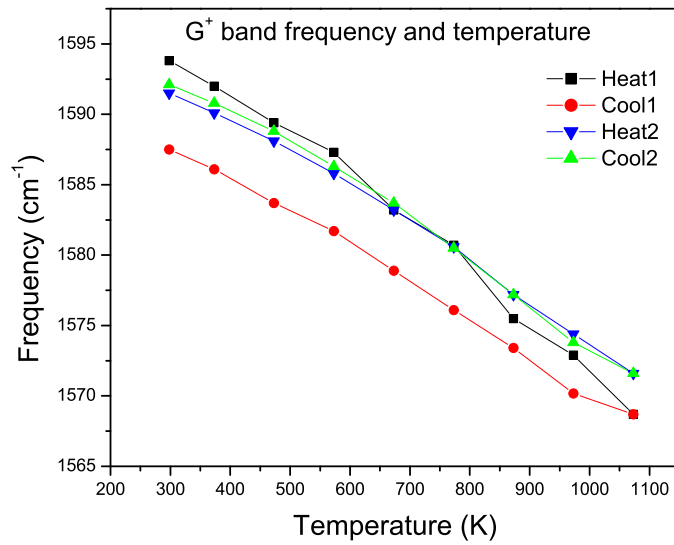


**Figure 6.2a:** Temperature dependence of the  $G^+$  mode frequency in SWCNTs during two heating and cooling runs using the 514.5 nm laser line.

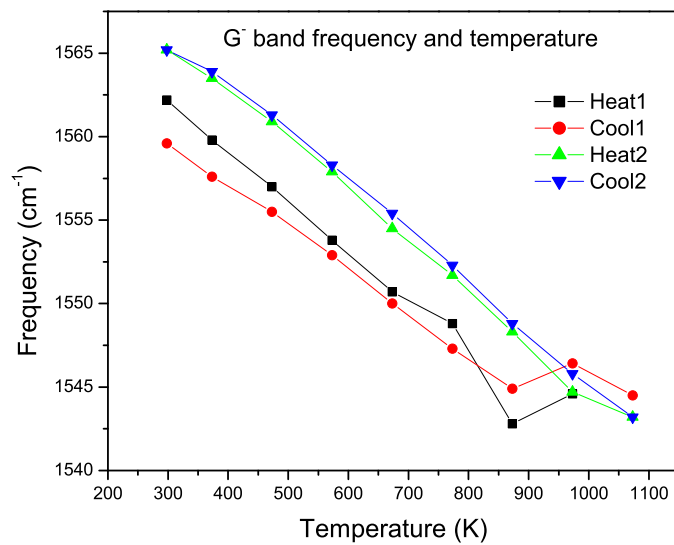


**Figure 6.2b:** Temperature dependence of the  $G^-$  mode frequency in SWCNTs during two heating and cooling runs using the 514.5 nm laser line.

Figures 6.2(a) and (b) show plots of the temperature dependence of the  $G^-$  and  $G^+$  mode frequencies. The first heating and cooling runs show unstable behaviour of

the mode frequencies with temperature. However, the second heating and cooling runs are more stable, showing an increasingly linear relationship between mode frequency and sample temperature. This result can be associated with improved stability of the sample as the spectral contribution of unstable smaller diameter tubes and amorphous carbon is thermally de-activated due to successive annealing.

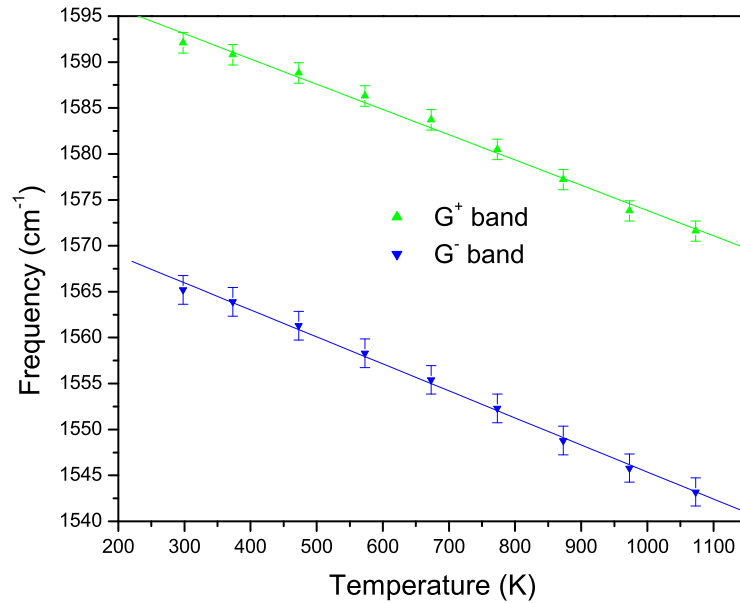
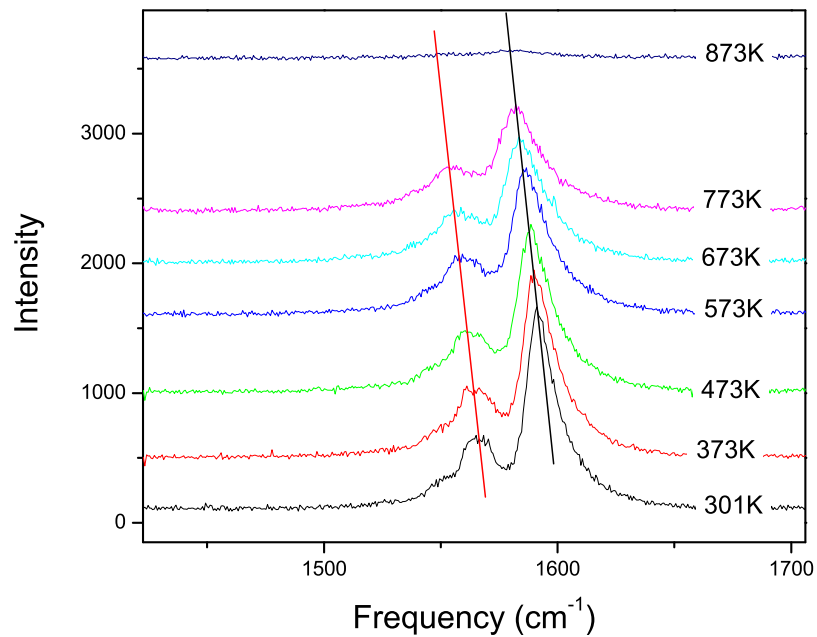


**Figure 6.3:** Temperature dependence of the  $G^+$  and  $G^-$  mode frequencies of SWCNTs excited by the 514.5 nm laser line corresponding to the second cooling run. The  $G^-$  band has a slope of  $-2.94 \text{ cm}^{-1}/100\text{K}$  and the  $G^+$  band has a slope of  $-2.75 \text{ cm}^{-1}/100\text{K}$

Figure 6.3 shows the temperature dependence of the  $G^-$  and  $G^+$  mode frequencies plotted on the same graph for SWCNTs excited using the 514.5 nm laser line for the second cooling run. The change in frequency with temperature shows a close to linear relationship. The slope of the  $G^-$  band is  $-2.94 \text{ cm}^{-1}/100\text{K}$  and that for the  $G^+$  band is  $-2.75 \text{ cm}^{-1}/100\text{K}$ .

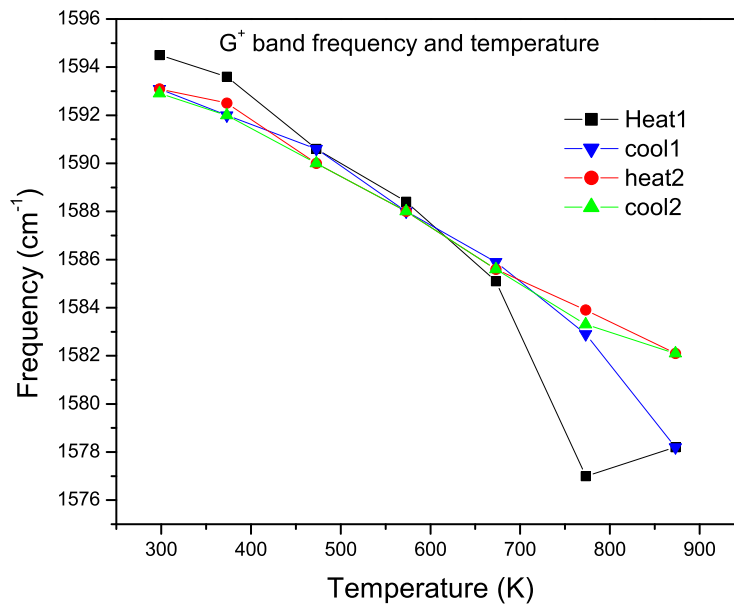
### 6.3.2 Semi-conducting SWCNTs (488.0 nm)

In this section the temperature dependence of the G bands of semi-conducting tubes probed using the 488.0 nm laser line is presented. The laser power density was kept at about 44 W/cm<sup>2</sup> and each spectrum was collected over 240 seconds. These tubes have larger diameters compared to the semi-conducting tubes excited by the 514.5 nm laser line.

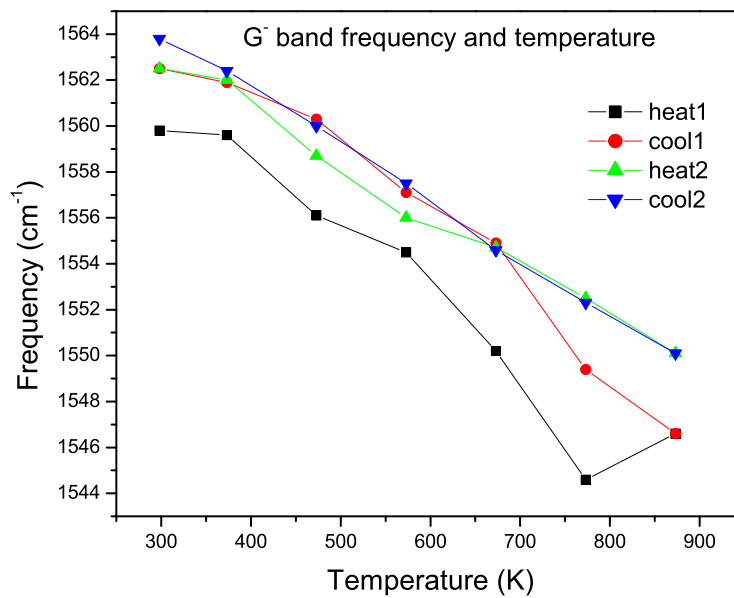


**Figure 6.4:** G bands for semi-conducting SWCNTs measured with decreasing temperatures during the second cooling run, using the 488 nm excitation line. The curves have been displaced for the purposes of clarity.

Figure 6.4 shows the Raman spectra of for the G bands for SWCNTs excited with the 488.0 nm laser line for the second cooling run. It also shows an increase in  $G^-$  and  $G^+$  mode frequency with decreasing temperatures. There is also a decrease in the line widths of the  $G^+$  and  $G^-$  modes with decreasing temperatures. The intensity of each mode increases as temperature reduces.

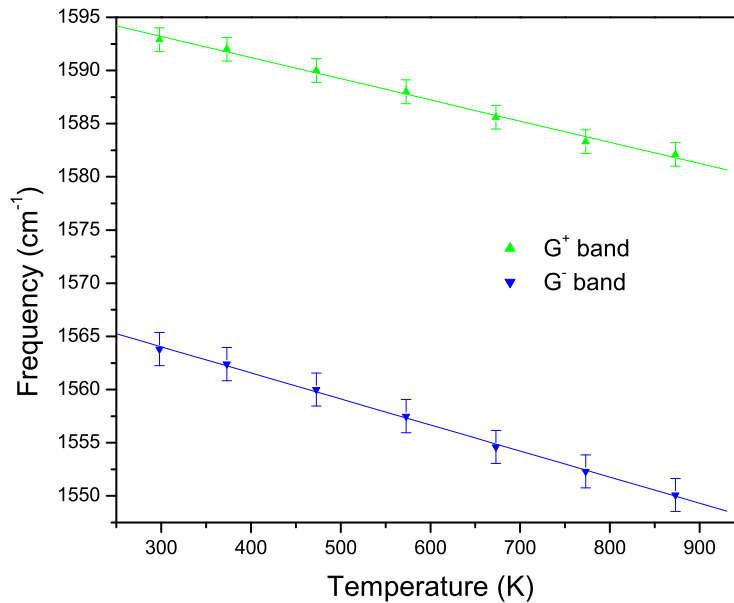


**Figure 6.5a:** Temperature dependence of the G<sup>+</sup> mode frequencies in SWCNTs during two heating and cooling runs using the 488.0 nm excitation line.



**Figure 6.5b:** Temperature dependence of the G<sup>-</sup> mode frequencies in SWCNTs during two heating and cooling cycles using the 488.0 nm excitation.

Figures 6.5(a) and (b) show the temperature dependence of the  $G^+$  and  $G^-$  mode frequencies. The first heating and cooling runs also show unstable behaviour of the mode frequencies with temperature, and the second heating and cooling runs show more stability.



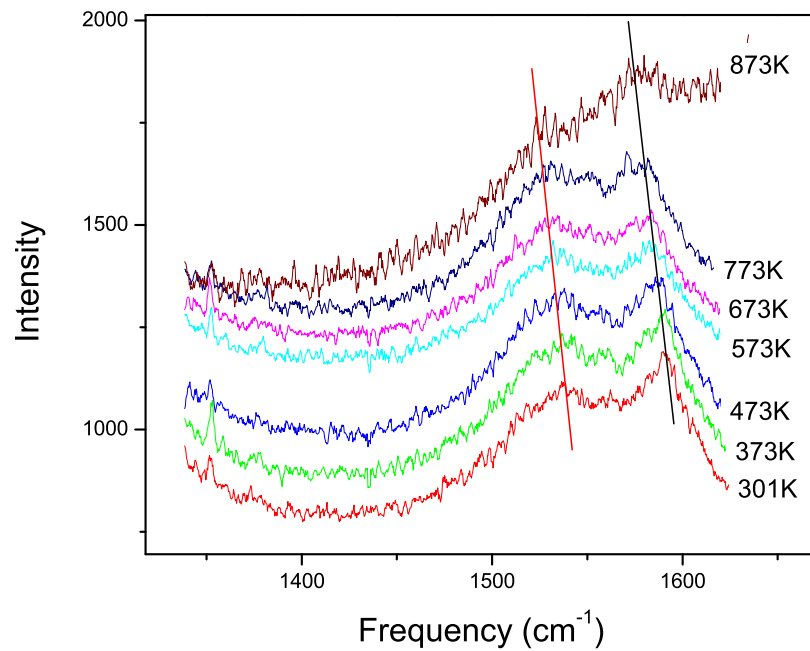
**Figure 6.6:** Temperature dependence of the  $G^+$  and  $G^-$  mode frequencies of SWCNTs excited by the 488.0 nm laser line corresponding to the second cooling run, with the slopes being  $-2.45 \text{ cm}^{-1}/100\text{K}$  for the  $G^-$  band and  $-1.99 \text{ cm}^{-1}/100\text{K}$  for the  $G^+$  band.

Figure 6.6 shows the temperature dependence of the  $G^+$  and  $G^-$  mode frequencies corresponding to the second cooling run for SWCNTs excited with the 488.0 nm laser line plotted on the same graph. It shows a linear decrease in frequency of the G-bands with increasing temperature, with respective slopes being  $2.45 \text{ cm}^{-1}/100\text{K}$  for the  $G^-$  band and  $1.99 \text{ cm}^{-1}/100\text{K}$  for the  $G^+$  band.

### 6.3.3 Metallic SWCNTs (647.1 nm)

For the 647.1 nm excitation, a laser power density of  $40 \text{ W}/\text{cm}^2$  was used. The accumulation time for each Raman spectrum was 240 seconds. The figures below

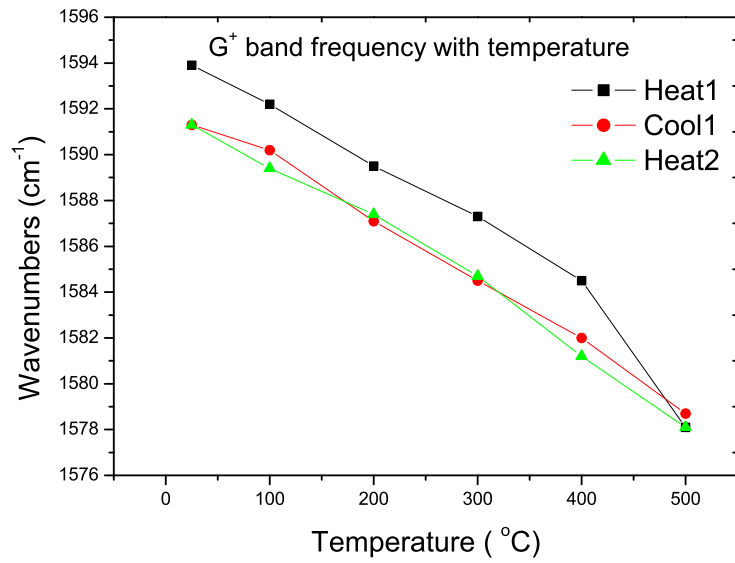
show the temperature dependence of the  $G^-$  and  $G^+$  bands in metallic tubes.



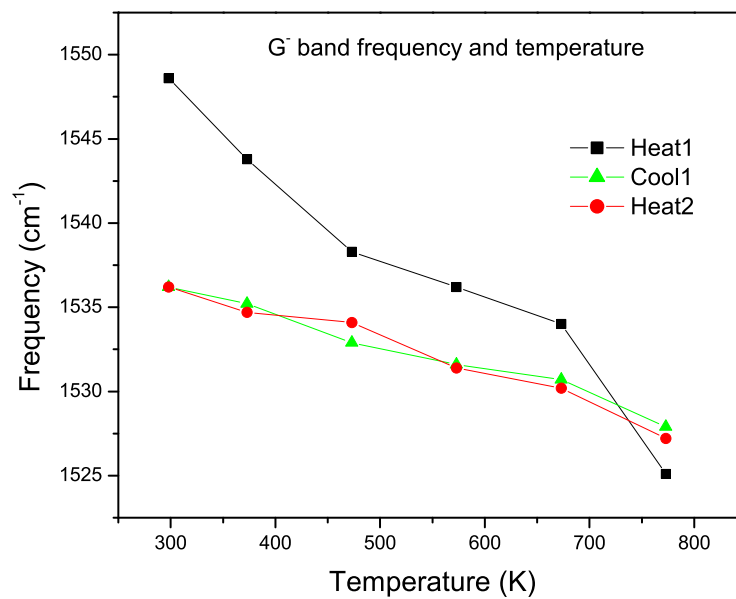
**Figure 6.7:**  $G$  bands for metallic SWCNTs measured with decreasing temperatures during the first cooling run using 647.1 nm excitation. The curves have been displaced for the purposes of clarity.

Figure 6.7 shows the Raman spectra for the  $G$  bands of SWCNTs excited with the 647.1 nm laser line for the first cooling run. The 647.1 nm laser line excites predominantly metallic SWCNTs. The  $G^-$  band in metallic SWCNTs is significantly broader than that for semi-conducting SWCNTs. As with semi-conducting SWCNTs, the  $G^+$  and  $G^-$  band peak frequencies increase with decreasing temperatures. The  $G^+$  band line width decreases as temperature decreases. However, the  $G^-$  band line width increases with decreasing temperature. An explanation of this behaviour will be given in section 6.4.4. With the red 647.1 nm laser line, the increase in the background radiation with increasing temperature limits the highest temperature for Raman measurements at 873K. Above 873K the sample holder in the heating cell becomes red hot resulting in an increase in the thermal background radiation.





**Figure 6.8a:** Temperature dependence of the  $G^+$  mode frequencies in SWCNTs during heating and cooling runs using the 647.1 nm laser line.



**Figure 6.8b:** Temperature dependence of the  $G^-$  mode frequencies in SWCNTs during heating and cooling runs using the 647.1 nm laser line.

Figures 6.8(a) and (b) show the temperature dependence of the  $G^+$  and  $G^-$  mode frequencies. The first heating run shows very unstable behaviour, but the first cooling and second heating runs are more stable; therefore the second cooling cycle was not taken.

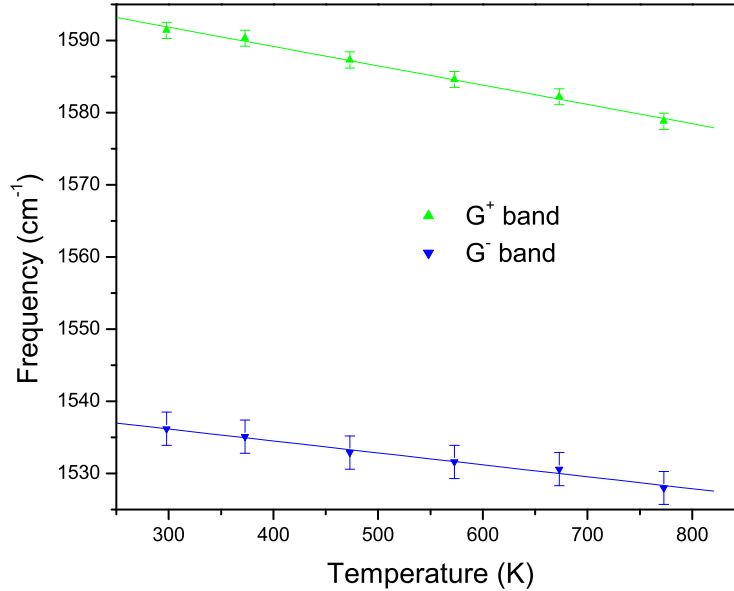


**Figure 6.9:** Temperature dependence of the  $G^+$  and  $G^-$  mode frequencies of SWCNTs excited by the 647.1 nm laser line corresponding to the first cooling run, with the slopes being  $-1.67 \text{ cm}^{-1}/100\text{K}$  for the  $G^-$  band and  $-2.68 \text{ cm}^{-1}/100\text{K}$  for the  $G^+$  band.

Figure 6.9 shows the temperature dependence of the  $G^+$  and  $G^-$  mode frequencies of metallic SWCNTs for the first cooling run. As in semi-conducting tubes, there is also a linear decrease of the  $G^+$  and  $G^-$  mode frequencies with increasing temperatures. For metallic tubes, the slope of the  $G^-$  band is  $-1.67 \text{ cm}^{-1}/100\text{K}$  and  $-2.68 \text{ cm}^{-1}/100\text{K}$  for the  $G^+$  band.

Table 6.1 gives a summary of the slopes of the  $G^+$  and  $G^-$  bands of the different types of SWCNTs in the high temperature range. A discussion of these results will be given in section 6.8.

**Table 6.1:** Slopes of the graphs of frequency versus temperature for the  $G^+$  and  $G^-$  bands of metallic and semi-conducting SWCNTs.

Laser	Electronic Property	$G^-$ slope( $\text{cm}^{-1}/100\text{K}$ )	$G^+$ slope ( $\text{cm}^{-1}/100\text{K}$ )
488.0 nm	Semi-conducting	-2.450	-1.992
514.5 nm	Semi-conducting	-2.940	-2.750
647.1 nm	Metallic	-1.669	-2.680

### 6.3.4 G-Band Linewidth in SWCNTs

In this section the temperature dependence of the linewidths of the G-band for metallic and semi-conducting tubes is presented. The Raman line width is usually a measure of phonon life time and is determined by the scattering mechanism, whether it is temperature-independent such as scattering from lattice defects or whether it is temperature-dependent such as scattering from phonons. The variation of the phonon line width with temperature was expressed by Iliev *et al.* (2000) as

$$\Delta T = \gamma + \Gamma_0 \left( 1 + \frac{2}{e^x - 1} \right) \quad (6.1)$$

where  $\gamma$  is the temperature-independent part of the line width,  $x = \hbar\omega/2k_B T$ , where  $\hbar\omega$  is the phonon energy and  $k_B$  is the Boltzmann constant.

Jorio *et al.* (2002) studied the temperature dependence of the line width of the G-band for semi-conducting SWCNTs between 110K and 610K. They observed that the line widths of both the  $G^-$  and  $G^+$  bands increase with increasing temperatures. This is in agreement with the prediction of Equation 6.1.

The graphs below show the temperature dependence of the linewidths of the G-bands of metallic and semi-conducting SWCNTs. The laser power density used is as indicated in the figures. The measured linewidths are a convolution of the instrumental function and the true linewidth. In this case the instrumental function was directly measured using the same experimental setup as in section 3.4.1 using

a laser plasma line and found to be  $1.67 \text{ cm}^{-1}$ . Deconvolution of the narrower peaks was carried out using the Fast Fourier Transform procedure in the Origin 6.1 software. The broader  $G^-$  and  $G^+$  band linewidths of metallic SWCNTs were not deconvoluted. Hughes (1968) indicates that it is unnecessary to correct for instrument function broadening where the broadening is  $\leq 10\%$  of the measured linewidth.

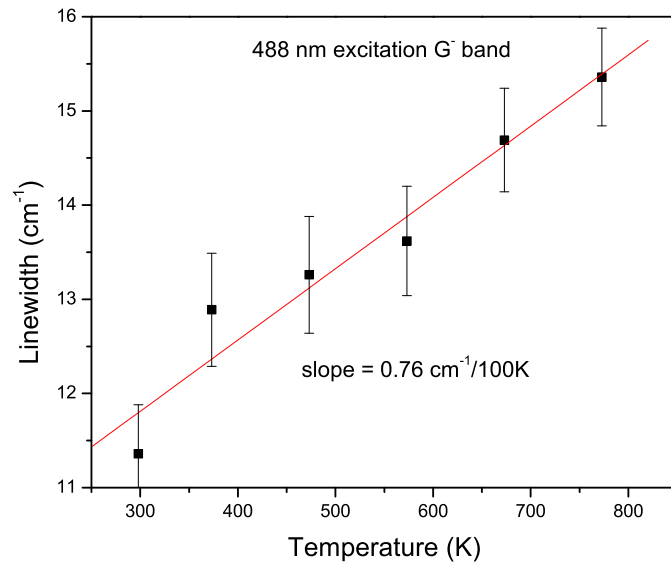


**Figure 6.10a:** Temperature dependence of the line width of the  $G^-$  band for SWCNTs excited with the 488.0 nm laser line using a laser power density of  $44 \text{ W/cm}^2$  on the sample. The slope of the graph is  $0.76 \text{ cm}^{-1}/100\text{K}$ .

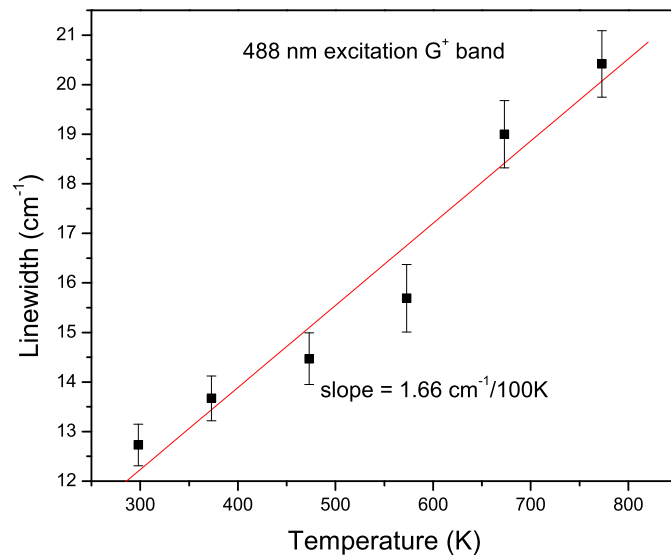


**Figure 6.10b:** Temperature dependence of the line width of the  $G^+$  band for SWCNTs excited with the 488.0 nm laser line using a laser power density of  $44 \text{ W/cm}^2$  on the sample. The slope of the graph is  $1.66 \text{ cm}^{-1}/100\text{K}$ .

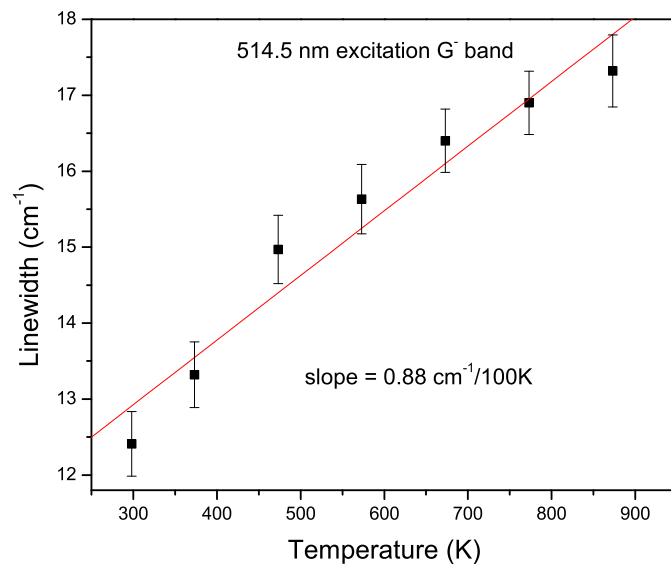


**Figure 6.11a:** Temperature dependence of the line width of the  $G^-$  band for SWCNTs excited with the 514.5 nm laser line using a laser power density of  $60 \text{ W/cm}^2$  on the sample. The slope of the graph is  $0.88 \text{ cm}^{-1}/100\text{K}$ .

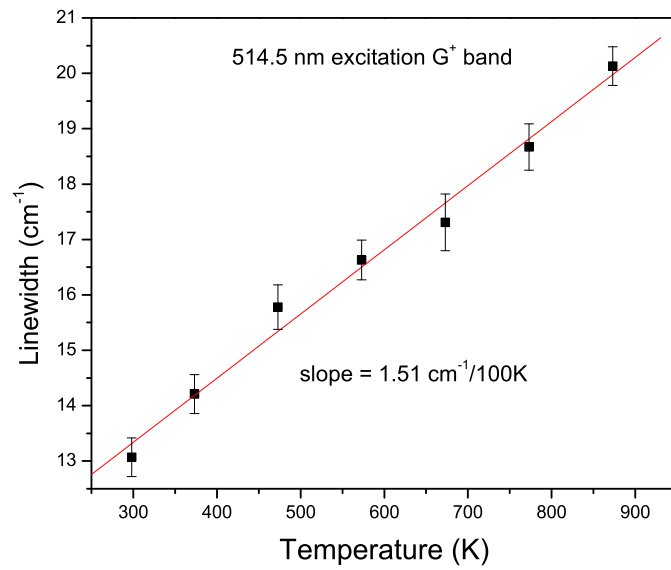


**Figure 6.11b:** Temperature dependence of the line width of the  $G^+$  band for SWCNTs excited with the 514.5 nm laser line using a laser power density of  $60 \text{ W/cm}^2$  on the sample. The slope of the graph is  $1.51 \text{ cm}^{-1}/100\text{K}$ .

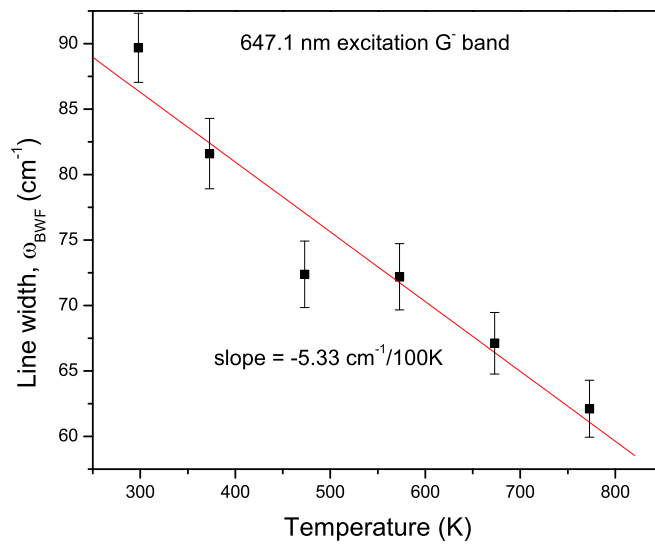


**Figure 6.12a:** Temperature dependence of the line width of the  $G^-$  band (BWF line) for SWCNTs excited by the 647.1 nm laser line using a laser power density of  $20 \text{ W/cm}^2$  on the sample. The slope of the graph is  $-5.33 \text{ cm}^{-1}/100\text{K}$ .

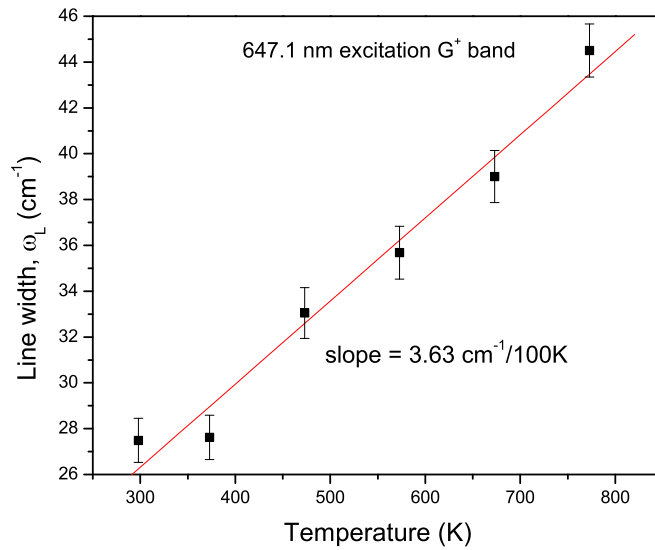


**Figure 6.12b:** Temperature dependence of the line width of the  $G^+$  band for SWCNTs excited with the 647.1 nm laser line using a laser power density of  $20 \text{ W/cm}^2$  on the sample. The slope of the graph is  $3.63 \text{ cm}^{-1}/100\text{K}$ .

The line widths of the  $G^+$  and  $G^-$  bands for semi-conducting SWCNTs excited with the 488.0 nm and 514.5 nm laser lines increase with increasing sample temperature. This is in agreement with Equation 6.1. The  $G^+$  band line width of SWCNTs excited with the 647.1 nm laser line also increases with increase in temperatures. However, the BWF line shape of the  $G^-$  band in metallic SWCNTs decreases with increasing temperature, opposite to what would be expected according to Equation 6.1

Uchida *et al.* (2004) applied the model of plasmon-phonon coupling and attributed this decrease in line width to a decrease in the coupling constant  $|1/q|$ , owing to the proportionality between these quantities. The coupling constant according to this model is related to the formation of a band of plasmons in a bundle of SWCNTs; the plasmon band in turn depends on the intertube distance in the bundle. It is supposed that as the temperature increases, thermal expansion results in an increase of the intertube distance in the bundles, resulting in the suppression of the plasmon band formation. This results in a decrease in the coupling constant

and the width of the BWF  $G^-$  line.

However, the electron-phonon coupling model can also be used to explain the narrowing of the metallic  $G^-$  band linewidth with increasing temperatures. Lazzeri *et al.* (2006) expressed the linewidth of a phonon as

$$\gamma = \gamma^{an} + \gamma^{EP} \quad (6.2)$$

where  $\gamma^{an}$  is due to the interaction with other phonons and  $\gamma^{EP}$  is due to the interaction with electron-hole pairs.  $\gamma^{EP}$  is determined by electron-phonon coupling (EPC) and is present only if the electronic gap is zero. This means that for semi-conducting SWCNTs  $\gamma^{EP}=0$ .

The EPC contribution of the linewidth for the LO mode in metallic SWCNTs is represented as

$$\gamma_{\Gamma-LO}^{EP} = \frac{2\sqrt{3}\hbar a_0^2 \langle D_{\Gamma}^2 \rangle_F}{\pi M \omega_{\Gamma} \beta d}. \quad (6.3)$$

where  $a_0$  is the graphite lattice spacing,  $M$  is the carbon atomic mass,  $\omega_{\Gamma}$  is the vibrational frequency of the  $E_{2g}$  phonon,  $\beta$  is the slope of the electron bands near the Fermi level,  $d$  is the SWCNT diameter and  $\langle D_{\Gamma}^2 \rangle_F$  can be defined as

$$\langle D_{\Gamma}^2 \rangle_F = \sum_{i,j}^{\pi} |D_{\mathbf{k}_i, \mathbf{k}_j}|^2 / 4 \quad (6.4)$$

where the sum is taken over the two degenerate  $\pi$  bands at the Fermi level  $\epsilon_F$ .  $D$  is the EPC.

As discussed in section 3.6.2, several papers consider the Kohn anomaly associated with EPC as being responsible for the downshift of the LO mode frequency in metallic SWCNTs. EPC also reduces the LO phonon lifetime, resulting in an increase in the phonon linewidth (Piscanec *et al.* 2007b). Popov and Lambin (2006) showed that the Kohn anomaly is strongly suppressed with increasing temperature. Agrestini *et al.* (2004) showed that the reduction in the Kohn anomaly is a result of the reduction in EPC and results in a narrower phonon linewidth. Therefore, the narrowing of the linewidth of the  $G^-$  band of metallic SWCNTs with temperature observed in our experiments is consistent with the weakening of EPC with



increasing temperatures. Equations 6.3 and 6.4 show that a reduction in EPC leads to a reduction in the value of  $\langle D_{\Gamma}^2 \rangle_F$ , which in turn leads to a reduction of  $\gamma^{EP}$ . This EPC model applies to isolated SWCNTs or SWCNTs in a bundle, whereas the plasmon-phonon model seems to apply only for bundled SWCNTs.

## 6.4 Radial Breathing Modes

In this section the diameters of the SWCNTs in resonance with the 514.5 nm, 488.0 nm and the 647.1 nm laser lines were calculated and the corresponding chiralities determined. The temperature dependence of the RBM is then discussed.

### 6.4.1 Calculation of SWCNT Diameters

As mentioned earlier in section 3.4.1, the RBM frequency can be used to calculate the diameter of a SWCNT. According to Alvarez *et al.* (2000) the diameter of a SWCNT can be calculated using the relation

$$\omega(\text{cm}^{-1}) = \frac{232(\text{cm}^{-1}\text{nm})}{d(\text{nm})} + 6.5 \text{ cm}^{-1} \quad (6.5)$$

The deconvolution of each RBM spectrum was done by fitting Lorentzian line shapes using the peak fitting procedure in Origin software. The errors on the RBM peak frequencies due to the deconvolution are less than 0.5%.

#### Semi-conducting SWCNTs: 514.5 nm

Figure 6.13 shows the de-convoluted RBM spectra of SWCNTs produced using the 25 at.% LaNi<sub>5</sub> catalyst at a helium pressure of 60 kPa, probed using the 514.5 nm (2.41eV) laser line. Lorentzian peaks are fitted to each of the predominant peaks. Table 6.1 gives the diameter corresponding to each peak and the possible chirality. For chirality assignment an algorithm based on Equation (2.3) was developed that looks for all possible  $(n, m)$  combinations for nanotubes in the diameter range 0.556 nm - 2.063 nm.

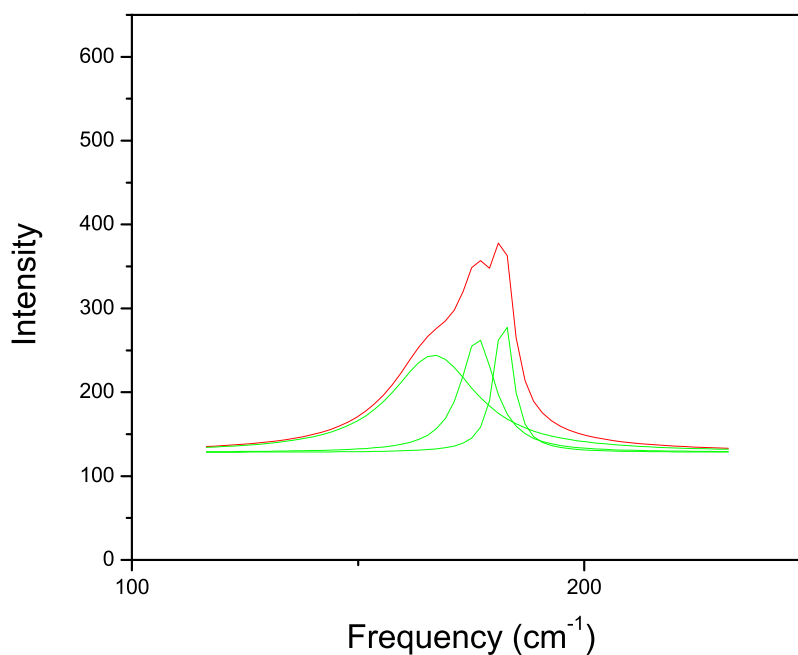


**Figure 6.13:** Deconvoluted radial breathing mode for semi-conducting tubes excited with the 514.5 nm laser line.

**Table 6.2:** Calculated diameters and corresponding chiralities for semi-conducting tubes excited by the 514.5 nm laser line.

Peak ( $\text{cm}^{-1}$ )	Intensity	Line Width ( $\text{cm}^{-1}$ )	Diameter (nm)	Chirality
181.07	250.76	9.53	1.33	(13, 6)
174.82	182.12	10.87	1.38	(11, 9) or (15, 4)
164.01	87.30	23.72	1.47	(14, 7)

#### Semi-conducting SWCNTs: 488.0 nm

Figure 6.14 shows the de-convoluted RBM spectra of SWCNTs produced using the 25 at.%  $\text{LaNi}_5$  catalyst at a helium pressure of 60 kPa, probed using the 488.0 nm (2.54eV) laser line. The calculated diameters and corresponding chiralities are given in Table 6.2.

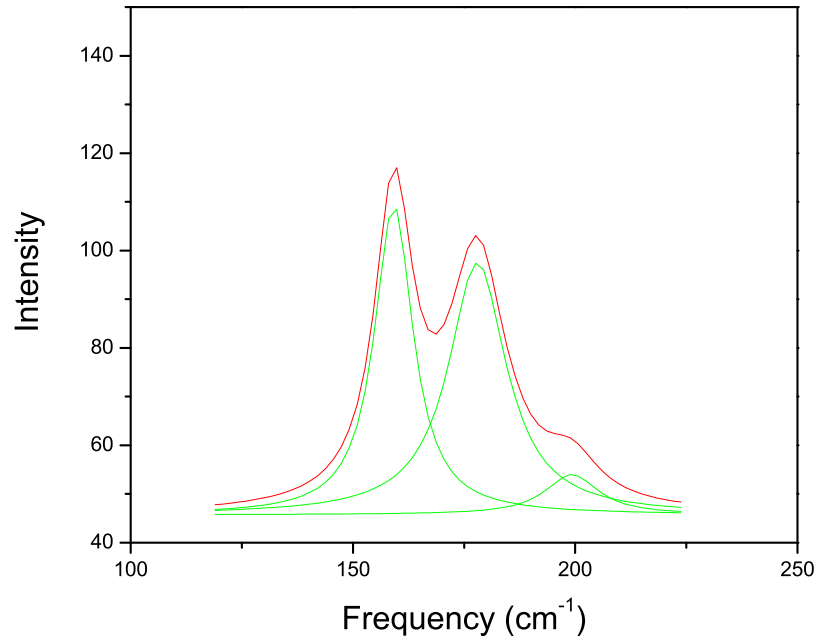


**Figure 6.14:** Deconvoluted radial breathing mode for semi-conducting tubes excited with the 488.0 nm laser line.

**Table 6.3:** Calculated diameters and corresponding chiralities for semi-conducting tubes excited by the 488.0 nm laser line.

Peak ( $\text{cm}^{-1}$ )	Intensity	Line Width ( $\text{cm}^{-1}$ )	Diameter ( $\text{nm}$ )	Chirality
199.3	23.98	16.32	1.20	(12, 5)
179.0	57.42	18.68	1.35	(16, 2)
158.2	88.50	11.40	1.52	(13, 9)

#### Metallic SWCNTs: 647.1 nm

Figure 6.15 shows the radial breathing modes for metallic nanotubes excited with the 647.1 nm (1.92eV) laser line. Table 6.2 gives the calculated diameters and the chirality for each peak.

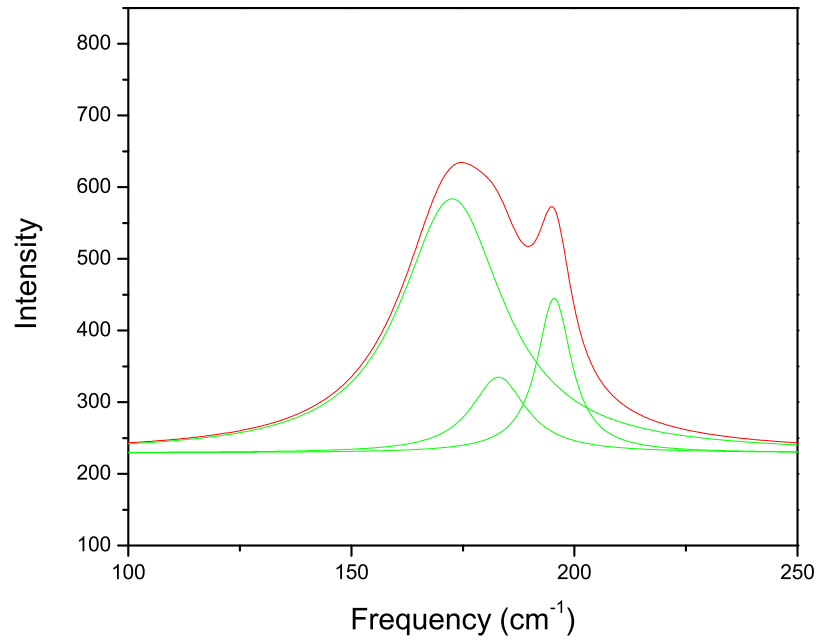


**Figure 6.15:** Deconvoluted radial breathing mode for metallic nanotubes excited using the 647.1 nm laser line.

**Table 6.4:** Calculated diameters and corresponding chiralities for metallic tubes excited by the 647.1 nm laser line.

Peak ( $\text{cm}^{-1}$ )	Intensity	Line Width ( $\text{cm}^{-1}$ )	Diameter ( $\text{nm}$ )	Chirality
190.16	203.50	9.43	1.26	(12, 6)
177.86	120.58	15.04	1.35	(14, 5)
166.52	235.24	28.09	1.45	(12, 9)

It is noted however, that the RBM method and the G-band splitting method (Equation 3.13) may give different results of SWCNTs diameter, particularly for the SWCNTs excited using the 488.0 nm laser line. According to the method of calculating SWCNT diameters using the radial breathing mode, the 514.5 nm laser line is strongly in resonance with SWCNTs of diameter 1.33 nm, which is very close to the diameter obtained from the G-band splitting method for a splitting of 27.5

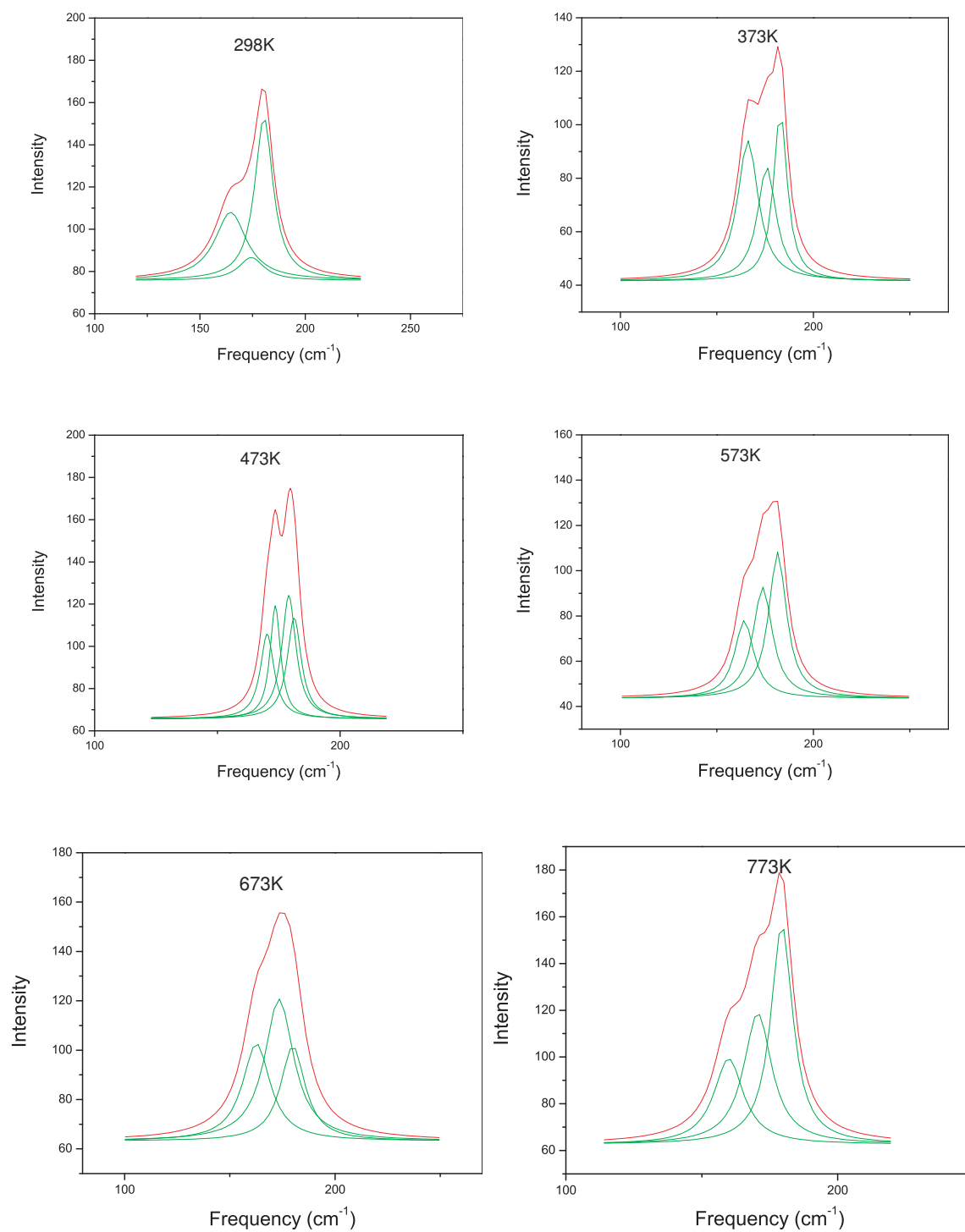
$\text{cm}^{-1}$  which is 1.32 nm.

The RBM method gives diameters of 1.35nm and 1.52 nm for SWCNTs excited with the 488.0 nm laser line while the G-band splitting method gives a diameter of 1.26 nm for the same excitation wavelength for a G-band split of  $30 \text{ cm}^{-1}$ . The following would be a plausible explanation on why the diameters are different: From sections 6.4.1 and 6.4.3, the RBMs of SWCNTs excited by the 488.0 nm laser line exhibit two prominent peaks, whose peak frequencies differ by about  $20 \text{ cm}^{-1}$ . This means that this laser lines excites two sets of SWCNT diameters. This therefore means that the resulting G-band is a superposition of the G-bands of these tubes and the peak positions of the resulting G-band are a superposition of the peak positions of the different G-bands. This superposition generates an uncertainty in the G-band position values, so that the RBM method would be more reliable in this case.

## High Temperature Results

### 6.4.2 514.5 nm Excitation

The 514.5 nm laser line of the  $\text{Ar}^+$  ion laser is strongly in resonance with nanotubes of diameter  $1.33 \pm 0.05 \text{ nm}$ . The tubes are semi-conducting. The laser power density on the sample was  $60 \text{ W/cm}^2$  and each Raman spectrum was collected over a 240 seconds period. In the graphs showing the frequency reduction of the RBM's for the various laser excitations (figures 6.17, 6.19 and 6.21) a standard procedure was used. Initially a prominent RBM was selected within each RBM spectrum and this or that at the nearest lower frequency was tracked as the measurement temperature was increased.



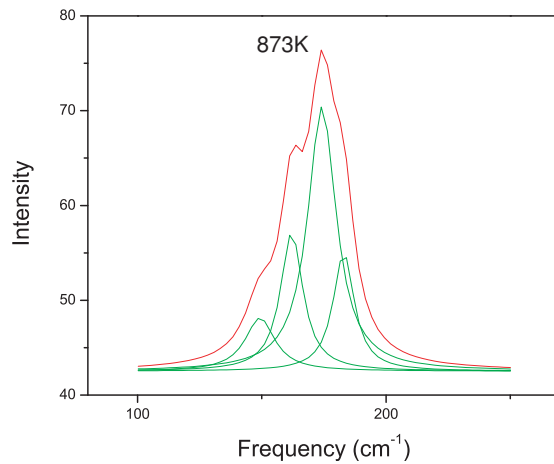


**Figure 6.16:** Deconvoluted RBM spectra of SWCNTs at different temperatures for the 514.5 nm excitation line, showing the change in line shape of the RBM with increasing temperatures.

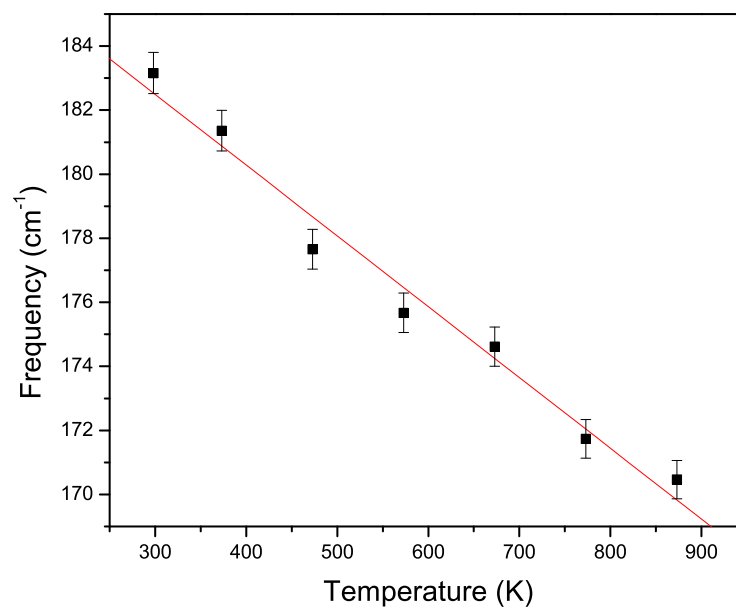


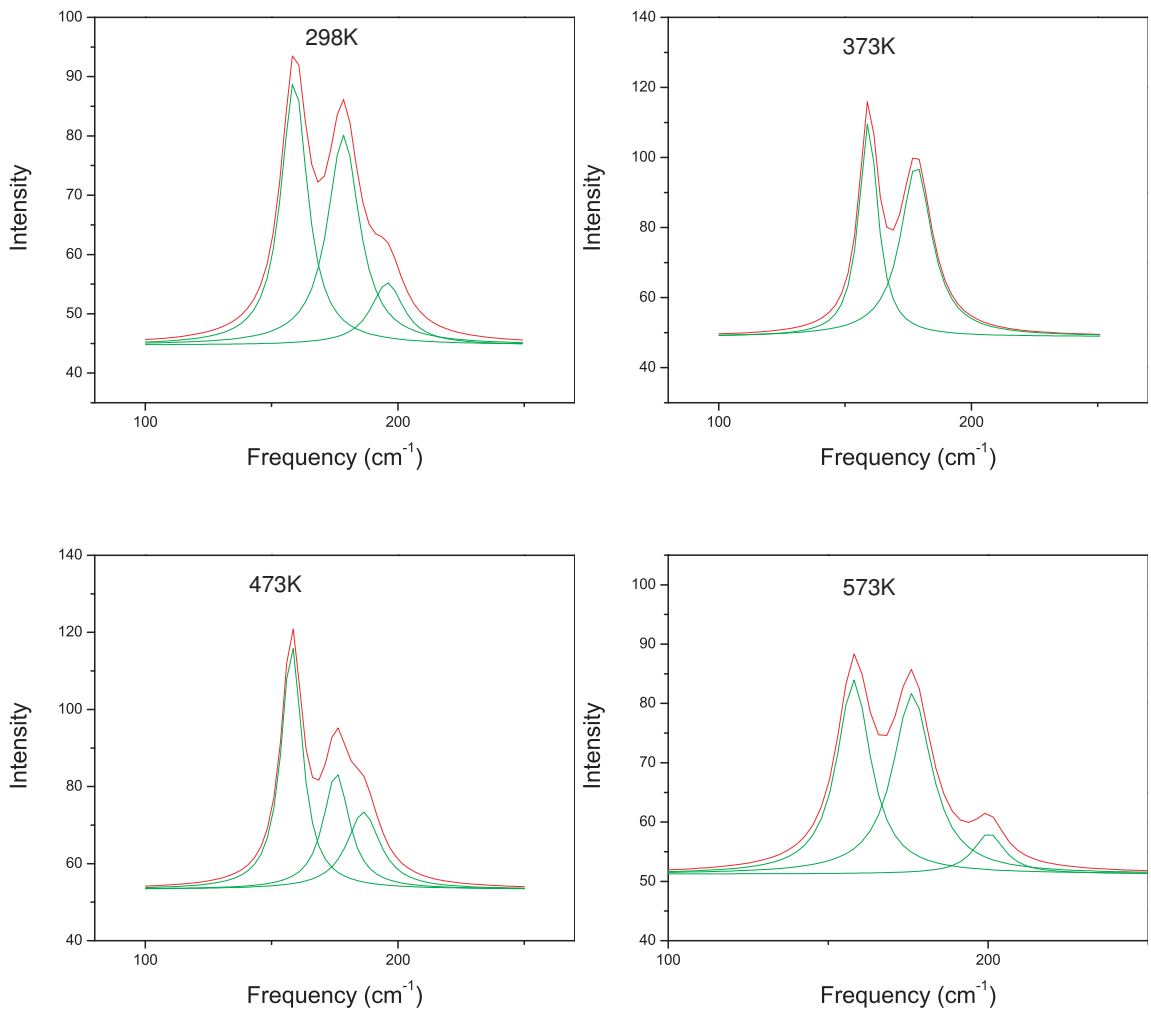
**Figure 6.17:** Temperature dependence of the radial breathing mode for the  $\omega_{181}$  peak obtained using the 514.5 nm laser line, with slope being  $-1.95 \text{ cm}^{-1}/100\text{K}$ .

There is a decrease in frequency of the entire RBM feature as temperature increases. There is also a significant change in the line shape of the RBM with increasing temperature. These changes in frequency and lineshape are however reversible,

i.e if temperature is lowered initial peak position and line shapes are maintained. A detailed explanation on the change of the lineshape of the entire RBM with temperature will be given in Section 6.7.2. Peak fitting to the RBMs was done using Lorentzian fits. The slope,  $(\frac{\partial\omega_R}{\partial T})$  is  $-1.95 \text{ cm}^{-1}/100\text{K}$  for the  $\omega_{181}$  peak.

### 6.4.3 488.0 nm Excitation

The dominant diameters of tubes probed by the 488 nm laser line are  $1.52 \pm 0.05$  nm and  $1.35 \pm 0.05$  nm. The tubes are semi-conducting and laser power density used was  $44 \text{ W}/\text{cm}^2$  and each spectrum was collected over a time of 240 seconds.





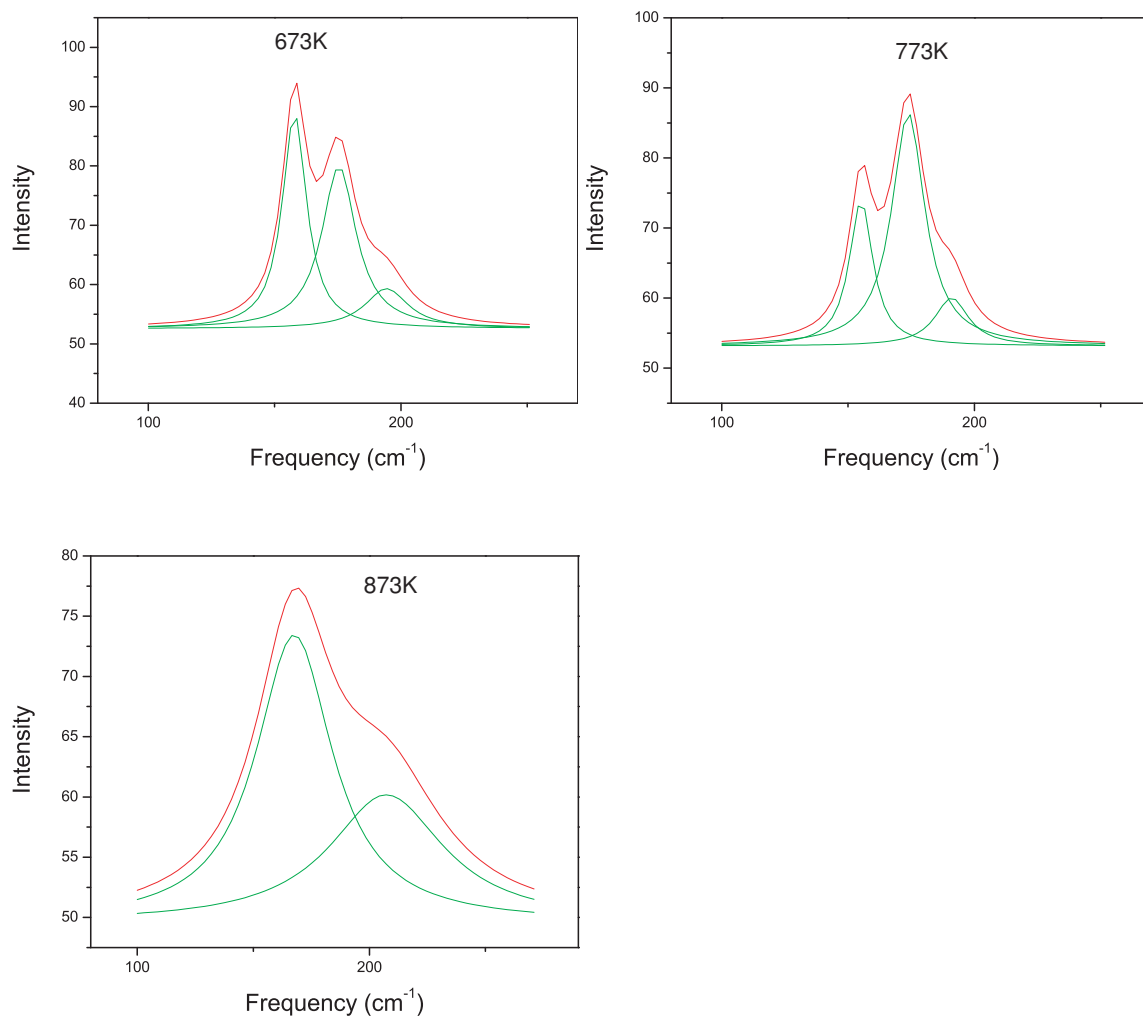


**Figure 6.18:** Deconvoluted radial breathing mode spectra for SWCNTs at different temperatures excited using the 488.0 nm excitation line.

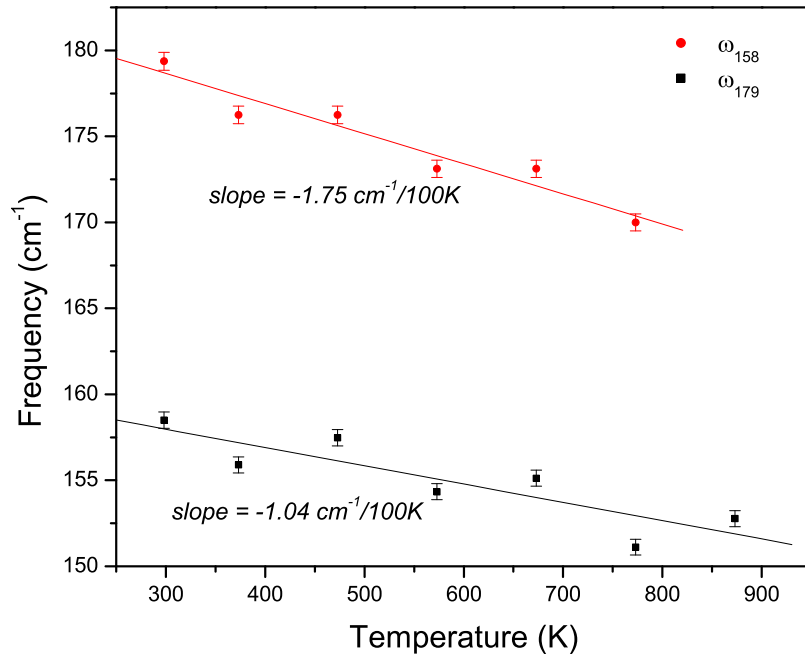
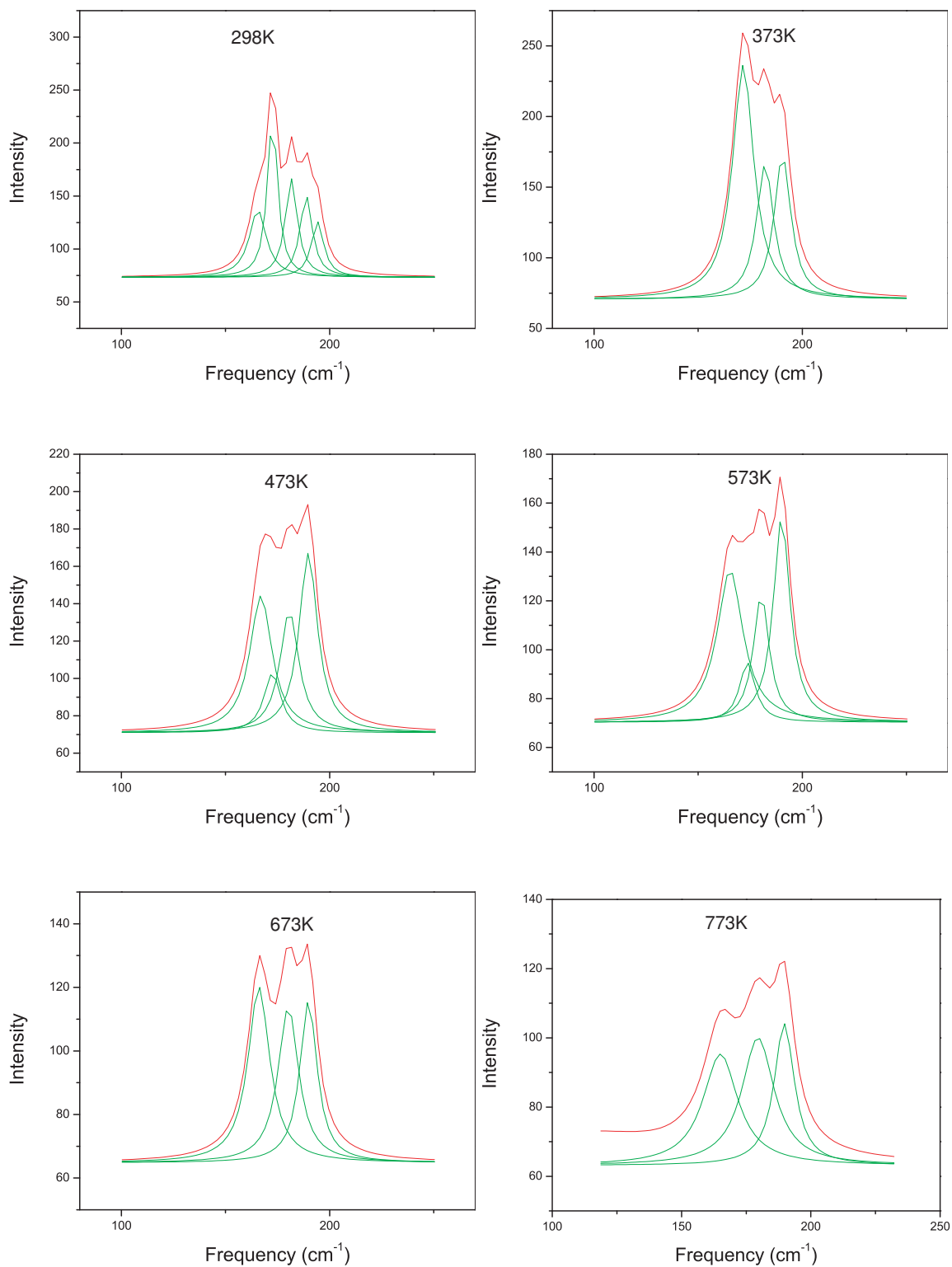


**Figure 6.19:** Temperature dependence of the radial breathing mode for the  $\omega_{179}$  and  $\omega_{158}$  peaks for semi-conducting SWCNTs excited by the 488.0 nm laser line.

There is a decrease of RBM peak positions with increasing temperature. There is also a significant change in the line shape of the RBM with changes in temperature. The 488.0 nm RBMs have two distinct peaks at frequency  $179 \text{ cm}^{-1}$  and frequency  $158 \text{ cm}^{-1}$  at room temperature corresponding to diameters of 1.34 nm and 1.52 nm respectively. At room temperature the  $\omega_{158}$  peak is more prominent. As temperature is raised to 500K, the  $\omega_{179}$  peak becomes more prominent as compared with the  $\omega_{158}$  peak.

#### 6.4.4 647.1 nm Excitation

This laser probes mostly metallic nanotubes of average diameter  $1.45 \pm 0.05 \text{ nm}$ . Laser power density used was  $20 \text{ W/cm}^2$ . The accumulation time for each Raman spectrum was 240 seconds.



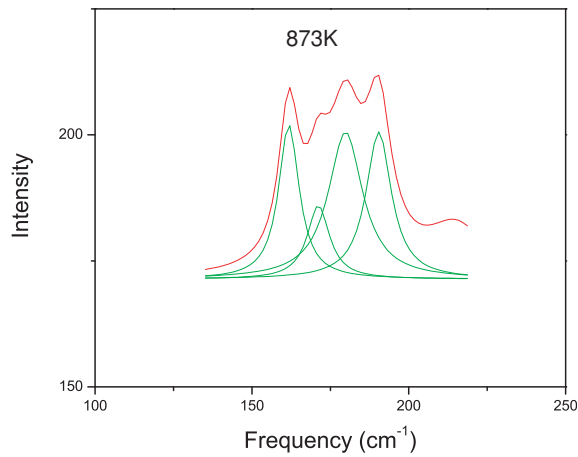


**Figure 6.20:** Deconvoluted radial breathing mode spectra of SWCNTs at different temperatures excited using the 647.1 nm excitation line.

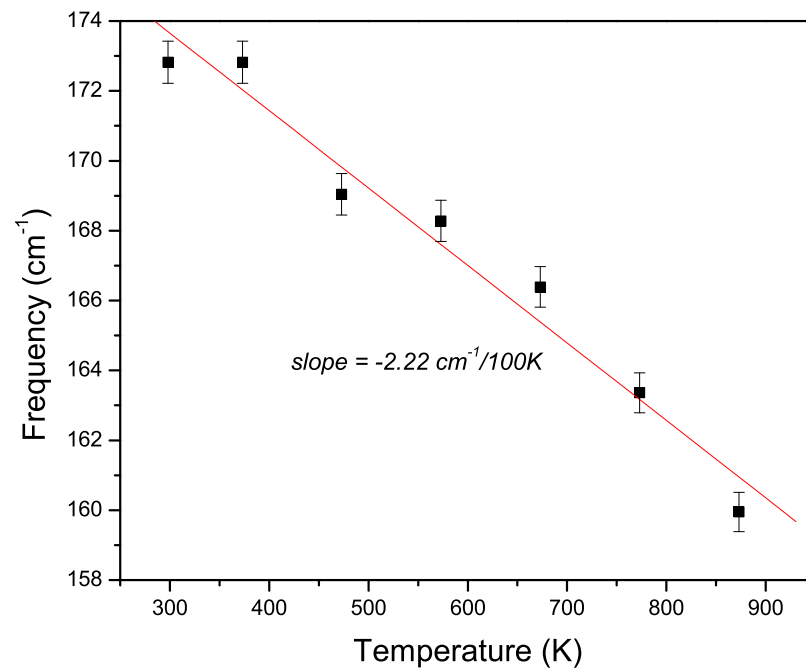


**Figure 6.21:** Temperature dependence of the radial breathing mode for the  $\omega_{190}$  peak for metallic SWCNTs excited by the 647.1 nm laser line

The RBM peak positions shift towards the lower wave number region as temperature increases.

Table 6.5 shows the rate of decrease of the RBM peak frequency with temperature for metallic and semi-conducting SWCNTs. A discussion of these results will be presented in section 6.8.

**Table 6.5:** Slopes of the graphs of frequency versus temperature for the RBM modes excited with various laser wavelengths.

Laser Excitation	Peak	$(\partial\omega_{RBM}/\partial T)$
488.0 nm	$\omega_{158}$	-1.04
488.0 nm	$\omega_{179}$	-1.75
514.5 nm	$\omega_{181}$	-1.95
647.1nm	$\omega_{166}$	-2.22

## 6.5 Low Temperature Raman Scattering Studies

### 6.5.1 Semi-conducting SWCNTs: 514.5 nm

In this section the Raman scattering results of semi-conducting SWCNTs at low temperatures are described. The bucky paper used for this experiment was produced using the method described in Section 6.2. and then taken through two annealing cycles to a maximum temperature of 873K in a Linkam heating cell to improve on its stability and purity.

Raman spectra were collected in the cryostat described in Section 4.4 at various temperatures as the sample temperature was raised from 77K to 400K. The temperature was held for about five minutes at each stage before a spectrum was recorded to allow for a temperature equilibrium to be reached within the cryostat. The 514.5 nm laser line was used for this work. Power density at the sample was approximately 30W/cm<sup>2</sup>. Each Raman spectrum was accumulated over a time of 300 seconds.

Both the G<sup>+</sup> and G<sup>-</sup> modes show a linear decrease of frequency with increasing

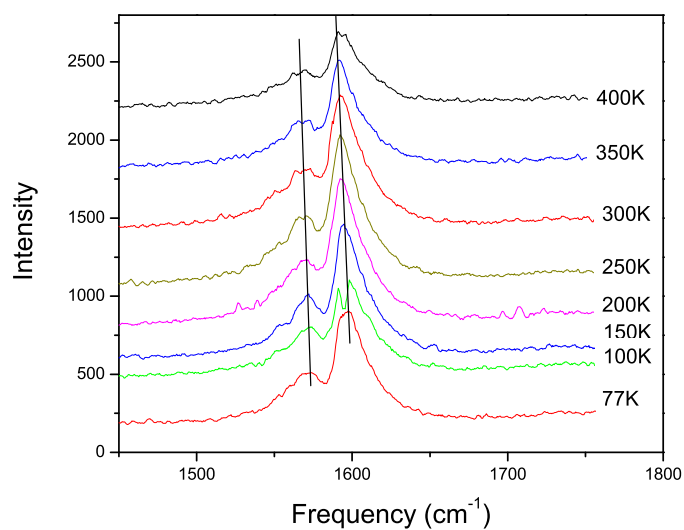


**Figure 6.22a:** Temperature dependence of the G band for the low temperature region for semi-conducting SWCNTs excited using the 514.5 nm excitation. The curves have been displaced for the purposes of clarity.

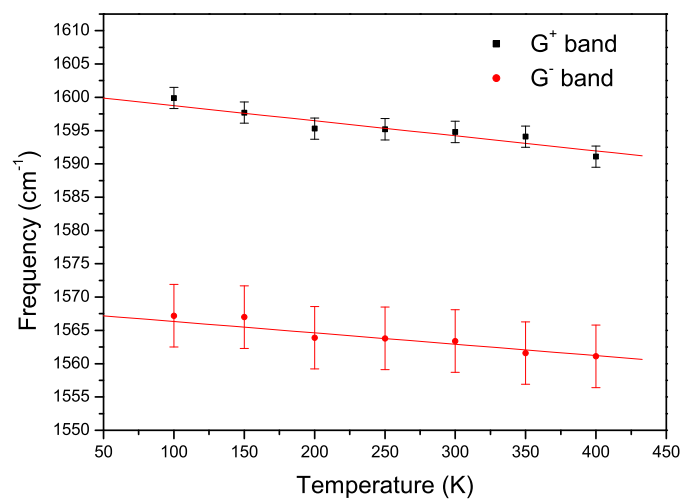


**Figure 6.22b:** Temperature dependence of the G<sup>+</sup> and G<sup>-</sup> band frequencies for SWCNTs excited with the 514.5 nm laser line for the low temperature region, with slopes being  $-2.11 \text{ cm}^{-1}/100\text{K}$  for the G<sup>-</sup> band and  $-2.44 \text{ cm}^{-1}/100\text{K}$  for the G<sup>+</sup> band.

temperature, with the slopes being  $-2.11 \text{ cm}^{-1}/100\text{K}$  for the  $G^-$  band and  $-2.44 \text{ cm}^{-1}/100\text{K}$  for the  $G^+$  band. Figure 6.22a shows the Raman spectra of the G-band taken in the temperature range 77K-400K. The spectra have been displaced upwards for the reasons of clarity. Figure 6.22b shows linear fits to the plot of  $G^+$  and  $G^-$  peak frequencies as a function of temperature.

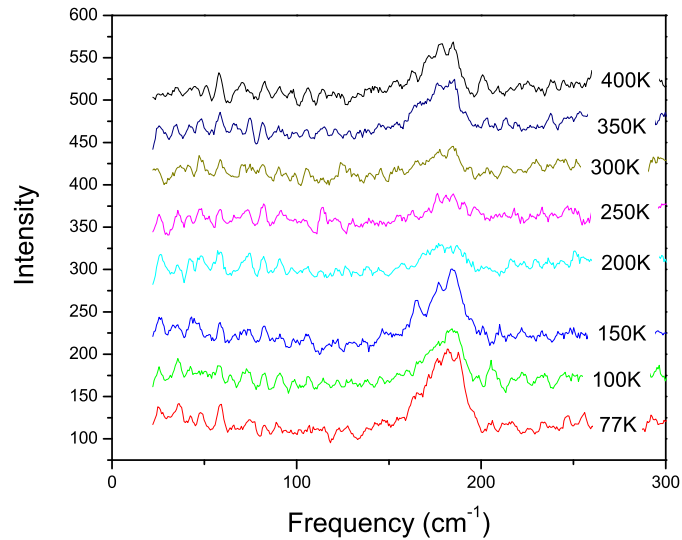


**Figure 6.23:** Temperature dependence of the RBM for the low temperature region for SWCNTs excited using the 514.5 nm excitation. The curves have been displaced for reasons of clarity.

The radial breathing mode does not show a significant change in frequency, but there is a notable change in the shape of the RBMs as temperature increases. Figure 6.23 shows the radial breathing modes taken in the temperature range 77K-400K. The curves have also been displaced for the purposes of clarity. Because of the weak intensities of the low temperature radial breathing modes, peak fitting could not be done for further analysis.

Figure 6.24 shows the combined curves for the low temperature and high temperature regions for the temperature dependence of the G-bands for SWCNTs excited using the 514.5 nm excitation line.

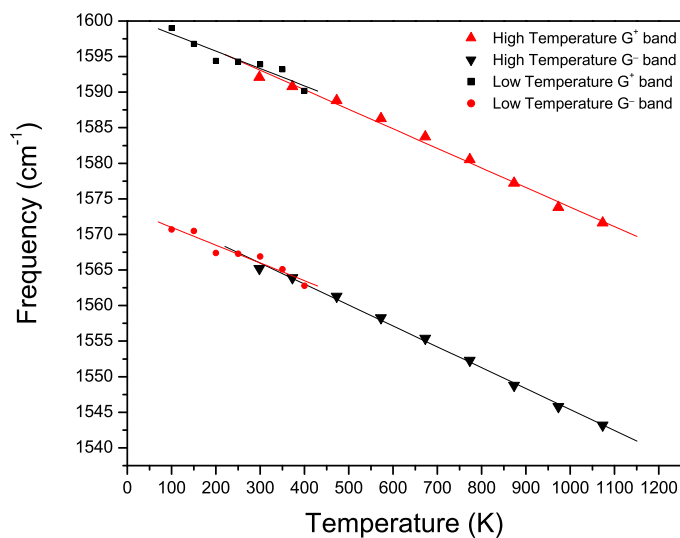


**Figure 6.24:** Temperature dependence of the  $G^+$  and  $G^-$  band frequencies for the low temperature and high temperature regions for SWCNTs excited with the 514.5 nm laser line.

### 6.5.2 Metallic SWCNTs: 647.1 nm

The temperature dependence of the G band of metallic SWCNTs excited by the 647.1 nm laser line is presented in this section. The bucky paper used was produced as described in section 6.2 and then taken through two annealing cycles to improve stability and purity. Raman spectra were collected in the cryostat and laser power density at the sample was approximately  $60\text{W}/\text{cm}^2$ .



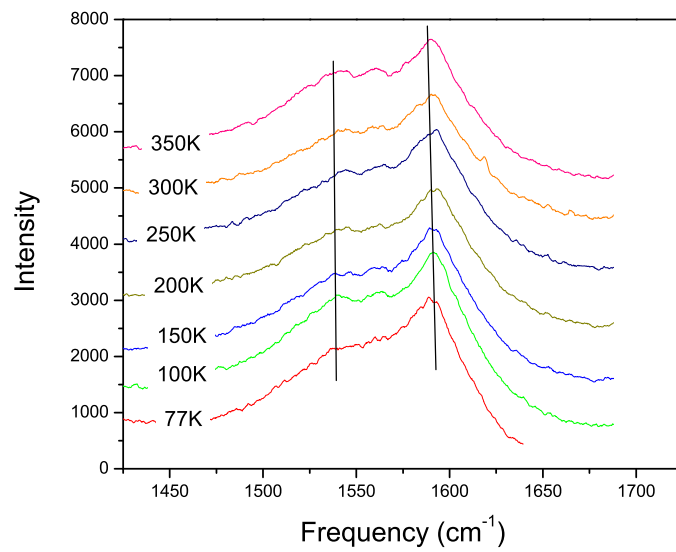


**Figure 6.25a:** Temperature dependence of the G band for the low temperature region for metallic SWCNTs excited using the 647.1 nm excitation. The curves have been displaced for the purposes of clarity.

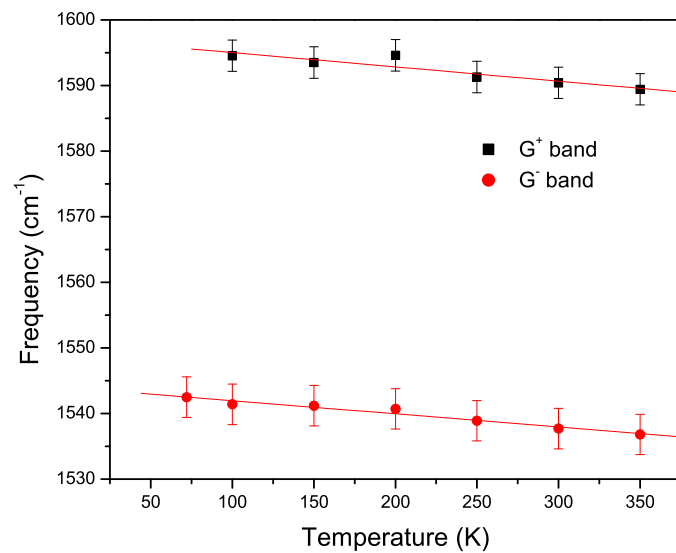


**Figure 6.25b:** Temperature dependence of the G<sup>+</sup> and G<sup>-</sup> band frequencies for metallic SWCNTs excited with the 647.1 nm laser line for the low temperature region, with slopes being  $-1.98 \text{ cm}^{-1}/100\text{K}$  for the G<sup>-</sup> band and  $-2.18 \text{ cm}^{-1}/100\text{K}$  for the G<sup>+</sup> band.

The  $G^+$  and  $G^-$  modes of metallic SWCNTs show a linear decrease of frequency with increasing temperature, with the slopes being  $-1.98 \text{ cm}^{-1}/100\text{K}$  for the  $G^-$  band and  $-2.18 \text{ cm}^{-1}/100\text{K}$  for the  $G^+$  band. Figure 6.25(a) shows the Raman spectra of the G-band taken in the temperature range 77K-350K. The spectra have been displaced for the reasons of clarity. Linear fits to the plot of  $G^+$  and  $G^-$  peak frequencies as a function of temperature are shown in Figure 6.25(b).

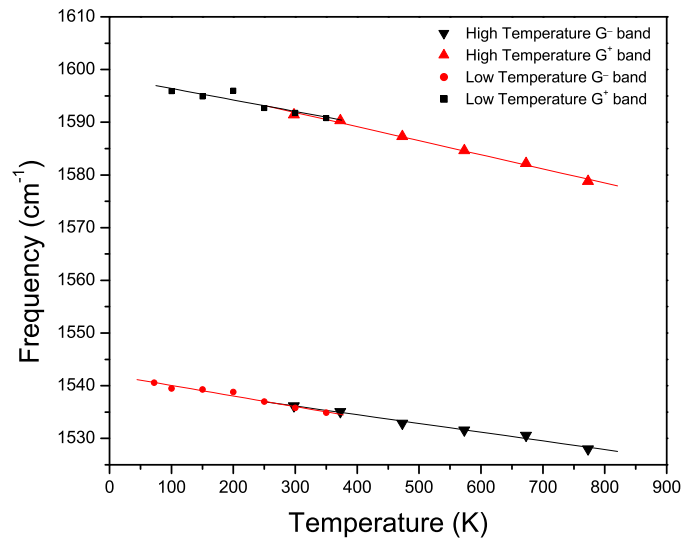


**Figure 6.26:** Temperature dependence of the  $G^+$  and  $G^-$  band frequencies for the low temperature and high temperature regions for metallic SWCNTs excited with the 647.1 nm laser line.

Figure 6.26 shows the combined curves for the low temperature and high temperature regions for the temperature dependence of the G-bands of metallic SWCNTs excited using the 647.1 nm excitation line. Table 6.6 shows the rate of frequency change of the  $G^+$  and  $G^-$  bands for metallic and semi-conducting tubes in the low temperature region.

**Table 6.6:** Slopes of the graphs of frequency versus temperature for the  $G^+$  and  $G^-$  bands of metallic and semi-conducting SWCNTs.

Laser	Electronic Property	$G^-$ slope( $\text{cm}^{-1}/100\text{K}$ )	$G^+$ slope ( $\text{cm}^{-1}/100\text{K}$ )
514.5 nm	Semi-conducting	-2.11	-2.44
647.1 nm	Metallic	-1.98	-2.18

## 6.6 G-band Splitting as a Function of Temperature

In this section the splitting of the G band ( $G^+$ - $G^-$ ) of metallic and semi-conducting SWCNTs as a function of sample temperature is discussed. The 647.1 nm laser line of the  $\text{Kr}^+$  laser was used to excite metallic tubes of diameter 1.45 nm while the 514.5 nm and 488.0 nm laser lines of the  $\text{Ar}^+$  laser were used to excite semi-conducting SWCNTs of diameters 1.33 nm and 1.52 nm respectively. Analysis of the G band splitting as a function of temperature allows determination of the pure temperature effects on the LO and TO mode splitting. Since anharmonic effects are the same for these modes, they do not affect their relative positions. This gives better insight into the phonon softening by a Kohn anomaly in SWCNTs.

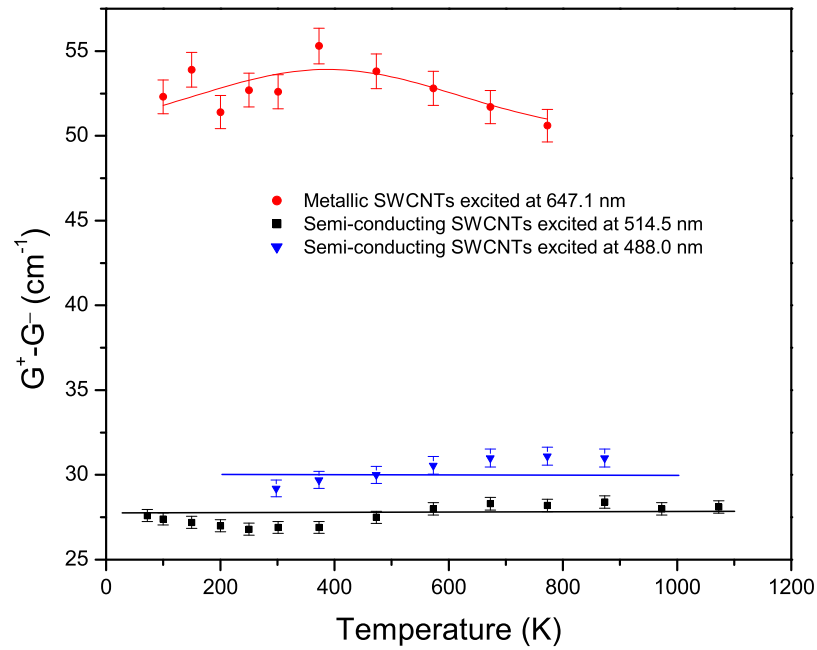


**Figure 6.27:** Temperature dependence of the  $G^+ - G^-$  splitting for metallic and semi-conducting SWCNTs. (Colour line) Circles: Metallic SWCNTs excited at 647.1 nm. Squares: Semi-conducting SWCNTs excited at 514.5 nm. Inverted triangles: Semi-conducting SWCNTs excited at 488.0 nm.

Figure 6.27 shows that the splitting in metallic SWCNTs is temperature dependent, especially in the high temperature region. This may be due to the fact that the LO mode in metallic SWCNTs is affected by a Kohn anomaly, which depends on sample temperature. As temperature changes, the softening of the LO mode by the Kohn anomaly also changes. The splitting of the LO and TO modes of semi-conducting SWCNTs is almost temperature independent, with tubes excited at 488.0 nm having a greater  $G^+ - G^-$  split ( $\approx 2.5 \text{ cm}^{-1}$ ) compared to those excited at 514.5 nm. Since the TO and LO modes in semi-conducting SWCNTs are not affected by a Kohn anomaly, the splitting of the LO and TO modes in semi-conducting tubes will be temperature independent and would be due to the relative effects of anharmonicity. However, at present we cannot give a full detailed explanation on the differences in the  $G^+ - G^-$  split between SWCNTs excited at 488.0 nm and those

excited at 514.5 nm. These experimental results are in good agreement with the theoretical calculations of Piskanec *et al.* 2007a.

## 6.7 Raman Scattering Measurements as a Function of Laser Power.

In this section the effects of laser power density on the behaviour of the tangential mode of semi-conducting tubes was studied using the 514.5 nm laser line of the argon ion laser. The sample temperature at each laser power density was calculated using the anti-Stokes/Stokes (AS/S) intensity ratio (Kuzmany 1998) and using the rate of frequency shifts of vibrational modes with temperature determined in Section 6.3.1. A comparison is made between sample temperatures determined from these two methods. The laser power at the source was kept between 0.48 mW and 7.20 mW for a laser spot size of 35  $\mu\text{m}$  giving a power density of 28  $\text{W}/\text{cm}^2$  to 415  $\text{W}/\text{cm}^2$  on the sample. Accumulation time for each Raman spectrum was maintained at 240 seconds.

Sample preparation was done using the method described in section 6.2. Before Raman spectra were collected the bucky paper was taken through two annealing cycles up to 873K in a Linkam heating cell. Raman spectra for the Stokes and anti-Stokes G-band were taken at different laser powers between 0.48 mW and 7.20 mW in an argon environment in the heating cell at room temperature. Laser powers were measured at the sample before and after the experiment.

Figures 6.28(a) and (b) show the laser power dependence of the Stokes and anti-Stokes  $G^+$  and  $G^-$  bands for semi-conducting SWCNTs excited with the 514.5 nm laser line. There is a shift to lower frequencies of the Stokes and anti-Stokes  $G^-$  and  $G^+$  band frequencies with increasing laser power density. Increasing the laser power density from 28  $\text{W}/\text{cm}^2$  to 415  $\text{W}/\text{cm}^2$  results in a Stokes frequency shift of 13.6  $\text{cm}^{-1}$  for the  $G^+$  band and 12.1  $\text{cm}^{-1}$  for the  $G^-$  band. Using the values of the rate of change of vibrational frequency of the G-bands with temperature

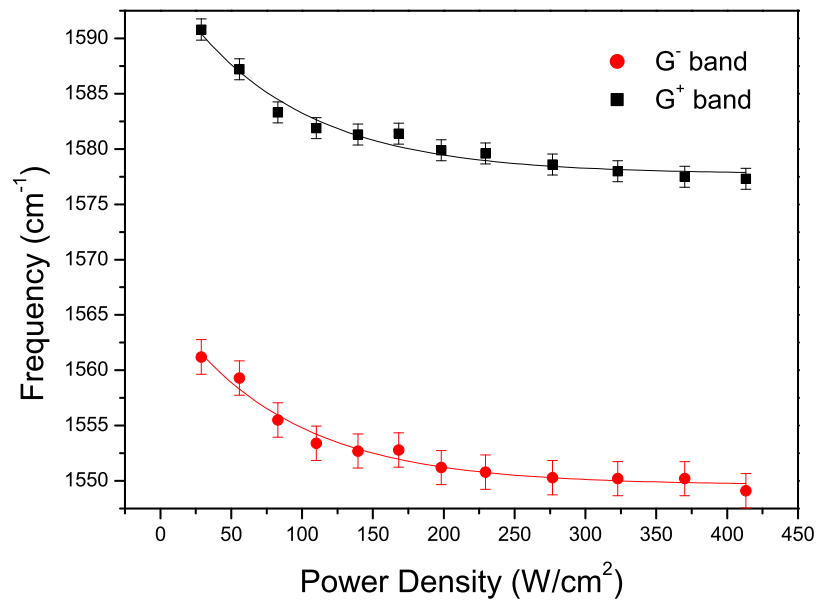


**Figure 6.28a:** Laser power density dependence of the Stokes  $G^-$  and  $G^+$  modes for semi-conducting SWCNTs excited with the 514.5 nm line of the  $\text{Ar}^+$  laser.

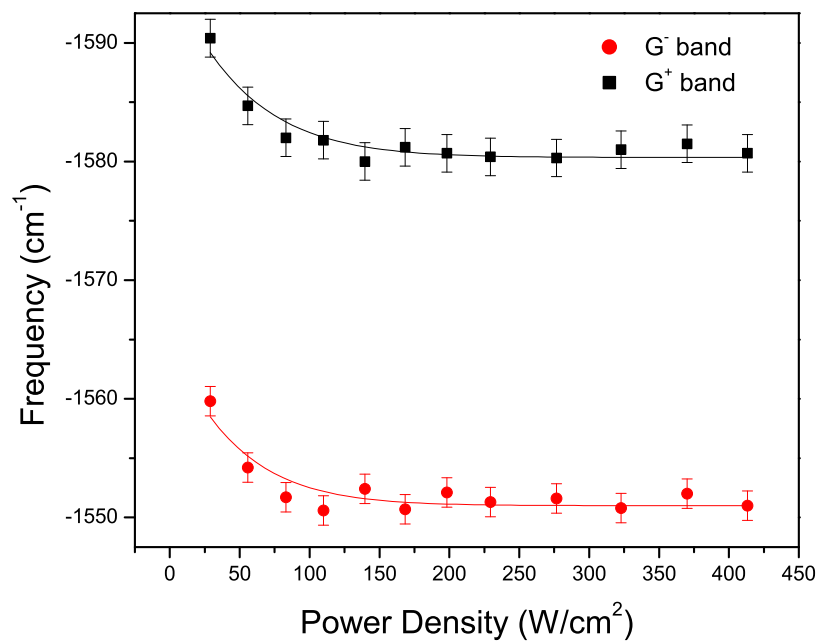


**Figure 6.28b:** Laser power density dependence of the anti-Stokes  $G^-$  and  $G^+$  modes for SWCNTs excited with the 514.5 nm excitation line of the  $\text{Ar}^+$  laser.

( $\frac{\partial\omega}{\partial T}$ ) obtained in Section 6.3.1 for the temperature dependence of the  $G^+$  and  $G^-$  modes using a heating cell, a  $G^+$  frequency shift of  $13.5 \text{ cm}^{-1}$  is equivalent to a sample temperature change of  $494.5\text{K}$ , and a  $G^-$  frequency change of  $12.1 \text{ cm}^{-1}$  is equivalent to a sample temperature change of  $412\text{K}$ . This shows that significant heating of the sample takes place at high laser power densities. This result shows that in temperature dependence experiments in SWCNTs, laser power densities should be carefully controlled and monitored to obtain accurate and reliable results.

Much of the previous work on the temperature dependence of SWCNTs has been done using extremely high laser powers (Li *et al.* 2000, Teredesai *et al.* 2001, Raravikar *et al.* 2002). For our experiments on the temperature dependence of Raman vibrational modes of SWCNTs, the laser power densities have been kept very low to minimise laser heating effects, thus giving more consistent results.

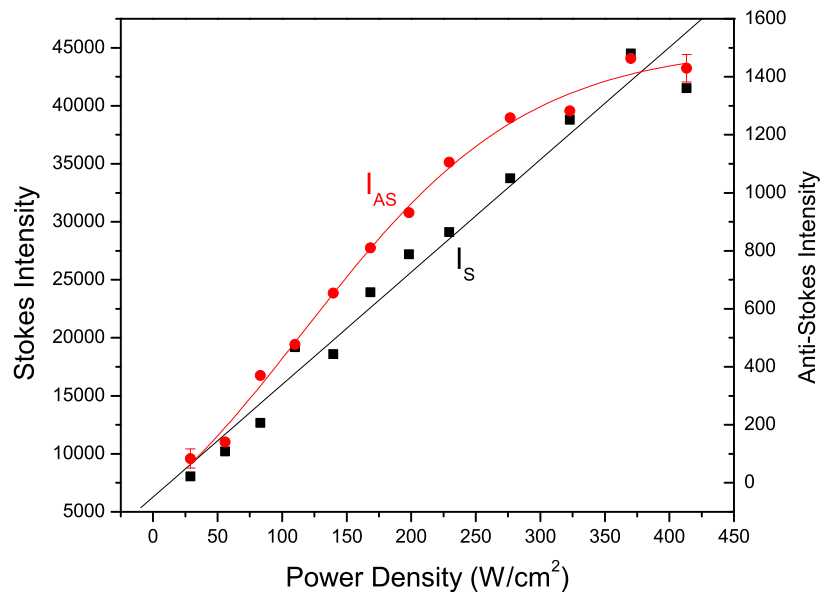


**Figure 6.29:** Laser power density dependence of the intensity of the Stokes and anti-Stokes  $G^+$  modes for SWCNTs excited with the  $514.5 \text{ nm}$  excitation line of the  $\text{Ar}^+$  laser.

Figure 6.29 shows the intensity of the Stokes and anti-Stokes  $G^+$  bands as a function of laser power density. As laser power density increases, the intensity of both the Stokes and anti-Stokes  $G^+$  bands increases. The Stokes intensity increases

linearly with increasing LPD, while the anti-Stokes intensity increases non linearly. This behaviour of the anti-Stokes intensity is different from the quadratic dependence on laser power density obtained when anti-Stokes pumping occurs, as shown in Figure 3.6. This shows that no anti-Stokes pumping takes place in this case. In the literature (Huong *et al.* 1995; Kuzmany 1998; Kneipp *et al.* 2000; Teredesai *et al.* 2001) the anti-Stokes/Stokes intensity ratio has been used for sample temperature determination since the strength of the anti-Stokes peak depends on the population of the first excited vibrational state, which is determined by the Boltzmann distribution. The AS/S intensity ratio can be expressed as

$$\frac{I_{AS}}{I_S} = \left( \frac{\nu_0 + \Delta\nu}{\nu_0 - \Delta\nu} \right)^4 \exp\left( \frac{-h c \Delta\nu}{kT} \right) \quad (6.6)$$

where  $h$  is Planck's constant,  $c$  the speed of light,  $\Delta\nu$  is the Raman shift in wavenumbers,  $k$  is the Boltzmann constant,  $\nu_0$  is the exciting frequency and  $T$  the sample temperature.

Table 6.7 shows temperatures calculated from the AS/S intensity ratio and that calculated from rate of  $G^+$  peak frequency shifts with temperature obtained in Section 6.3.1.

There are significant differences between the temperatures calculated from the AS/S intensity ratios and those calculated from peak frequency shifts. The AS/S temperature changes by just 160.2 K over the whole power density range while the temperature calculated from peak frequency shifts changes by 494.5 K. This result is consistent with the theory that the anti-Stokes/Stokes intensity ratio is not reliable for calculating temperatures for systems where the laser excitation is in resonance with the electronic transitions (Schomacker *et al.* 1984). In this case the 514.5 nm laser line, corresponding to an exciting energy of 2.41 eV, resonantly enhances the electronic transitions of semi-conducting SWCNTs.



**Table 6.7:** Calculated sample temperatures using the AS/S intensity ratio method and the peak frequency shift method.

Power Density (W/cm <sup>2</sup> )	AS/S Ratio Temp (K)	Freq Shift Temp (K)
28.9	421.1	-*
55.7	478.5	552.0
83.0	516.1	653.8
110.0	541.8	719.3
139.5	560.5	766.6
168.3	572.6	810.2
198.3	578.2	832.0
229.4	581.3	853.8
276.7	579.2	864.7
322.8	572.1	890.2
370.0	562.1	904.7
413.3	553.1	915.6

\*The frequency shift temperature cannot be calculated for the starting laser power density.

## 6.8 Discussion

### 6.8.1 G-band

Both metallic and semi-conducting tubes show a linear decrease at different rates of the  $G^+$  and  $G^-$  band peak frequencies with increasing temperature. This decrease can be attributed to the softening of the C-C atomic vibrations due to the softening of the force constants as a result of the thermal expansion of the C-C bonds with increasing temperatures (Huong *et al.* 1995; Huang *et al.* 1998; Raravikar *et al.* 2002). The decrease of both the  $G^+$  and  $G^-$  modes with temperature is irregular on the first annealing cycles, showing improved stability with subsequent annealing cycles. This effect can be associated with burning off of unstable and smaller diameter tubes due to annealing.

Brown *et al.* (2001) and Jorio *et al.* (2002b) showed that the  $G^-$  band frequency in semi-conducting SWCNTs is diameter dependent. This means that the  $G^-$  band frequency depends on the curvature of the nanotube. The slope of the  $G^-$  band frequency with temperature of semi-conducting SWCNTs excited by the 514.5 nm laser line is greater in magnitude than that of tubes excited by the 488.0 nm laser line (Table 6.5). A plausible explanation for this difference can be given in terms of  $sp^2/sp^3$  hybridization of the SWCNTs bonds. The folding of graphene into a SWCNT results in a mixing of the  $\sigma$  and  $\pi$  orbitals giving rise to  $sp^2/sp^3$  hybrid character of the SWCNT chemical bonds (Saito *et al.* 1998). Because the  $sp^2$  bonds of graphene are stiffer than the  $sp^3$  bonds, the mixing of the orbitals results in softer  $sp^2/sp^3$  hybrid bonds in SWCNTs. The bond mixing is proportional to curvature, resulting in tubes with higher curvatures (smaller diameters) having softer bonds. This means that nanotubes excited by the 514.5 nm laser line have softer bonds compared to those excited by the 488.0 nm line since they have a smaller diameter. The slopes of the  $G^-$  and  $G^+$  band frequencies with temperature of semi-conducting tubes excited with the 514.5 nm and 488.0 nm laser lines are in agreement with this explanation, since the smaller tubes excited with the 514.5 nm line show faster  $G^-$  and  $G^+$  band frequency downshift with increasing temperatures.

However, at this moment it cannot be explained why the rate of change of the  $G^+$  band frequency with temperature of tubes excited by the 488.0 nm laser line differs significantly from that of tubes excited with the 514.5 nm laser line. A detailed theoretical investigation of these modes at high temperatures appears necessary to explain this difference.

The slopes of the respective  $G^-$  band frequencies with temperature graphs of nanotubes excited by the 488.0 nm and 514.5 nm laser lines are larger than those respective slopes of the  $G^+$  band frequency with temperature graphs. Because of curvature effects, the mode arising from atomic vibrations tangential to circumference of the nanotube is expected to be more sensitive to temperature effects compared to vibrations parallel to the nanotube axis. The slopes of these graphs agree well with the mode assignment in semi-conducting tubes where the  $G^-$  band is associated with vibrations tangential (TO) to the surface of the nanotube and the  $G^+$  band is associated with vibrations parallel (LO) to nanotube axis.

However, the rate of decrease of the  $G^-$  band frequency with temperature in metallic nanotubes is smaller than the rate of decrease of the  $G^+$  band frequency with temperature. The TO mode is expected to be more sensitive to temperature effects compared to the LO mode. This result is consistent with the assignment of the tangential vibrations (TO) to the  $G^+$  mode and the longitudinal vibration (LO) to the  $G^-$  mode in metallic nanotubes (Lazzeri *et al.* (2006); Popov and Lambin, 2006; Ishikama and Ando, 2006; Piscanec *et al.* 2007a). This supports the conclusion that the BWF line shape in metallic tubes originates from electron-phonon coupling.

The rate of decrease of the  $G^-$  band frequency with temperature of metallic nanotubes is considerably smaller compared to the rate of decrease of the  $G^-$  band frequency with temperature of semi-conducting nanotubes. This can be explained in terms of the Kohn anomaly behaviour at high temperatures. The Kohn anomaly, whose effect is to lower the LO mode frequency in metallic SWCNTs, is suppressed with increasing temperature (Popov and Lambin, 2006; Piscanec *et al.* 2007a). This implies that as temperature increases, the LO mode softening by the Kohn anomaly

reduces, and the LO mode frequency has a tendency to upshift. This effect is opposite to the downshift in the mode frequency due to softening of the C-C atomic vibrations and the softening of force constants with increasing temperature (Huong 1995; Huang 1998; Raravikar *et al.* 2002). The result is a lower rate of decrease of the  $G^-$  band frequency with temperature of metallic SWCNTs compared to the rate of decrease of the  $G^-$  band frequency with temperature of semi-conducting tubes which are not affected by a Kohn anomaly. This result is also consistent with the theory that the  $G^-$  band in metallic nanotubes corresponds to the LO mode and is a result of electron-phonon coupling.

The rate of decrease of the  $G^+$  band frequency with temperature of metallic nanotubes ( $-2.68 \text{ cm}^{-1}/100\text{K}$ ) is comparable to the rate of decrease of the  $G^-$  band frequency with temperature of semi-conducting SWCNTs excited by the 488.0 nm and 514.5 nm laser lines ( $-2.45 \text{ cm}^{-1}/100\text{K}$  and  $-2.94 \text{ cm}^{-1}/100\text{K}$  respectively). If the  $G^-$  band in semi-conducting SWCNTs is due to the TO mode, then this result implies that the  $G^-$  band in metallic SWCNTs is also due to the TO mode, consistent with the mode assignment of Lazzeri *et al.* (2006), Popov and Lambin, 2006, Ishikama and Ando, 2006 and Piscanec *et al.* 2007a.

The linewidth of the BWF line decreases with increasing temperatures. This is in contrast to the behaviour of the Lorentzian lineshapes of the  $G^-$  band in semi-conducting tubes and the  $G^+$  band in the spectra of metallic nanotubes, which increase with temperature. The EPC theory can be used to explain the behaviour of the  $G^-$  band linewidth of metallic SWCNTs with increasing temperatures since the suppression of the Kohn anomaly and EPC with increasing temperatures leads to narrowing of the  $G^-$  band of metallic SWCNTs (Equations 6.3 and 6.4). These equations demonstrate that the BWF linewidth depends on the degree of EPC which in turn decreases with increasing temperature (Piscanec *et al.* 2007a). It is noted that Jiang *et al.* 2002 and Uchida *et al.* 2004 used the plasmon-phonon coupling theory to explain the above behaviour in terms of weakening of the plasmon band with increasing temperatures. However this theory is restricted only to bundled

SWCNTs and is non quantitative.

It is concluded that the electron-phonon coupling model provides a self consistent account of the results and is the preferred explanation rather than that provided by the plasmon-phonon coupling theory.

Furthermore the differences in the slopes between semi-conducting and metallic SWCNTs are a result of the differences in their electronic properties together with structural and vibrational influences. A fully quantitative understanding will require further theoretical work.

A laser power dependence study of the G band of semi-conducting SWCNTs using the 514.5 nm laser line shows that there is significant heating of the sample at LPDs of the order of  $10^2$  W/cm<sup>2</sup>. The intensity of the Stokes signal was found to increase linearly with LPD and the anti-Stokes intensity increases non linearly. Sample temperatures were calculated using the ratio of the anti-Stokes/Stokes intensities method and the peak frequency shift method. A comparison of the temperatures calculated using these two methods show that the anti-Stokes/Stokes intensity ratio appears not to be a reliable method for determining temperatures in resonance processes.

### 6.8.2 Radial Breathing Modes

There is a general linear decrease of the mode frequencies of the entire RBM feature as temperature is increased for all types of nanotubes. In metallic nanotubes however, the rate of decrease is larger as compared to semi-conducting tubes. A summary of the slopes is given in Table 6.5. The decrease of the RBM frequency has been attributed to the thermal expansion of C-C bonds (Raravikar *et al.* 2002). A thermal expansion of the C-C bonds results in an increase in the diameter of the nanotube, and since  $\omega_{RBM}$  is proportional to  $\frac{1}{dt}$ ,  $\omega_{RBM}$  decreases as radius increases. It is considered that structural influences associated with the tubes of different chiralities will influence the rate of decrease.

There are also significant changes in the lineshapes of the RBM with increasing temperatures. The change in lineshape of the RBM with temperature can be associated with the change in the size of the resonance window with increasing temperatures. Reich *et al.* (2002) have shown that the curvature of a nanotube reduces the band gap by causing a downshift of the conduction bands. Therefore, as temperature increases, the C-C bond thermally expands resulting in reduced curvature and hence the size of the band gap increases. They also showed that bundling in SWCNTs decreases the separation of the conduction and valence bands around the Fermi level. As temperature increases, thermal expansion results in an increase of the intertube distance in the bundle, and hence weakening of the bundle, resulting in an increased separation of the valence and conduction bands near the Fermi level.

A change in the size of the resonance window results in a change in the tubes that are in resonance with the excitation line. With increasing temperature, some tubes can enter the resonance window, while others may go out of resonance, resulting in a change in the lineshape of the RBM.

Fantini *et al.* (2004), Capaz *et al.* (2005) and Cronin *et al.* (2006) have also shown that electronic transitions for resonance ( $E_{ii}$ ) in SWCNTs are temperature dependent. The temperature dependence can be divided into harmonic and anharmonic effects, where the harmonic effects arise due to electron-phonon interaction (Cronin *et al.* (2006)), and the anharmonic effects are due to thermal expansion.

Figure 6.30 shows the changes that happen to the RBM line shape as temperatures are increased. At 373K only two Lorentzian peaks can be fitted to the RBM feature while at 773K an additional peak can be fitted. This suggests that at high temperatures a different set of SWCNTs will be in resonance compared to at lower temperatures.

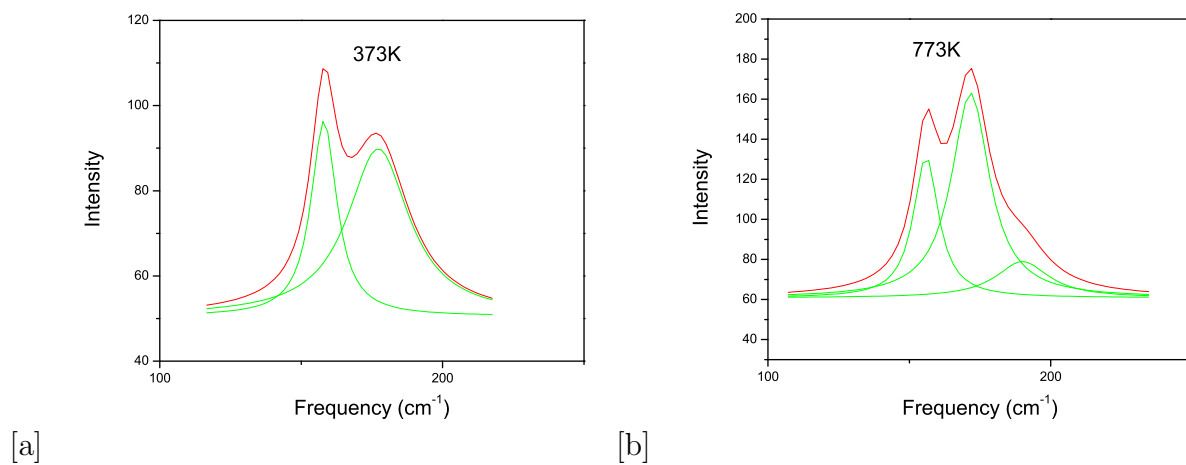


**Figure 6.30:** Radial breathing modes at 373K and at 773K showing the different line-shapes at different temperatures for the 514.5 nm excitation.

# Chapter 7

## Conclusions

Single-walled carbon nanotubes were successfully synthesized using the electric arc discharge method using  $\text{LaNi}_5$  as a catalyst. An optimization process was carried out using different catalytic concentrations and different buffer gases under different pressures. The as-produced SWCNTs material was characterized by transmission electron microscopy and Raman scattering. An analysis of the ratio of the intensity of the  $G^+$  band to that of the D band showed that using 26 at.%  $\text{LaNi}_5$  catalyst and helium gas at a pressure of 60 kPa gives nanotubes of high purity with the narrowest diameter distribution of all the various combinations of catalysts and helium gas pressure.

Raman measurements on the as-produced SWCNTs could not be undertaken for temperatures exceeding 773K due to the presence of metallic impurities. Purification of the as-produced SWCNTs was successfully carried out to remove these metallic impurities. After purification Raman spectra could be measured for temperatures up to 1073K for semi-conducting tubes and 873K for metallic SWCNTs. We also showed that taking the sample through several annealing cycles prior to the final measurements stabilizes the sample. The curves of the peak frequency against temperature show linear behaviour with subsequent annealing cycles, an effect that is due to the destruction of the smaller diameter and unstable SWCNTs.

The temperature dependence results of the Raman vibrational modes show that



the  $G^-$  and  $G^+$  band frequencies decrease with increasing sample temperatures for both metallic and semi-conducting tubes. A comparison of the rate of change of the  $G^-$  band frequency with temperature and that of the  $G^+$  band frequency with temperature gives a deeper understanding of the assignment of vibrational modes in metallic nanotubes. The rate of change for the  $G^-$  band frequency of metallic nanotubes compared to that for the  $G^+$  band frequency is consistent with the assignment by Lazzeri *et al.* (2006) of the  $G^-$  peak in metallic tubes to the TO mode. The rate of change of the  $G^-$  band frequency in metallic SWCNTs significantly differs from that of the  $G^+$  band frequency and that of the  $G^-$  and  $G^+$  band frequencies in semi-conducting tubes. This can be explained in terms of the suppression of the Kohn anomaly effect at high temperatures. This result is consistent with the theory that the  $G^-$  peak in metallic SWCNTs is a result of electron-phonon coupling and not plasmon-phonon coupling.

The linewidth of the  $G^-$  and  $G^+$  bands were studied as a function of temperature for metallic and semi-conducting SWCNTs. The linewidth of the  $G^-$  band in metallic SWCNTs decreases with increasing temperatures, contrary to what is expected of the line width of a Raman peak. This behaviour was explained using both the plasmon-phonon coupling model and the electron-phonon coupling model. The plasmon-phonon coupling explanation is valid for SWCNTs in a bundle and not isolated SWCNTs. However, the EPC theory gives an explanation that holds for both isolated and bundled SWCNTs.

The temperature dependence of the radial breathing mode on temperature was studied. There is a decrease of the RBM frequency with increasing temperature. This decrease is a result of thermal expansion in the radial direction and softening of the C-C bonds. The line shapes of the RBM are observed to change with changes in sample temperatures. This change is associated with the dependence of the size of the resonance window on temperature. As temperature changes, the size of the resonance window changes resulting in a change in the of the SWCNTs that are in resonance, leading to a change in the line shape of the RBM feature.

The laser power dependence of the peak position and intensity of the G band was studied for semi-conducting SWCNTs using the 514.5 nm laser line. The intensity of both the Stokes and anti-Stokes bands increase with increasing laser powers. The Stokes intensity increases linearly with power density. The anti-Stokes intensity does not increase in a quadratic manner as would be expected in the case of anti-Stokes pumping. Sample temperatures were calculated using the anti-Stokes/Stokes ratios method and the frequency shift method. A comparison of temperatures calculated using these two methods shows that the AS/S intensity ratio method appears not to be as reliable for calculating temperatures for resonance processes. The magnitude of the peak frequency for both Stokes and anti-Stokes  $G^-$  and  $G^+$  bands decreased with increasing laser powers. This proves that there is significant heating of the sample by the laser, emphasizing the importance of monitoring the laser power densities in these types of experiments.

## Recommendations

The experimental results from the temperature dependence of the linewidths of the G bands and the values of the slopes of the peak frequencies of the  $G^-$  and  $G^+$  bands with temperature give contradicting conclusions on the origins of the BWF line shape in the spectra of metallic SWCNTs. To get a deeper understanding into the origins of this feature, it would be important to do the experiments on the temperature dependence of the line width using isolated SWCNTs of known chiralities. This would give a deeper insight into the role played by the plasmon band if any in the formation of the BWF feature.

# Bibliography

Adar F. *Handbook of Raman Spectroscopy*. Marcel Dekker, New York (2001) Eds . Lewis IR, Edwards HGM.

Beesley MJ. *Lasers and their Applications*. Taylor and Francis Ltd. (London) (1976)

Bose S, Gayen S, Behera S. *Phys. Rev. B* **72**, 153402 (2005)

Brown S, Jorio A, Corio P, Dresselhaus MS, Dresselhaus G, Saito R, Kneipp K. *Phys. Rev. B* **63**, 155414 (2001)

Burns G. *Solid State Physics*. Academic Press (London) (1985)

Capaz RB, Spataru CD, Tangney P, Cohen ML, Louie SG. *Phys. Rev. Lett.* **94**, 036801 (2005)

Charlier JC, Iijima S. *Topics in Applied Physics* **80**, *Carbon Nanotubes: Synthesis, Structure, Properties and Applications*. Springer-Verlag (Berlin, Heidelberg) (2001)

Chattopadhyay D, Galeska I, Papadimitrakopoulos F. *Carbon* **40**, 985, (2002)

Cheng H, Li F, Su G, Pan H, He L, Sun X, Dresselhaus MS. *Appl. Phys. Lett.* **72**, 3282 (1998)

---

Corio P, Santos P, Brar V, Samsonidze G, Chou S, Dresselhaus M. *Chem. Phys. Lett.* **370**, 675 (2003)

Cronin SB, Yin Y, Walsh A, Capaz RB, Stolyarov A, Tangney P, Cohen ML, Louie SG, Swan AK, Unlu MS, Goldberg BB, Tinkham M. *Phys. Rev. Lett.* **96**, 127403 (2006)

Dai H. *Topics in Applied Physics* **80**, 29 *Carbon Nanotubes: Synthesis, Structure, Properties and Applications*. Springer-Verlag (Berlin, Heidelberg) (2001)

Dresselhaus M, Dresselhaus G, Jorio A, Souza Filho AG, Saito R. *Carbon* **40**, 2043 (2002)

Dresselhaus MS, Dresselhaus G, Saito R, Jorio A. *Phys. Rep.* **409**, 47 (2005)

Dresselhaus MS, Jorio A, Pimenta MA. *An. Acad. Bras. Cienc.* **78**, 3 (2006)

Fantini C, Jorio A, Souza M, Strano MS, Dresselhaus MS, Pimenta MA. *Phys. Rev. Lett.* **93**[14], 147406 (2004)

Guo T, Nikolaev P, Thess A, Colbert D, Smalley RE. *Chem. Phys. Lett.* **243**, 49 (1995)

Hayes W. *Comtemp. Phys.* **16**, 69 (1975)

Hayes JM. PhD Thesis, University of Bristol. (2002)

Hecht J. *The Laser Guidebook*. Second Edition McGraw Hill Professional (1999)

Huang F, Yue KT, Tan P, Zhang S, Shi Z, Zhou X, Gu Z. *J. Appl. Phys.* **84**,

4022 (1998)

Hughes AE. *J. Phys. Chem. Solids* **29**, 1461 (1968)

Huong P, Cavagnat R, Ajayan P, Stephan O. *Phys. Rev B* **51**, 10048 (1995)

Iijima S. *Nature* (London) **354**, 56 (1991)

Ishikawa K, Ando T. *J. Phys. Soc. Jpn* **75**, 084713 (2006)

Jiang C, Kempa K, Zhao J, Schelecht U, Kolb U, Basche T, Burghard M, Mews A. *Phys. Rev. B* **66**, 161404 (2002)

Jorio A, Saito R, Hafner J, Lieber C, Hunter M, McClure T, Dresselhaus G, Dresselhaus MS. *Phys. Rev. Lett.* **86**, 1118 (2001)

Jorio A, Fantini C, Dantao M, Pimenta MA, Souza Filho AG, Samsonidze Ge G, Brar VW, Dresselhaus G, Dresselhaus MS, Swan AK, Unlu M, Colberg BB, Saito R. *Phys. Rev B* **66**, 115411 (2002a)

Jorio A, Souza Filho AG, Dresselhaus G, Dresselhaus MS, Swan AK, Unlu M, Goldberg BB, Pimenta MA, Hafner JH, Lieber CM, Saito R. *Phys. Rev. B* **65**, 155412 (2002b)

Jorio A, Pimenta MA, Souza Filho AG, Saito R, Dresselhaus G, Dresselhaus MS. *New. J. Phys.* **5**, 139.1 (2003)

Jorio A, Saito R, Dresselhaus G, Dresselhaus MS. *Phil. Trans. R. Soc. Lond. A.* **362**, 2311 (2004)

- 
- Journet C, Bernier P. *Appl. Phys. A* **67**,1-9 (1998)
- Kagel RO. *Practical Handbook of Spectroscopy*. CRC Press Inc. (1991) Ed. Robinson JW.
- Kataura H, Kumazawa Y, Maniwa Y, Ohtsuka Y, Sen R, Suzuki S. *Carbon* **38**, 1691 (2000)
- Kavhita G, Vivek S, Govindaraj A, Narayana C. *Proc. Indian Acad. Sci. (Chem. Sci.)* **115**, 689 (2003)
- Kempa K. *Phys. Rev. B* **66**, 195406 (2002)
- Keresztury G. *Handbook of Vibrational Spectroscopy. Vol. 1*. John Wiley (2002) Eds. Chalmers J, Griffiths P
- Kneipp K, Wang Y, Kneipp H, Itzkan I, Ramachandra D, Feld M. *Phys. Rev. Lett.* **76**, 2444 (1996)
- Kittel C. *Introduction to Solid State Physics, 7th Edition*. John Wiley and Sons, Inc. (1996)
- Kneipp K, Kneipp H, Corio P, Brown S, Shafer K, Mots J, Perelman L, Hanlon E, Marucci A, Dresselhaus G, Dresselhaus M. *Phys. Rev. Lett.* **84**, 3470 (2000)
- Kohn W. *Phys. Rev. Lett.* **2**, 9 (1959)
- Kuzmany H. *Solid-State Spectroscopy*. Springer-Verlag (Berlin, Heidelberg) (1998)
- Lazzeri M, Piscanec S, Mauri F, Ferrari A, Robertson J. *Phys. Rev. B* **73**, 155426

(2006)

Li H, Yue K, Lian Z, Zhan Y, Zhou L, Zhang S, Shi Z, Gu Z, Liu B, Yang R, Yang H, Zou G, Zhang Y, Iijima S. *Appl. Phys. Lett.* **76**, 2053 (2000)

Louie S. *Topics in Applied Physics* **80**, 113, *Carbon Nanotubes: Synthesis, Structure, Properties and Applications*. Springer-Verlag (Berlin, Heidelberg) (2001) *Eds.* Dresselhaus M, Dresselhaus G, Avouris Ph.

Matthew MJ, Pimenta MA, Dresselhaus G, Dresselhaus MS, Endo M. *Phys. Rev. B* **59**, R6585 (1999)

Maultzsch J, Reich S, Thomsen C. *Phys. Rev. B* **64**, 121407(R) (2001)

Nikolaev P, Bronikowski M, Bradlet R, Rohmund F, Colbert D, Smith K, Smalley R. *Chem. Phys. Lett.* **313**, 91 (1999)

Oron-Carl M, Henrich M, Kappes M, v. Lohneysen H, Krupke R. *Nano. Lett.* **5**, 1761 (2005)

Pimenta MA, Marucci A, Empedocles SA, Bawendi MG, Hanlon E, Rao A, Eklund P, Smalley R, Dresselhaus MS. *Phys. Rev. B* **58**, R16016 (1998)

Pimenta MA, Jorio A, Brown S, Souza Filho AG, Dresselhaus G, hafner JH, Lieber CM, Saito R, Dresselhaus MS. *Phys. Rev. B* **64**, 041401 (2001)

Piscanec S, Lazzeri M, Mauri F, Ferrari AC, Robertson J. *Phys. Rev. Lett.* **93**, 185503 (2004)

Piscanec S, Lazzeri M, Robertson J, Ferrari AC, Mauri F. *Phys. Rev. B* **75**, 035427

(2007a)

Piscanec S, Lazzeri M, Mauri F, Ferrari AC. *Eur. Phys. J. Special Topics* **148**, 159 (2007b)

Popov VN. *New. J. Phys* **6**, 17 (2004)

Popov VN, Henrard L. *Phys. Rev B* **70**, 115407 (2004)

Popov VN, Lambin P. *Phys. Rev. B* **73**, 085407 (2006)

Rammutla KE. PhD Thesis, University of the Witwatersrand, Johannesburg. (2001)

Raravikar N, Koblinski P, Rao A, Dresselhaus MS, Schadler L, Ajayan P. *Phys. Rev B* **66**, 235424 (2002)

Reich S, Thomsen C, Ordejon P. *Phys. Rev. B* **65**, 155411 (2002)

Reich S, Thomsen C, Maultzsch J. *Carbon Nanotubes: Basic Concepts and Physical Properties*. WILEY-VCH Verlag GmbH and Co. (Weinheim) (2004)

Reynolds W. *Physical Properties of Graphite*. Elsevier (Amsterdam, London, New York) (1968)

Saito R, Dresselhaus G, Dresselhaus MS. *Physical Properties of Carbon Nanotubes*. Imperial College Press, (London) (1998).

Saito R, Kataura H. *Topics in Applied Physics* **80**, 213 *Carbon Nanotubes: Synthesis, Structure, Properties and Applications*. Springer-Verlag (Berlin, Heidelberg) (2001) *Eds.* Dresselhaus M, Dresselhaus G, Avouris Ph.



---

Saito R, Takeya T, Kimura T, Dresselhaus G, Dresselhaus MS, *Phys. Rev. B* **57**, 4145 (1999)

Schomacker KT, Bangcharoenpaurpong O, Champion PM. *J. Chem. Phys.* **80**, 4701 (1984)

Scott CD, Arepalli S, Nikolaev P, Smalley RE. *Appl. Phys. A* **72**, 573 (2001)

Smith WE, Rodger C. *Handbook of Vibrational Spectroscopy. Vol. 1.* John Wiley (2002) Eds. Chalmers J, Griffiths P

Souza Filho AG, Jorio A, Samsonidze Ge G, Dresselhaus G, Saito R, Dresselhaus MS. *Nanotechnology* **14**, 1130 (2003)

Tan PH, Deng YM, Zhao Q, Cheng WC. *Appl. Phys. Lett.* **74**, 13 (1999)

Tarasov BP, Muradyan VE, Shul'ga YM, Krinichnaya P, Kuyunko NS, Efimov ON, Obraztsova ED, Schur DV, Maehlen JP, Yartys VA, Lai H. *Carbon* **41**, 1357 (2003)

Telg H, Maultzsch J, Reich S, Hennrich F, Thomsen C. *Phys. Rev. Lett.* **93**, 177401 (2004)

Teredesai P, Sood A, Govindaraj A, Rao C. *Appl. Surf. Sci.* **182**, 196 (2001)

Thess A, Lee R, Nikolaev P, Dai H, Petit P, Robert J, Xu C, Lee Y, Kim SG, Rinzler AG, Colbert DT, Scuseria GE, Tomanek D, Fischer JE, Smalley RE. *Science* **273**, 483 (1996)

Thomsen C, Reich S, Maultzsch J. *Phil. Trans. R. Soc. Lond. A* **362**, 2337

(2004)

Uchida T, Tachibana M, Kutita S, Kojima K. *Chem. Phys. Lett.* **400**, 341 (2004)

Yin Y, Walsh A, Vamivakas A, Cronin S, Stolyarov A, Tinkham M, Basca W, Unlu M, Goldberg B, Swan A. *IEEE Journal of Selected Topics in Quantum Electronics* **12** [6], 1083 (2006)

Zhang L, Li H, Yue KT, Zhang S, Wu X, Zi J, Shi Z and Gu Z. *Phys. Rev. B* **65**, 073401 (2002)

Zhang Q, Yang DY, Wang SG, Yoon SF, Ahn J. *Smart. Mater. Struct* **15**, S1 (2006)

Zhang Y, Xie L, Zhang J, Wu Z, Liu Z. *J. Phys. Chem. C* **111**, 14031 (2007)

Zhao X, Inoue S, Suzuki T, Ando Y. *Chem. Phys. Lett.* **373**, 266 (2003)

Zheng LX, O'Connell MJ, Doorn SK, Liao XZ, Zhao YH, Akhadov EA, Hoffbauer MA, Roop BJ, Jia QX, Dye RC, Peterson DE, Huang SM, Liu J, Zhu YT. *Nature. Mat.* **3**, 673 (2004)